

Award Number:
W81XWH-11-2-0109

TITLE:
Toward Development of a Field-Deployable Imaging Device for TBI

PRINCIPAL INVESTIGATOR:
Pierre D. Mourad, PhD

CONTRACTING ORGANIZATION:
University of Washington,
Seattle WA 98107

REPORT DATE:
March 2014

TYPE OF REPORT:
annual report

PREPARED FOR: U.S. Army Medical Research and Materiel Command
Fort Detrick, Maryland 21702-5012

DISTRIBUTION STATEMENT:

☒ Approved for public release; distribution unlimited

The views, opinions and/or findings contained in this report are those of the author(s) and should not be construed as an official Department of the Army position, policy or decision unless so designated by other documentation.

REPORT DOCUMENTATION PAGE				Form Approved OMB No. 0704-0188	
Public reporting burden for this collection of information is estimated to average 1 hour per response, including the time for reviewing instructions, searching existing data sources, gathering and maintaining the data needed, and completing and reviewing this collection of information. Send comments regarding this burden estimate or any other aspect of this collection of information, including suggestions for reducing this burden to Department of Defense, Washington Headquarters Services, Directorate for Information Operations and Reports (0704-0188), 1215 Jefferson Davis Highway, Suite 1204, Arlington, VA 22202-4302. Respondents should be aware that notwithstanding any other provision of law, no person shall be subject to any penalty for failing to comply with a collection of information if it does not display a currently valid OMB control number. PLEASE DO NOT RETURN YOUR FORM TO THE ABOVE ADDRESS.					
1. REPORT DATE March 2014		2. REPORT TYPE annual		3. DATES COVERED 15 February 2013-14 February 2014	
4. TITLE AND SUBTITLE Toward Development of a Field---Deployable Imaging Device for TBI				5a. CONTRACT NUMBER	
				5b. GRANT NUMBER W81XWH-11-2-0109	
				5c. PROGRAM ELEMENT NUMBER	
6. AUTHOR(S) Pierre D. Mourad, Ph.D. E-Mail: pierre@apl.washington.edu				5d. PROJECT NUMBER	
				5e. TASK NUMBER	
				5f. WORK UNIT NUMBER	
7. PERFORMING ORGANIZATION NAME(S) AND ADDRESS(ES) AND ADDRESS(ES) University of Washington, Seattle WA 98195-6470				8. PERFORMING ORGANIZATION REPORT NUMBER	
9. SPONSORING / MONITORING AGENCY NAME(S) AND ADDRESS(ES) U.S. Army Medical Research and Materiel Command Fort Detrick, Maryland 21702-5012				10. SPONSOR/MONITOR'S ACRONYM(S)	
				11. SPONSOR/MONITOR'S REPORT NUMBER(S)	
12. DISTRIBUTION / AVAILABILITY STATEMENT Approved for Public Release; Distribution Unlimited					
13. SUPPLEMENTARY NOTES					
14. ABSTRACT <p>Improvised explosive devices (IEDs) produce head injuries in nearly a majority of surviving soldiers. Most brain-injured soldiers do not, however, receive the necessary, rapid brain imaging studies as would their civilian counterparts. Instead they are flown to rear-echelon medical service centers such as in Germany for those studies, as well as additional medical care. There exists, therefore, a critical need for robust brain imaging systems at and near the battlefield. This gap in patient care reduces the quality of care and potentially, therefore the quality of life of injured soldiers. This gap also defines a critical need for rugged, field deployable systems capable of imaging injured brain. For a variety of reasons it is reasonable to expect that changes in the stiffness of brain accompany TBI, and that ultrasound-based 'sonoelastic' imaging modalities responsive to some measure of stiffness might offer a useful means for imaging the changes to brain due to TBI. Use of such systems in and near the field should improve clinical outcome for patients suffering from TBI. Our long-term goal is to develop a field deployable brain imaging system, capable of transcranial application, responsive to brain stiffness.</p>					
15. SUBJECT TERMS traumatic brain injury, ultrasound, sonoelasticity, brain imaging.					
16. SECURITY CLASSIFICATION OF:			17. LIMITATION OF ABSTRACT	18. NUMBER OF PAGES	19a. NAME OF RESPONSIBLE PERSON
a. REPORT U	b. ABSTRACT U	c. THIS PAGE U			USAMRMC
			UU	110	19b. TELEPHONE NUMBER (include area code)

Table of Contents

	<u>Page</u>
Introduction.....	pg #4
Body.....	pg #5
Key Research Accomplishments.....	pg #16
Reportable Outcomes.....	pg #17
Conclusion.....	pg #18

INTRODUCTION – subject. Improvised explosive devices (IEDs) produce head injuries in nearly a majority of surviving soldiers. Most brain-injured soldiers do not, however, receive rapid brain imaging studies as would their civilian counterparts. Instead they are flown to rear-echelon medical service centers such as in Germany for those studies, as well as additional medical care. This is because magnetic resonance imaging is unavailable in or near the theatre of war (and a bad idea for many patients because of the presence of metal fragments) and because of the lack reliably operational CT machines at medical centers in Iraq. In the mean time, due to the lack of adequate neuro-imaging, acute neurosurgical care in response to closed TBI often requires a complete hemicraniectomy (removal of one side of the patient’s skull) simply to assay the extent and location of injured brain. There exists, therefore, a critical need for robust brain imaging systems at and near the battlefield. Also, more subtle brain injuries are apparent clinically but difficult to definitively diagnose, hence treat. These gaps in patient care reduce the quality of care and potentially, therefore the quality of life of injured soldiers. This gap also defines a critical need for rugged, field deployable systems capable of imaging injured brain.

INTRODUCTION - purpose. For a variety of reasons (summarized in a recent book chapter of mine – Mourad, 2013) it is reasonable to expect that changes in the stiffness of brain accompany TBI, and that ultrasound-based ‘sonoelastic’ imaging modalities responsive to some measure of stiffness might offer a useful means for imaging the gross and subtle changes to brain due to TBI. Use of such systems in and near the field should improve clinical outcome for patients suffering from TBI. Our long-term goal is to develop a field deployable brain imaging system responsive to brain stiffness. Our system would do so through the use of ultrasound applied transcranially.

INTRODUCTION – scope of the research. To met the goal of this proposal we sought to test the following hypothesis: Rodent brain after closed TBI (blast, controlled cortical impact (CCI); ischemic stroke) manifest spatial patterns of endogenous and exogenous tissue displacement, hence patterns of brain-tissue stiffness, sufficient to map and identify the extent of each of hemorrhage, edema, and TAI, as tested via the following iterative aims.

Specific Aim #1: Quantify via histology and MR the spatial position and extent of each of hemorrhage, edema and TAI within each of the blast and CCI models of brain injury.

Specific Aim # 2: Directly measure the intrinsic stiffness of brain tissue of different types: normal gray and white matter; hemorrhagic brain; edematous brain; traumatized axons.

Specific Aim # 3: Use displacement-based ultrasound to image intrinsic brain tissue stiffness of normal versus traumatized rodent brains and their component parts.

BODY

Specific Aim #1: Quantify via histology and MRI the spatial position and extent of each of hemorrhage, edema and diffuse axonal injury (DAI) within each of the blast and CCI models of brain injury, with comparable studies for ischemic stroke.

Task (1): Generate closed TBI (mild and moderate-to- severe) in rats using blast methodology.

1) Thanks to administrative issues we have delayed this task to start in summer/fall 2014

Task (2): Generate closed TBI (mild, moderate-to-severe) using CCI methodology in 'mito' mice and in rats and ischemic stroke using an occlusion model in mice.

2) As reported last year, we have achieved these goals.

Task (3): MR image rodent brains.

3) UVA has performed its all of its of MRI studies of CCI rats (Figure 1a,b). They have finished co-registration of those MR images with immunohistochemical images, in order to develop direct correlation of the brain-injury features in each imaging modality (Figure 1c). To do so, they have developed an algorithm to spatially normalize each of brain histological slides and corresponding MRI, achieved primarily through the various tools found within the Advanced Normalization Tools (ANTs) repository. Due to administrative issues this work is on hold until Summer 2014.

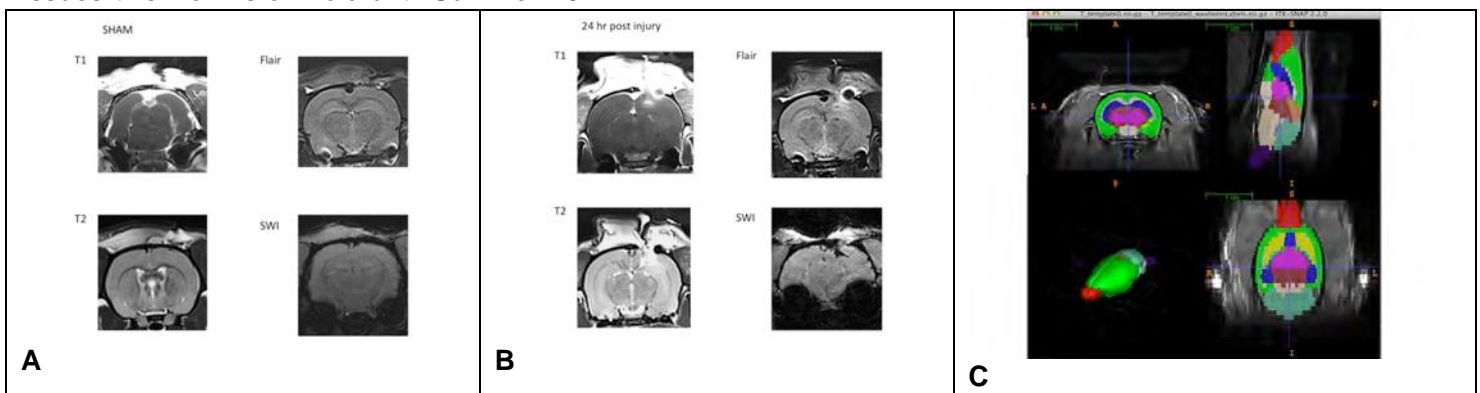


Figure 1. Images of rat brain after (sham) controlled cortical impact (CCI) injury. (A) shows various MRI images of coronal views of sham injured rat brains. **(B)** shows various comparable MRI images of injured rat brains. The injury manifests in the upper right-hand quadrant of the brain, encompasses the cortex down to the hippocampus. 'T1' highlights the basic structural abnormality generated by the CCI, 'T2' highlights fluid buildup at the site of CCI, 'Flair' refers to fluid attenuated inversion recovery that suppresses fluid-specific signals to highlight changes in tissue structure, 'SWI' refers to susceptibility weighted imaging that is sensitive to venous blood and hemorrhage. **(C)** shows co-registration of MRI images with a rat-brain atlas, each of the major components of brain highlighted in different colors. Follow-on co-registration of the atlas with histological images will complete a useful triad of MRI/Atlas/histology.

Task (4): Immunohistochemical assays.

4a) Each of UW and UVa have performed all of their immunohistochemical assays for CCI rats. At UW we are using those results to finish two papers detailing the ability of different modalities of ultrasound (shear-wave imaging (SWE) and vibro-acoustography) to detect traumatic brain injury (TBI), described below under Specific Aim #3.

4b) We at UW have collected wide field fluorescent microscopy brain-tissue images from mito-mice subjected to severe TBI via CCI (Figure 2a). (These mice have the unique property that the mitochondria within the neurons in their brain fluoresce when healthy.) We have identified unanticipated *increases* in fluorescence at the site of injury pointing to possible decreases in the ability of the neurons and axons to transport mitochondria, or, to changes in mitochondria morphology and function. Moreover, we observed changes in both ipsilateral as well as contralateral fluorescence due to injury, with comparable levels of fluorescence both acutely as well as 24 hours after injury (Figure 2b). Interestingly, we did not see this kind of damage for mild TBI (data not shown).

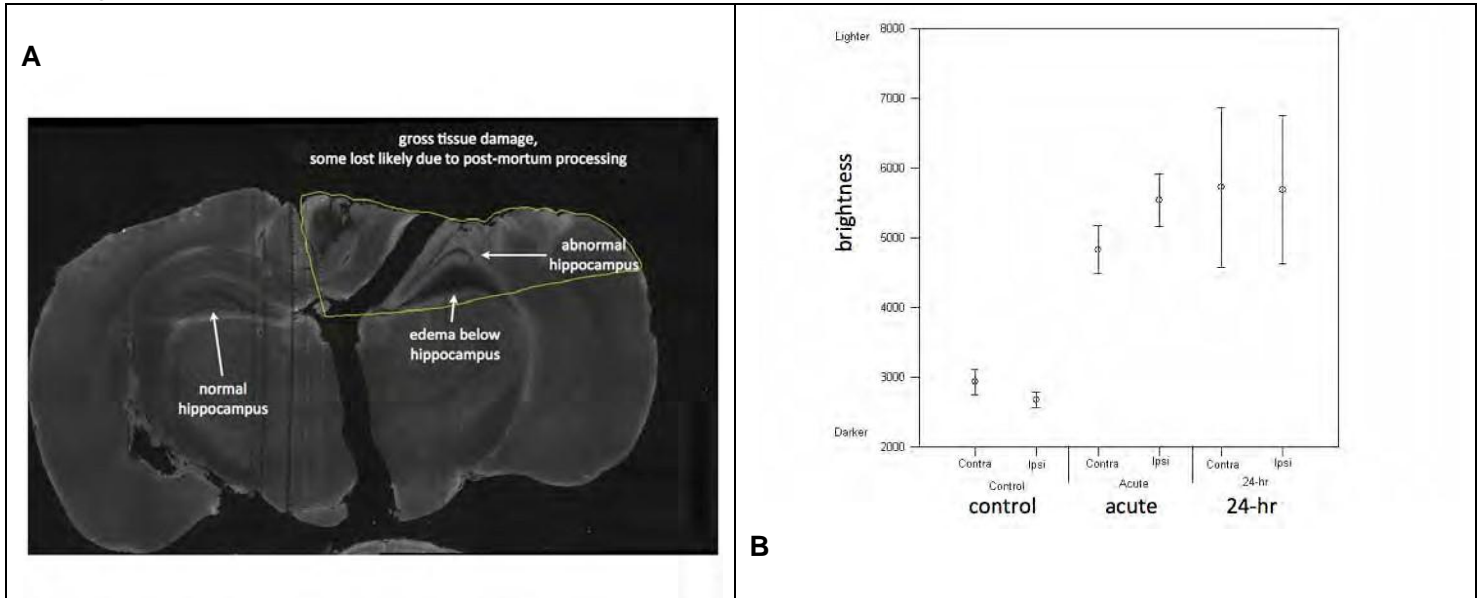


Figure 2. mitoMice brains – lighter gray has greater concentration of mitochondria than darker gray.

(A) This figure shows a coronal slice of brain subjected to actual CCI. Note the enhanced fluorescence within the hippocampus (as well as edema and large-scale necrosis), suggestive of mitochondrial dysfunction and/or reduced transport. **(B)** Averaging over all data (N = 3) we observe increase in fluorescence in both hemispheres due to a single-hemisphere contusion injury that affects axonal transport in the upper quadrants of both hemispheres.

Specific Aim # 2: Directly measure the intrinsic stiffness of brain tissue of different types: normal gray and white matter; hemorrhagic brain; edematous brain; ischemic brain; traumatized axons.

Task (5): Calibrate indenter system and apply it in vitro as well as to rodent brain tissue samples dominated by one of each of normal gray and white matter; hemorrhagic brain; edematous brain; traumatized axons.

5) This system is calibrated and working after quite extensive development of the technique. We have shown statistically significant changes in brain tissue viscoelastic structure at the site of CCI – Figure 3. We have published this paper whose results we described in detail in the last annual report – (Gabler et al, 2013 - attached).

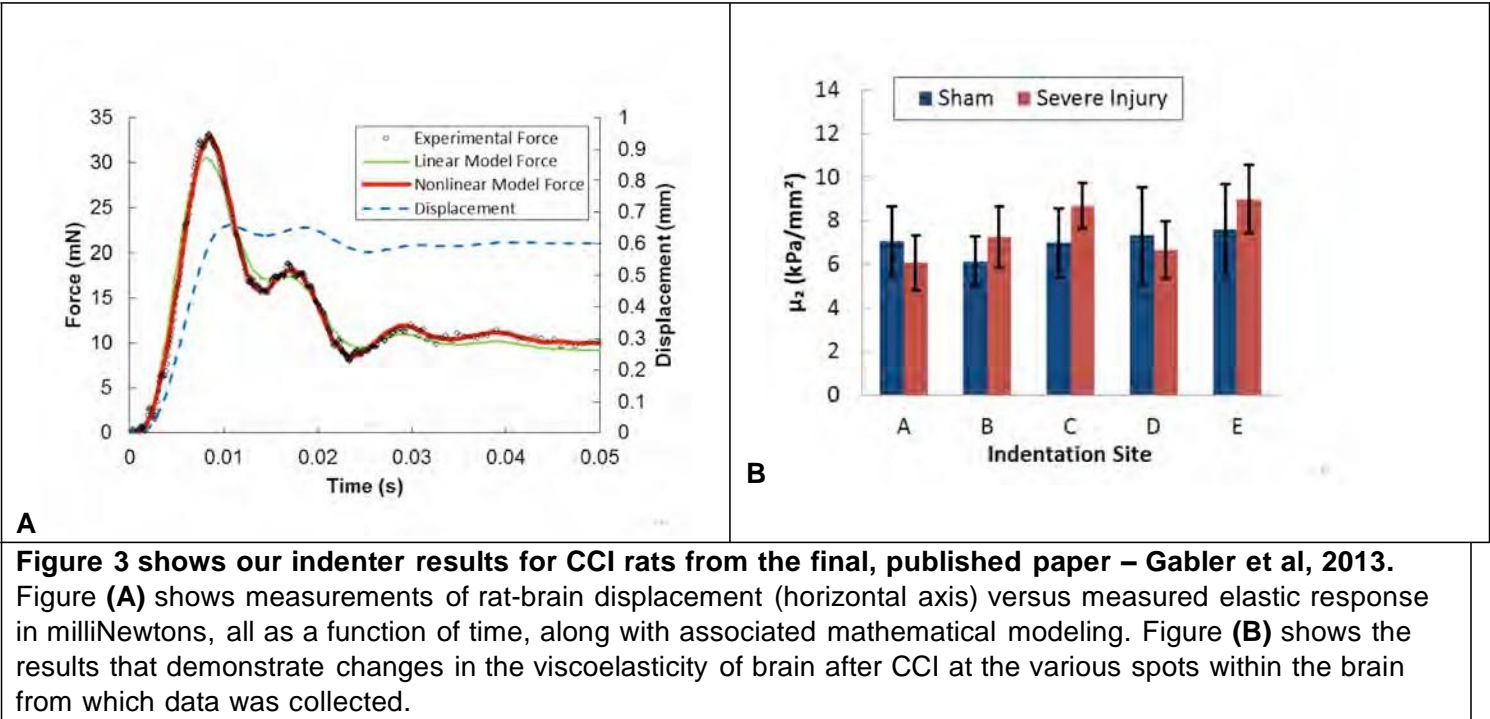


Figure 3 shows our indenter results for CCI rats from the final, published paper – Gabler et al, 2013. Figure (A) shows measurements of rat-brain displacement (horizontal axis) versus measured elastic response in milliNewtons, all as a function of time, along with associated mathematical modeling. Figure (B) shows the results that demonstrate changes in the viscoelasticity of brain after CCI at the various spots within the brain from which data was collected.

Specific Aim # 3: Use displacement-based ultrasound to image intrinsic brain tissue stiffness of normal versus traumatized rodent brains and their component parts.

Task (6): Optimize commercial ultrasound-imaging device based on measurement of exogenous and endogenous brain palpation.

6a) We have established a procedure for optimizing the analysis of images from the commercial ultrasound imaging system, based on exogenous brain palpation by the SuperSonic Imagine (SSI) machine via the acoustic radiation force and subsequent monitoring of the propagation of the shear wave. We have performed this procedure for stroke animals and published the results, where this grant supported the analysis of that data. In Figure 5 from the second annual report we described the methodology. We have now published a paper describing the application of this methodology to TBI detection in each of mice and rats, discussed below in Task 8.

Task (7): Optimize research ultrasound-imaging device based on measurement of exogenous and endogenous brain palpation.

7a) As reported earlier, we can track shear-wave propagation using our research ultrasound-imaging device (the VUE system) – Fig. 4a,b. We have used this research methodology to analyze shear-wave propagation within mouse brain *ex vivo* by varying how the shear wave entered brain (Figure 4c,d). We discuss the details of this methodology in the attached senior thesis (Yayun, 2013). We report preliminary results below.

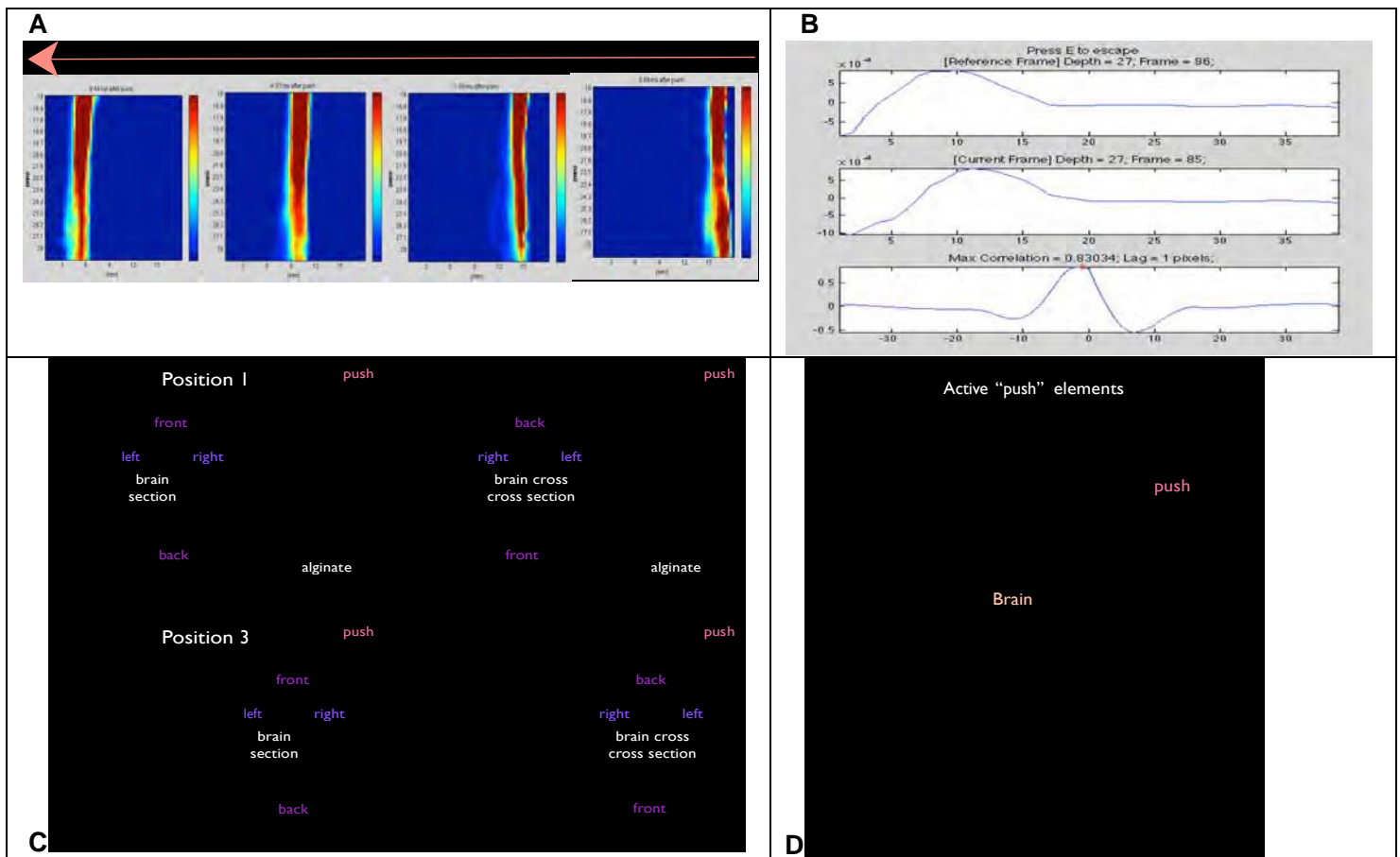
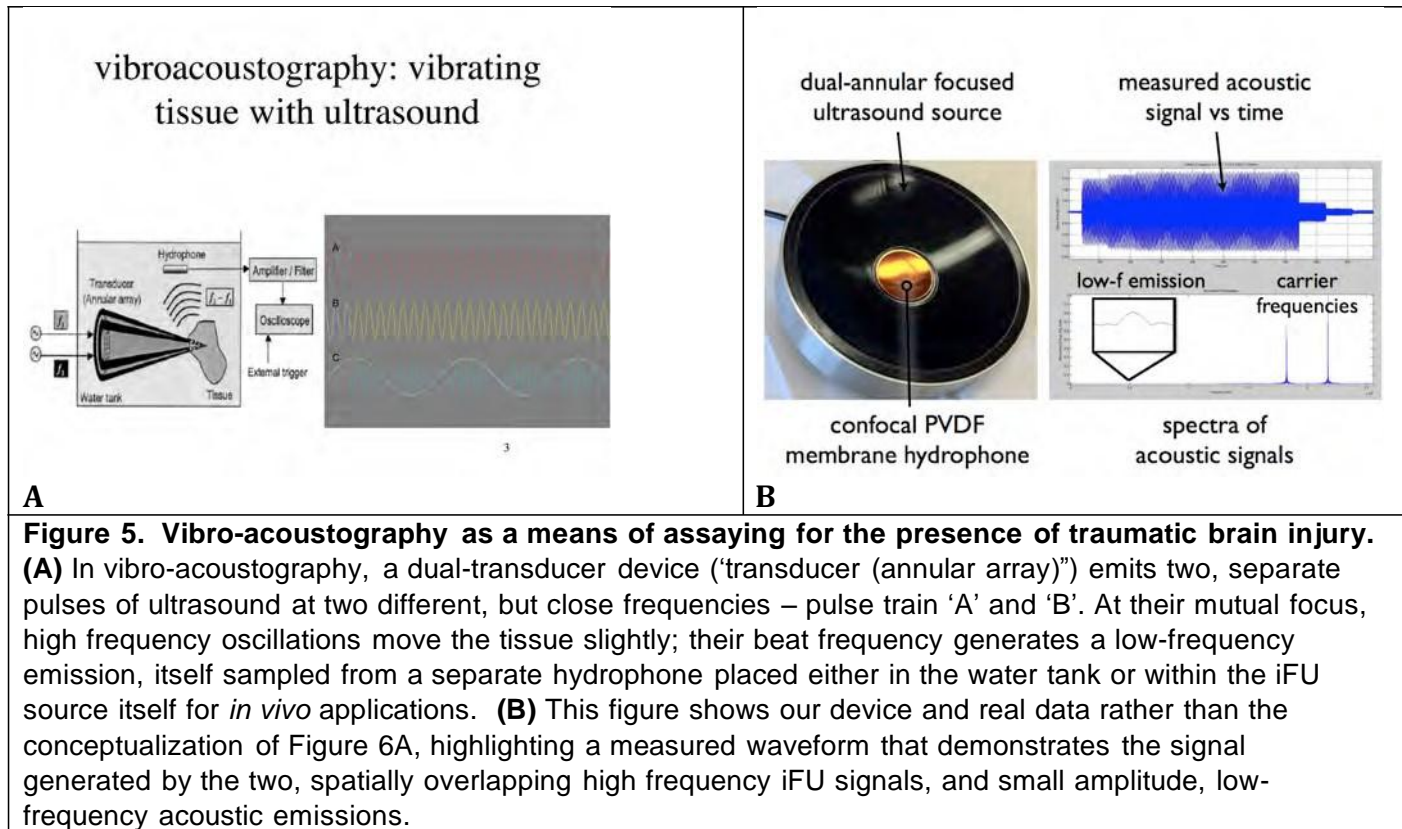


Figure 4. Quantification of shear wave propagation in alginate. We can create a focal and vertically elongated, vertical push within alginate (and tissue – below) that **(A)** generates a horizontally propagating shear wave, whose speed we can quantify and translate **(B)** through custom software that cross-correlates temporally adjacent ultrasound images along a given horizontal line. The local stiffness of tissue is proportional to the square of that local speed of the shear-wave propagation. **(C, D)** We studied shear-wave propagation into damaged brain *ex vivo* from a variety of angles relative to the injury in brain in an attempt to develop an image of the contusion injury created by the CCI mechanism.

7b) We have tested on sham and actual TBI rats, both acute and 24 hours after injury, an exogenous brain palpation system based on vibrating brain with focused ultrasound, whose methodology we review in Figure 5a and demonstrate capable of measuring acoustic emissions from brain (Figure 5b). We report results below.



7c) To create endogenous ultrasound imaging results we have demonstrated that we can measure the pulsation of mouse brains completely enclosed within their crania, pulsations created by both their breathing and their heart beat (Figure 6). Unfortunately, despite this finely detailed work we do not see a difference in pulsatility between the TBI and contralateral side of mice and rats, neither acutely nor 24 hours after injury.

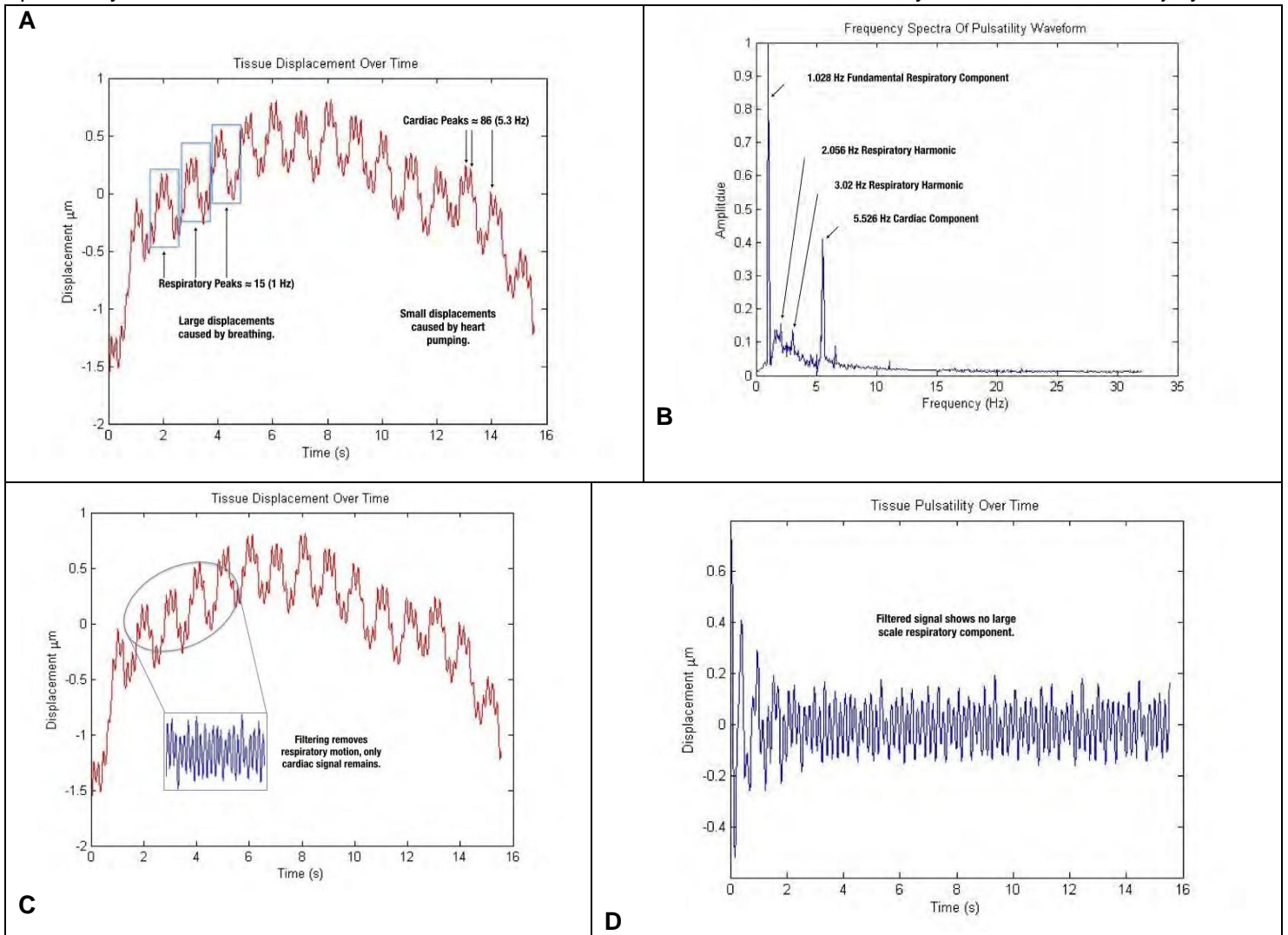


Figure 6 demonstrates our ability to collect tissue pulsatility images of mouse brain *in vivo* within the mouse's completely enclosed cranium. We developed a measure of the average brain-tissue displacement within a small portion of mouse brain, following the method of Kucewicz et al, 2006, 2007, 2008. That measure, as a function of time, demonstrates both respiratory peaks (e.g., when the mouse breathes) as well as cardiac peaks (when the heart beats), when shown in time series **(A)** or in spectral analysis as shown in **(B)**. Note that the respiratory peaks can approach 1 micron in diameter, while the cardiac peaks measure one tenth of that, on average. **(C)** Filtering out the respiratory peaks highlights the cardiac cycles only – inset of 'C' as well as **(D)**.

Task (8): Image normal versus damaged rodent brains with commercial and research ultrasound devices.

(8a) We show statistically significant variations in acoustic emissions from within severe TBI rat brain relative to sham TBI rat brain, with data collected a few millimeters away from the TBI site (Figure 7, for acute as well as for results measured 24 hours after TBI). We will finish writing up these results (Suarez et al, 2014 – see draft in Appendices) then begin design of a system capable of application to humans.

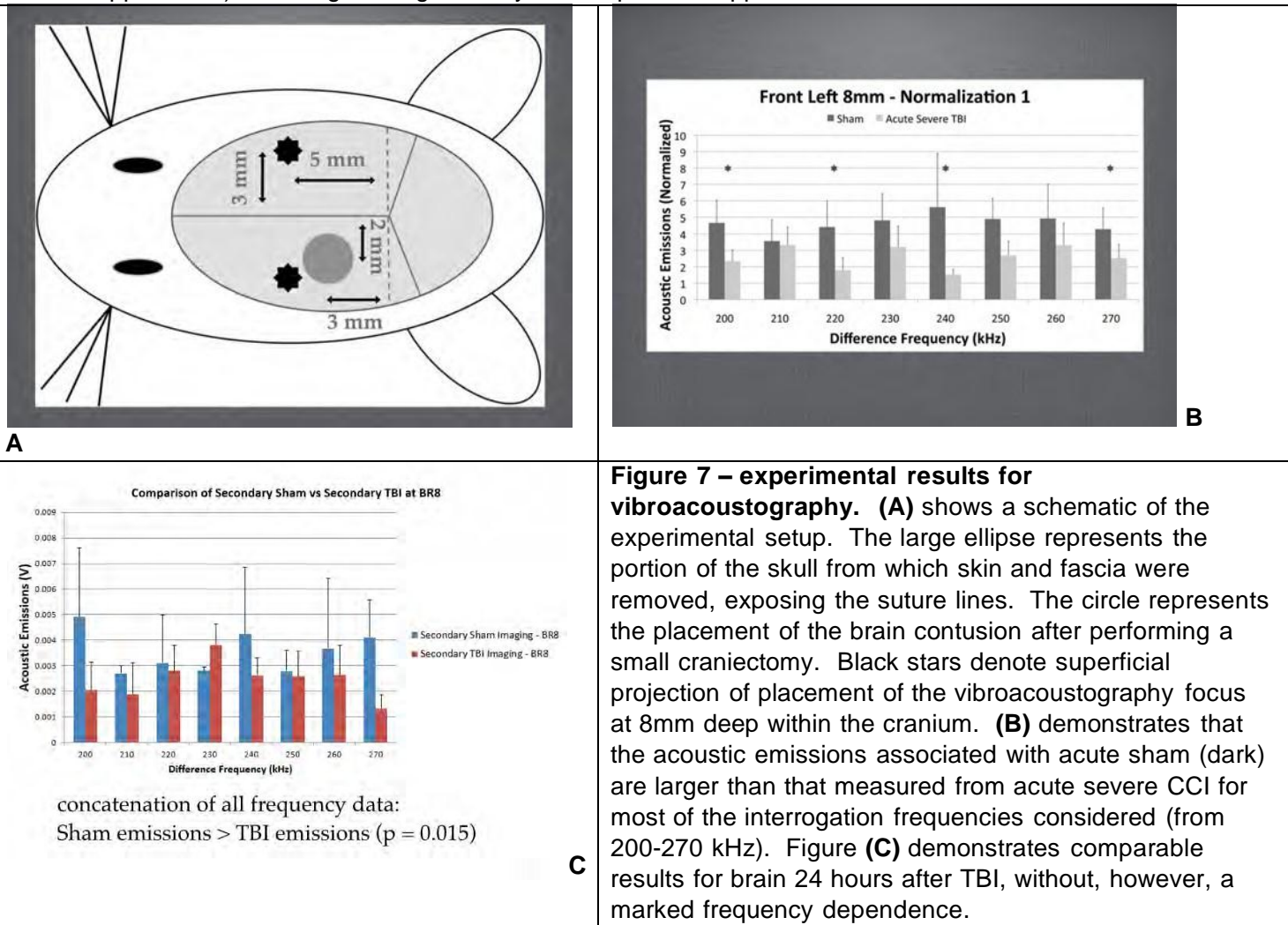
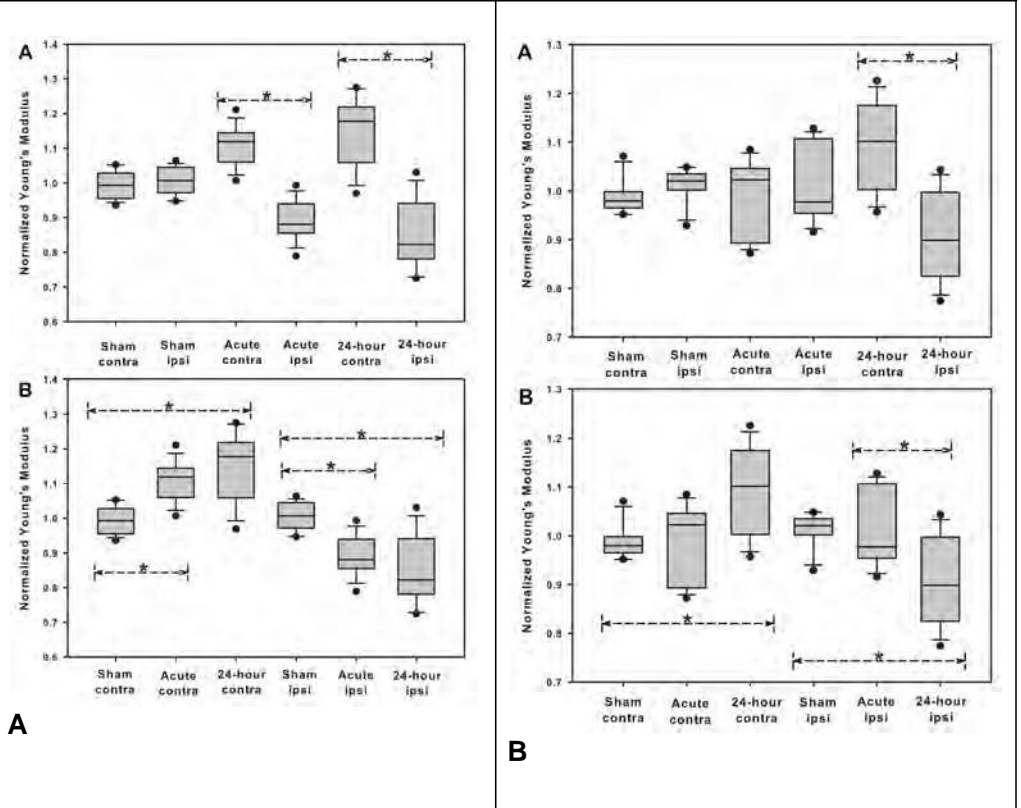


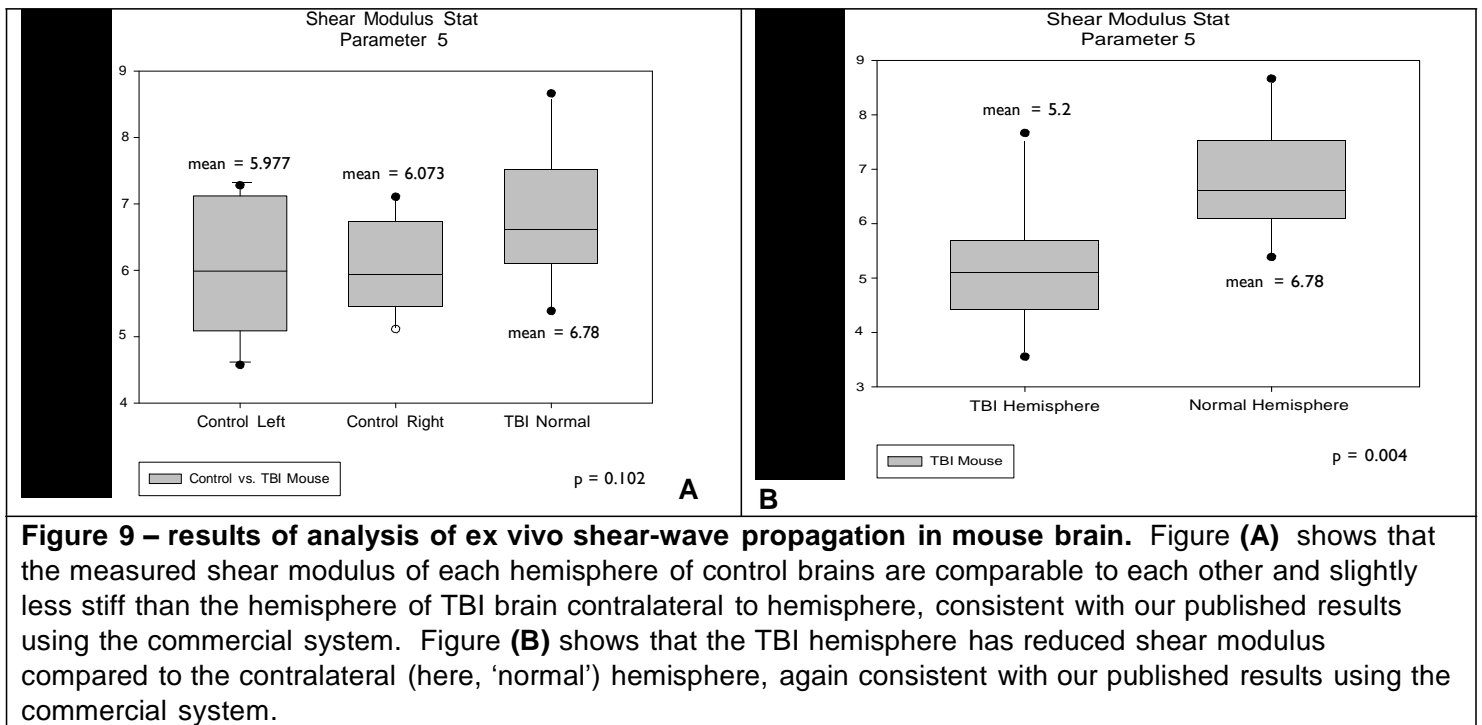
Figure 7 – experimental results for vibroacoustography. (A) shows a schematic of the experimental setup. The large ellipse represents the portion of the skull from which skin and fascia were removed, exposing the suture lines. The circle represents the placement of the brain contusion after performing a small craniectomy. Black stars denote superficial projection of placement of the vibroacoustography focus at 8mm deep within the cranium. **(B)** demonstrates that the acoustic emissions associated with acute sham (dark) are larger than that measured from acute severe CCI for most of the interrogation frequencies considered (from 200-270 kHz). Figure **(C)** demonstrates comparable results for brain 24 hours after TBI, without, however, a marked frequency dependence.

(8b) We have finished use of the commercial SSI system *without any modification* on TBI mice and rats – Figure 8, with a paper describing this work in press (Xu et al, 2014, see attachment in appendix). Specifically, these results demonstrate changes in hemispherically averaged shear modulus for each of the hemispheres due to ipsilateral TBI. The ipsilateral decrease in shear modulus relative to control is consistent with the combination of focal ischemia and wide spread edema formation after CCI, a well-established phenomenon in this animal model for TBI. Unexpectedly, we also see a contralateral increase in shear modulus relative to control by 24 hours after CCI injury, consistent with other’s observation of reduction of blood flow contralateral to injury as well as elevated global ICP.

Figure 8 demonstrates our ability to detect changes in intra-hemispheric brain stiffness after TBI using our commercial imaging system. Average values of ‘shear-modulus’ values (normalized by the average value for the entire given brain) within a hemisphere of mouse or rat brain, averaged across five (A) mice and (B) rats demonstrate that the ipsilateral hemisphere has a lower mean, normalized shear modulus than the contralateral hemisphere by 24 hours after CCI injury. These values change also relative to sham TBI values, which themselves agree between hemispheres. We see comparable values for mice, as discussed in Xu et al (2014).



(8c) We have finished use of the research VUE system on TBI mouse brain *ex vivo* – Figure 9, as described in the senior thesis (Yayun, 2013). These preliminary results suggest that we can image small brain contusions with shear-wave based methods, although translating this to transcranial results has thus-far proved quite difficult.



Task (9): Compare images of strain, and of bulk and shear modulus of blasted rat brain with histological and MR-based images of hemorrhage, edema, ischemia and TAI.

9) We intend to start this research in Summer 2014, after we deploy our VUE research device at the University of Virginia.

Task (10): Compare images of strain, and of bulk and shear modulus of brain tissue with images of bulk and shear modulus derived by assigning directly measured values of bulk and shear modulus to portions of histological images.

10) We intend to start this research in Summer 2014 after we deploy our VUE research device at the University of Virginia.

Task (11): Generate first-order specifications for a device capable of imaging TBI in humans.

11) We can now specify one of what we anticipate to be three devices capable of imaging TBI in humans. That device will emit diagnostic ultrasound with a frequency around 2 MHz, with its data analyzed via ‘tissue pulsatility imaging’ [TPI] algorithms we have developed. The other device we anticipate will involve vibro-acoustography in combination with TPI. We are less optimistic about using shear-wave methods to image transcranially.

KEY RESEARCH ACCOMPLISHMENTS

- We have developed and demonstrated *in vivo* a new means of detecting severe TBI both acutely and after 24 hours, based on generation and detection of focal, low-frequency vibration within brain via a process known as vibro-acoustography.
- We have demonstrated our enablement of a novel ultrasound-based imaging system capable of translating diagnostic ultrasound images, derived transcranially, into images of endogenous brain-tissue displacement that highlight focal TBI, based on our ability to image *mouse- and rat-brain* pulsatility. Unfortunately these results have not yet demonstrated sensitivity to the presence of TBI on length scales of millimeters.
- We have observed changes in hemispherically averaged brain-tissue stiffness in TBI generated by the controlled cortical impact (CCI) method in mice and rats consistent with physiological changes in brain observed in rodent models of TBI as well as in patients with TBI. These observations include ipsilateral edema and hemorrhage formation (observed in rodents and in patients) and short-term contralateral reduction in blood flow (observed in patients and sometimes in rodents) along with a reduction in cerebral perfusion pressure. We have a paper that describes these results in press.
- We have demonstrated in preliminary analysis that we can produce hemispheric-averaged estimates of mouse brain stiffness in a using our research device, *ex vivo*.
- We have developed a means of co-registering MR and immunohistochemical images, in order to develop direct correlation of the brain-injury features in each imaging modality. The tools we are creating to accomplish this task will likely find clinical application, for bringing together different imaging modalities for TBI and other etiologies.
- We have demonstrated our direct means of measuring brain-tissue stiffness of rat brains, data that will give us ground-truth measurements of that stiffness for comparison with our ultrasound-based means of imaging brain-tissue stiffness variations in the context of TBI.
- We anticipate deployment at UVA of a research ultrasound imaging system capable of generating tissue-pulsatility images and possibly vibroacoustography maps of the brains of rats after blast injury. Successful collection and analysis of these data, along with direct measures of brain-tissue stiffness and associated MRI and immunohistochemical images, will allow us to demonstrate in a direct fashion that we can use ultrasound to produce high-contrast images of damaged versus normal brain in the context of TBI.

REPORTABLE OUTCOMES

(copies of relevant documents are attached to the end of this document)

- Gabler LF, Stone JR, Mourad PD, Crandall JR, Salzar RS (2013) Region Specific Viscoelastic Properties of the Adult Rat Brain under Indentation following Traumatic Brain Injury, Proc. Ircobi Conf., paper no. IRC-13-52, pp. 470- 482.
- Xu JS, Yao A, Chu SS, Paun MK, McClintic AM, Murphy SP, Mourad PD. Detection of mild traumatic brain injury in rodent models using shear wave elastography: preliminary studies. In press at *Journal of Ultrasound in Medicine*.
- Yayun Chen (2013) Optimization of ultrasound elastography for diagnosis of traumatic brain injury. Senior Capstone Thesis with the Department of Bioengineering, University of Washington.
- Suarez, M, Dever D, Gu X, Illian PR, Mehic E, Mourad PD. Vibro-acoustography can detect traumatic brain injury, *in vivo*. For submission to *Ultrasound in Medicine and Biology*.

CONCLUSIONS

We have generated evidence supportive of the hypothesis that ultrasound-derived brain-tissue stiffness imaging using exogeneous 'palpation' of brain with diagnostic ultrasound can successfully detect changes in rat brain caused by both ischemic stroke and in TBI. This uses shear-wave generation and tracking via ultrasound as well as 'vibrating' brain with focused ultrasound. We have also generated evidence supportive of the hypothesis that we can detect endogeneous palpation of rodent brain by cerebral blood flow. We have made direct measurements of brain-tissue stiffness in rats *ex vivo* that show a change in brain tissue viscoelasticity due to TBI. We have completed a novel means of co-registering imaging and histological data that together highlight TBI. We have begun designs of two ultrasound systems capable of creating images of TBI in humans.

In our last extension year we will generate comparable data on blast mice and blast rats.

1 Detection of mild traumatic brain injury in rodent models using shear wave
2 elastography: preliminary studies.

3
4
5 Zinnia S. Xu¹, Anning Yao¹, Stephanie S. Chu¹, Marla K. Paun², Abbi M. McClintic³, Sean P.
6 Murphy, Ph.D.³, Pierre D. Mourad, Ph.D.^{1,2,3}.

7
8
9 ¹Department of Bioengineering
10 University of Washington
11 Box 356470
12 Seattle, WA 98195

13
14 ²Applied Physics Laboratory
15 University of Washington
16 Box 355640
17 Seattle, WA 98195

18
19 ³Department of Neurological Surgery
20 University of Washington
21 Box 356470
22 Seattle, WA 98195

23
24
25 Corresponding Author:

26 Pierre D. Mourad
27 Department of Neurological Surgery
28 University of Washington
29 Box 356470
30 Seattle WA 98195

31
32
33
34
35 (email) pierre@apl.washington.edu

36
37
38 Running title: Ultrasound elastography detection of TBI

39
40 Manuscript category: Original Research

Abstract

Objectives: Traumatic brain injury (TBI) can cause adverse physiological changes in fluid content within brain, which may lead to changes in tissue elasticity (e.g., stiffness). This study evaluated the ability of ultrasonic shear wave elastography (SWE) imaging to observe these changes in brain after TBI, *in vivo*.

Methods: Mice and rats received a mild TBI or sham surgery and were imaged acutely or 24 hours after injury using SWE and the hemispheric stiffness values were compared.

Results: Stiffness values were consistent across brain hemispheres of sham TBI rodents. By 24 hours after TBI, relative brain-tissue stiffness values for mice and rats each decreased ipsilaterally and increased contralaterally, both relative to each other and as compared to sham TBI rodents ($p < 0.05$). The absolute value of tissue elasticity increased for rats ($p < 0.05$) but not for mice.

Conclusion: Differences between intra-hemispheric stiffness values of rodent brain by 24 hours after mild TBI may reflect the observed edema and hemorrhage ipsilateral to TBI, and the known reduction of cerebral blood flow in both brain hemispheres. If these hypotheses hold true, ultrasonic shear wave elastography may offer a method to detect adverse changes in fluid content within brain after mild TBI.

Keywords: Brain; Edema; Elastography; Ultrasound; Traumatic Brain Injury;

Introduction

Incidence of traumatic brain injury (TBI) has increased significantly in recent years owing to the growing use of improvised explosive devices in operations in the Middle East [1]. TBI also occurs among civilians, primarily caused by falls, motor vehicle accidents, struck by/against events, contributing up to 30% of injury-related deaths [2].

Computed tomography (CT) and magnetic resonance imaging (MRI) are the current civilian standards for imaging traumatic brain injury, with CT more commonly available, thanks to its speed and relatively low cost. It is therefore generally used acutely, if available, while MRI finds more use a few days after initial injury because of its sensitivity to blood products [3]. Both imaging technologies are often insufficiently accessible for military TBI (Ken Curley, MD, personal communication) with the additional requirement of patient transport to the imaging site, relevant in either the civilian or military context. Transcranial ultrasound imaging offers a rapid, portable and point-of-care system for imaging brain but lacks sufficient contrast to provide much diagnostic utility [4].

Here we consider ultrasonic shear wave elastography (SWE) as a possible alternative or adjunct to CT and MRI. SWE creates images of Young's Modulus, a measure of the resistance to such that larger values describe stiffer tissue. Therefore, maps of Young's Modulus describe the spatial dependence of tissue shear elasticity or stiffness. The SWE system works by generating within tissue a rapid, net axial displacement of tissue. This spatially focal impulse force then creates a shear wave that propagates outward from the 'pushed' region [5-7]. SWE systems use diagnostic ultrasound to track the propagating shear wave, with the existing commercial system from SuperSonic Imagine (SSI) translating the square of that local speed into a local value of Young's Modulus [5].

SWE via the SSI clinical system has found well-documented use on humans for large and primarily homogenous organs such as breast [5, 8-9]. Studies exist that have used the clinical system in animal models of disease such as kidney [10] and ischemic cerebral stroke [11]. Relevant here, Xu et al [11] resolved inter-hemispheric differences in the stiffness of mouse brain after complete occlusion of the middle cerebral artery. They hypothesized that known formation of edema and ischemia due to stroke ipsilateral to the occlusion and diaschisis contralateral to the occlusion caused the observed inter-hemispheric differences in stiffness.

When using small animal models internal scatter of the shear wave can produce aliasing in stiffness images [10-12]. Indeed, Macé et al. [12] used a research version of the

SSI to remove this aliasing effect by tracking individual shear waves between scattering events. Their maps of brain-tissue stiffness displayed intra-hemispheric features in exquisite detail.

As a first step towards the goal of making SWE applicable to human brain, we used SWE images from the SSI of the brains of rats and mice that received a focal traumatic brain injury to analyze the temporal evolution of the stiffness of brain associated with that injury.

Materials and methods

All animal procedures were approved by the Institutional Animal Care and Use Committee (IACUC) of the University of Washington and the US Army Medical Research and Materiel Command (USAMRMC) Animal Care and Use Review Office (ACURO).

Animal techniques

Surgery

Fifteen male Sprague Dawley rats (250-300 grams, Charles River) and fifteen male mitoCFP mice (20-30 grams, bred at the University of Washington [13]) were used. These were divided into three experimental groups for both rats and mice: sham TBI group (n=5), acute TBI group (n=5) and 24-hour TBI group (n=5). We induced mild TBI following the controlled cortical impact (CCI) protocol of Lighthall [14] as refined by Dixon et al [15], which produced a repeatable and localizable cortical contusion.

Anesthesia was induced via inhalation isoflurane (5% isoflurane for rats; 3% for mice) and maintained (2-3% isoflurane for rats; 1-2% isoflurane for mice) during surgery and cortical impact. The surgical technique was nearly identical for rats and mice; therefore we describe the procedure generally referring to the subjects as “rodents.”

The rodent was placed in a stereotaxic device within a pneumatic controlled cortical impact device (AmScien Instruments, Richmond, VA, USA) to hold the head steady. A heating pad was used to maintain the core body temperature of approximately 37° C. The surgical site was prepared by shaving the top of the head then application of a lotion hair remover. Prior to surgery, lidocaine (1 mg/kg) was injected subcutaneously to the surgery site. For TBI rodents allowed to survive 24 hours after injury, bupivacaine (1 mg/kg) was also injected subcutaneously to the surgery site and buprenorphine (0.05 mg/kg) was delivered as an intraperitoneal injection.

After establishing an anesthetic plane via toe pinch and respiratory observation, an incision was made from the bregma to just posterior of the lambda suture line and the skull was exposed. A small (of order 1 mm) hole was drilled in the right (ipsilateral) parietal portion of the skull bone using a surgical drill (Dremel, Racine, WI). Bone rongeurs were used to enlarge the drilled hole to approximately 4 mm in diameter between the bregma and lambda of the right parietal bone of each of mice and rats. (For mice this cranial window encompassed nearly the entire cranial vault above the ipsilateral hemisphere of brain. For rats, this hole took up less than 40% of available ipsilateral cranial vault.) The cranial window was then aligned with the tip of the cortical impact device. At this point sham animals were removed from the apparatus. For TBI animals, the cortical impact device was then fired to create an impact at the surface of the brain of a velocity of 3.5 m/s and a depth of 1.0 mm for rats and 0.5 mm mice.

For sham and acute TBI rats, the ipsilateral cranial window was enlarged after impact to approximately the entire right parietal bone up to the bregma, lambda, and sagittal suture line. For mice we worked with the existing ipsilateral cranial window. For each of the sham and acute TBI rats and mice an identical cranial window was then created on the contralateral side of the skull.

For the rodents in the 24-hour TBI groups, after impact the unilateral cranial window was filled with bone wax. The surgery site was then closed with 3-0 nylon sutures (Covidien, Mansfield, MA, USA) and the rodents were returned to their cages. After 24 hours, these received bilateral craniectomies as described above.

SWE Image Acquisition

After the creation of bilateral cranial windows we imaged the brains of each rodent with a linear SL15-4 MHz transducer of an Aixplorer Multiwave Ultrasound System (SuperSonic Imagine, Aix-en-Provence, France). The transducer's imaging frequency ranged between 4.0-15.0 MHz, with a standard center frequency of 8.5 MHz. Two types of images were collected, Shear Wave Elastography (SWE) and standard B-mode. Images were collected with an elasticity range of 0-180 kPa to minimize gross imaging artifacts associated with the surrounding tissue and skull while blinding the user to intra- hemispheric features at low values of Young's Modulus, which generally lie between 2 and 25 kPa [11-12,16-18].

A micro-positioner was used to maintain the SWE transducer over the rodent's head perpendicular to show coronal slices. Multi-purpose ultrasound lotion (Polysonic, Cone

Instruments, Solon, OH, USA) was used to maintain ultrasound conduction between the transducer and the head.

The brain was first imaged using traditional B-mode; combined B-mode and SWE imaging began when the brain had been located and centered in the B-mode image (Fig. 1 A). Significant effort was made to minimize creation of imaging artifacts in the SWE images. These artifacts (e.g., Fig. 1 C,D) are areas of high Young's Modulus that do not correlate with the neuroanatomy [11-12,16-17]. For each rodent, we collected 10 – 30 images. We selected 3 images where both the impact site was identifiable in the B-mode imaging and had minimal elasticity artifacts.

After imaging the animals were sacrificed and perfused and the brains were harvested for histological analysis. The brains were sectioned through the injury site at 8-10 micron thick that were stained with hematoxylin and eosin (H&E) and, separately, cresyl violet (CV). The slides were digitized and the extent of TBI damage was quantified by manual selection of the injured area using ImageJ.

Post-processing of SWE Images

Image post-processing was completed using MATLAB (Natick, MA, USA). The entire brain region was manually selected in the SWE-mode image obtained from the Aixplorer (Fig. 1 B). The brain region in the SWE image was selected based on the structure of the skull as seen in the corresponding B-mode image.

After the selection of images, the elasticity map of the selected brain region was reduced to display an elasticity range of 0-35 kPa (Fig. 1 C,D), down from 0-180kPa (Fig. 1 A,B). Regions of interest from within each hemisphere of brain tissue within the skull were then manually selected directly from the elasticity map (Fig. 1 D). Regions of comparable size and location but free of imaging artifacts were selected from both hemispheres.

Regional selection and analysis was performed three times for each image and then averaged together to produce the intra-hemispheric average of brain-tissue stiffness for each of the two hemispheres of brain within the image.

Data Analysis

For each image for each rodent, a representative value of the Young's Modulus value of each hemisphere was used directly for analysis as well as normalized by dividing the average value of Young's Modulus for a given hemisphere by the average of the two

hemispheres. The normalized Young's Modulus therefore provides a measure of the elasticity of a given hemisphere relative to the average value across the entire brain.

Kruskal-Wallis One Way Analysis of Variance tests on Ranks (ANOVA) was applied to the data using SigmaPlot (Systat Software, San Jose CA).

Results

Quantification of areal extent of damage in H&E and Creyl Violet.

We quantified the anatomical extent of TBI damage as shown histologically (Fig. 1 E,F). There was no difference between groups with regard to the extent of damage shown by H&E versus cresyl-violet stains nor in the extent of damage between the acute and 24-hour groups for either species (Table 1).

Directly measured values of Young's Modulus for rats.

Figure 2 shows directly measured average values of Young's Modulus for each hemisphere of sham, acute, and 24-hour TBI rats. There was no significant difference between average Young's Modulus values within any of the sham or acute or 24-hour TBI groups (Fig. 2 A). We did, however, observe changes in average Young's Modulus between groups. Specifically, each of the contralateral and ipsilateral hemispheric values of the acute and 24-hour TBI groups have values of Young's Modulus that increased significantly relative to their respective values for the sham TBI group (Fig. 2 B).

Normalized values of Young's Modulus for rats.

Figure 3 shows normalized Young's Modulus values for each hemisphere of sham, acute, and 24-hour TBI rats. There was no significant difference between average Young's Modulus values within the sham or acute TBI groups while by 24 hours there existed a significant difference between ipsilateral and contralateral hemispheric averages of normalized Young's Modulus (Fig. 3 A). With regard to between-group changes, by 24 hours after TBI the ipsilateral values of normalized Young's Modulus decreased with time while the contralateral values increased with time (Fig. 3 B).

Directly measured values of Young's Modulus values for mice.

Figure 4 shows directly measured values of Young's Modulus for each hemisphere of sham, acute, and 24-hour TBI mice. There was no significant difference between average Young's Modulus values within the sham group while there exist significant differences between the average ipsilateral and contralateral values of Young's Modulus both acutely and at 24 hours after TBI (Fig. 4 A). Relative to the sham value of Young's Modulus the ipsilateral value decreased by 24 hours after TBI while the contralateral value increased acutely before returning to a value comparable to the sham value of Young's Modulus (Fig. 4 B).

Normalized values of Young's Modulus for mice.

Figure 5 shows normalized Young's Modulus values for each hemisphere of sham, acute, and 24-hour TBI mice. There was no significant difference between average Young's Modulus values within the sham group. In contrast, the average value of Young's Modulus for the ipsilateral hemisphere was significantly smaller than that of its contralateral value both acutely and at 24 hours after TBI (Fig. 5 A). In addition, by 24 hours after TBI the ipsilateral values of normalized Young's Modulus decreased with time while the contralateral values increased with time (Fig. 5 B).

Discussion

We created mild traumatic brain injury (TBI) in mice and rats using the controlled cortical impact (CCI) paradigm. We then used a commercial diagnostic ultrasound machine to measure intra-hemispheric averages of brain-tissue stiffness (the Young's modulus, a measure of shear resistance of tissue) of the brains both acutely and 24 hours after TBI induction. We presented analysis of both the absolute value and normalized values of brain stiffness, the latter documenting changes in brain-tissue stiffness relative to the average value of the entire brain at a given time point.

We note that tissue stiffness values inferred by ultrasound shear-wave elastography are sensitive to the tissue's net fluid content. For example, all else being equal more fluid as a percentage of tissue decreases the measured stiffness, while less fluid increases the measured stiffness [5]. One can appreciate this view by considering Derieppe et al. [10],

whose study of ischemia in kidney showed a decrease in SWE-derived stiffness, and Xu et al. [11], whose study of ischemia in mouse brain showed a decrease in stiffness ipsilateral to injury (a region of extensive edema) and an increase in stiffness contralateral to injury (a region of known reduced cerebral blood flow). Paraphrasing the literature analysis of Xu et al. [11], ischemic brain within a cranium doesn't sag while ischemic kidney within a belly does.

We start with our results for rats. The absolute value of Young's modulus increased through time in each of the ipsilateral and contralateral hemispheres compared to controls (Fig. 2). There exist many physiological processes that occur after TBI that can alter the fluid content of brain that may explain our observations, subject to direct testing. For example, our observed global increase in measured brain-tissue stiffness across hemispheres through time may have arisen due the combined effect of reduced peripheral blood pressure and increased in ICP, which can work together to reduce cerebral perfusion pressure (CPP) hence cerebral blood flow throughout the brain. This hypothesis is consistent with the observations of some researchers [19-20] though not all [21]. Also contributing to this net increase in brain-tissue stiffness may have been a reduction in cerebral spinal fluid (CSF) within the cranium [20]. We note that these hypotheses require that global peripheral (blood pressure) and intracranial (ICP; CPP; cerebral blood flow; CSF) processes more than compensate for the focal increase in fluid content within TBI brain ipsilateral to the injury caused by the observed edema and hemorrhage. That increase in focal fluid content may itself balance in part the focal ischemia observed by others after CCI [21]. Attention to the normalized data highlights these potentially competing, focal effects.

Specifically, we note that by 24 hours after TBI the normalized value of brain-tissue stiffness within the ipsilateral hemisphere reduced in magnitude relative to controls while its counterpart within the contralateral hemisphere increased in magnitude relative to controls (Fig. 3). Moreover, by 24 hours after TBI the ipsilateral value of normalized brain tissue stiffness was significantly reduced relative to the contralateral value. Because of our choice of normalization technique, these results document changes in brain-tissue stiffness that occur relative to the global rise in the absolute value of brain-tissue stiffness reported above.

With regard to the observed reduction in relative ipsilateral brain-tissue stiffness, we first note the presence and time course of edema and hemorrhage demonstrated by our histology (Fig. 1 E, F and Table 1) and consistent with other's observations[22-23]. In

addition to edema, others have documented ischemia measured using laser Doppler velocimetry and whole-brain autoradiography techniques. Specifically, Bryan et al. [21] observed immediate ipsilateral ischemia after severe CCI that lasted at least four hours after injury. We therefore hypothesize that the observed edema formation ipsilateral to injury by 24 hours lowered the normalized value of the measured intra-hemispheric average of brain elasticity compared to that of sham TBI in a manner that more than compensated for the likely effect of ischemia known to occur in at least severe CCI, but undocumented within our experiment, all riding on a wave of global reduction in blood flow due to elevated ICP. This complex hypothesis, besides requiring verification in future studies, is consistent with recent observations of reduced brain-tissue stiffness at the site of CCI in mice relative to the rest of the brain, based on images created with magnetic resonance elastography [24-25].

With regard to the observed increase in contralateral relative brain-tissue stiffness, our observations and those cited above show no edema formation contralateral to the injury while [19], for example, observed decreased cerebral perfusion pressure and reduced cortical perfusion contralateral to the injury, both consistent with our observations.

Our results for normalized values of brain-tissue stiffness observed for mice after TBI (Fig. 5) are consistent with what we observed for rats (Fig. 3). This suggests it possible that the same interplay of ipsilateral edema versus ischemia and global reduction in cerebral blood flow that can occur for rats may also have occurred for mice. Consistent with this idea, Lundblad et al. [26] observed after *severe* CCI significant edema in ipsilateral cortex, a reduction of cortical blood flow in ipsilateral cortex on time scales of hours to 24 hours and in contralateral cortex by 24 hours. Comparable studies are lacking for mild CCI and warrant future work.

Our measurement of the absolute value of intra-hemispheric brain-tissue stiffness of mouse brain differs significantly, however, from what we observed for rat brain. For example, ipsilateral to the injury site the absolute value of Young's modulus value decreased by 24 hours, rather than increased as for rats. Also, the absolute value of Young's modulus increased acutely contralateral to the injury as for rats, but returned to baseline values by 24 hours after TBI, unlike in rats, which continued to increase. This difference may have arisen due to the large discrepancy in areal extent between the ipsilateral craniectomy required for mice versus that for rats. Specifically, the craniectomy uncovered essentially the entire hemispheric cranial vault for mice while less than half of that vault for rats. Perhaps this relatively large craniectomy reduced the possibility of elevated ICP, hence

reduced CPP and cerebral blood flow in our mice. The mouse model may, therefore, only display the effects of intra-hemispheric dynamics (edema, local ischemia) and reduced global cerebral blood flow due to changes in systematic blood pressure rather than the additional effects of global intracranial dynamics (elevated ICP, hence a further decrease in CPP and therefore in cerebral blood flow).

Limitations

This study had several limitations due to its preliminary nature. First and foremost, we've generated a series of largely untested hypotheses regarding the possible impact on measured brain-tissue stiffness due to the relative weights of different fluid sources within brain tissue, motivated by our direct observations and the published literature. These hypotheses require direct testing. Also, out of necessity we performed a relatively large craniectomy to facilitate the CCI method for mice, which may have altered the effects of elevated ICP and reduced CPP known to occur in these animal models. Future studies should target use of larger animal models of TBI to mitigate this possible effect. In addition, we used SWE technology not optimized for rodent brain encased in a skull. The artifacts we observed associated with the skull produced elasticity values that are not consistent with other, published measurements of brain-tissue stiffness, forcing us to carefully select around these artifacts so that they did not confound our data.

Conclusion

We used ultrasound shear-wave elastography to measure absolute as well as normalized values of intra-hemispheric stiffness of rodent brain both acutely and at 24 hours after TBI via the controlled cortical impact (CCI) method. These observed changes in brain-tissue stiffness after TBI may reflect multiple physiological processes known to occur within brain after TBI caused by CCI. These processes include the initial formation of edema and hemorrhage known to develop ipsilateral to TBI and observed by us, as well as the known but un-assayed by us (a) formation of ischemia ipsilateral to TBI, (b) reduction in cerebral perfusion pressure and (c) blood flow observed both ipsilateral and contralateral to TBI. Ultrasound-based elastography may therefore offer a method to monitor subtle changes in brain after TBI.

Future work should target testing the links we have hypothesized between observed changes in brain-tissue stiffness and the underlying physiology of TBI. In addition,

future work should address currently identified problems in the translation of this technology to human use, including delivery in a transcranial fashion of a shaped pulse of ultrasound energy sufficient to generate usefully observable shear waves, and the known large-scale anisotropy of human brain and its likely impact on the formulae used to translate shear-wave propagation into estimates of brain-tissue stiffness.

Acknowledgements

We received support for this work from the Congressionally Directed Medical Research Program (CDMRP), Award Number W81XWH-11-2-0109.

379 **Table 1**

Table 1: % extent of damage of TBI in histological analysis.				
Stain	Acute Mice	24 Hr Mice	Acute Rats	24 Hr Rats
H&E	8.02% +/- 2.2%	14.2% +/- 7.5%	4.62% +/- 2.7%	7.57% +/- 1.6%
CV	8.33% +/- 0.6%	11.2% +/- 2.7%	4.95% +/- 0.1%	6.98% +/- 2.1%

380

381

382

383

Figures

Fig. 1. Image Processing. (A) Aixplorer images in SWE mode (top) and B-mode (bottom) (B) The brain region was selected from the elastographic image (0-180 kPa) with reference to the B-mode image. (C) The SWE image of the brain was rescaled to 0-35 kPa to enhance the contrast. (D) Regions of Interest selected manually to avoid skull and artifacts (large values of Young's Modulus greater than that of brain). (E) Hematoxylin and Eosin and (F) Cresyl Violet staining of corresponding brain.

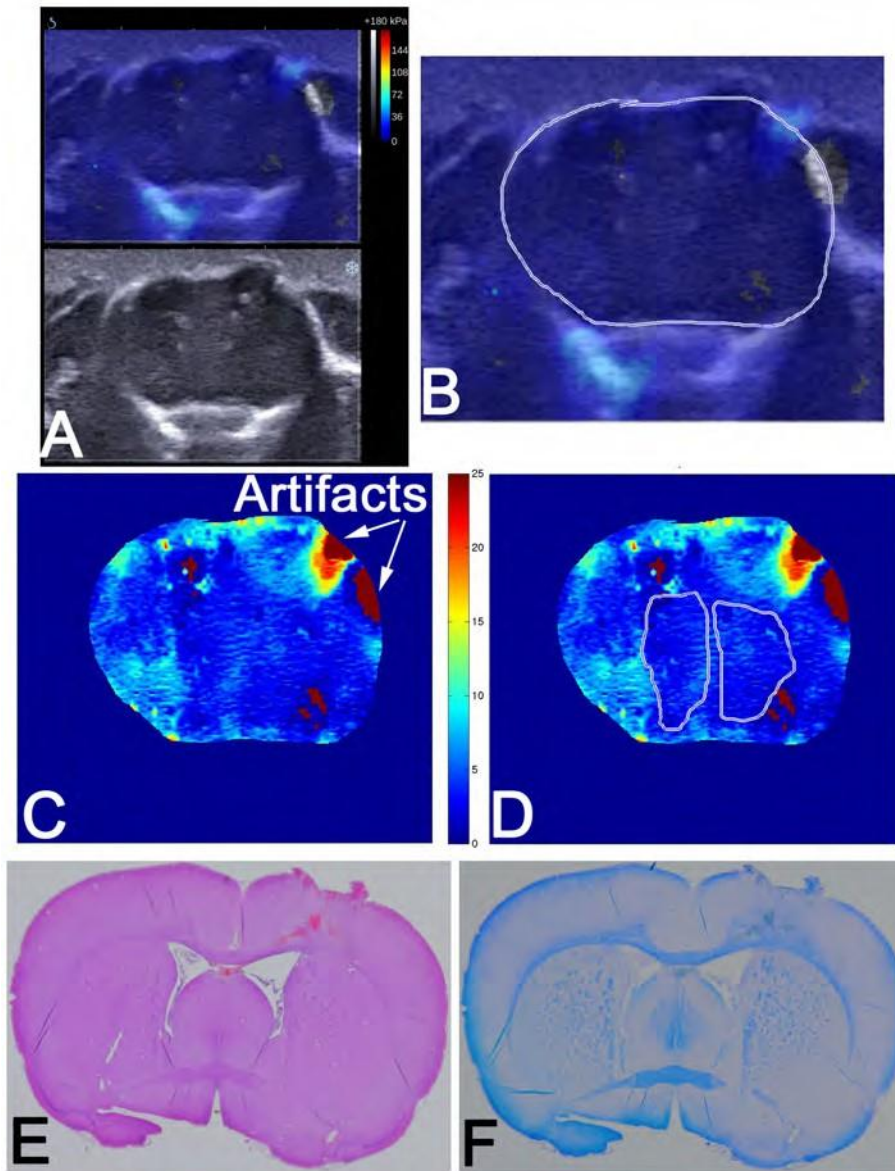


Fig. 2. Directly measured values of Young's Modulus for ipsilateral and contralateral hemispheres of the brains of rats for all test groups. * = $p < 0.05$ between the two indicated groups.

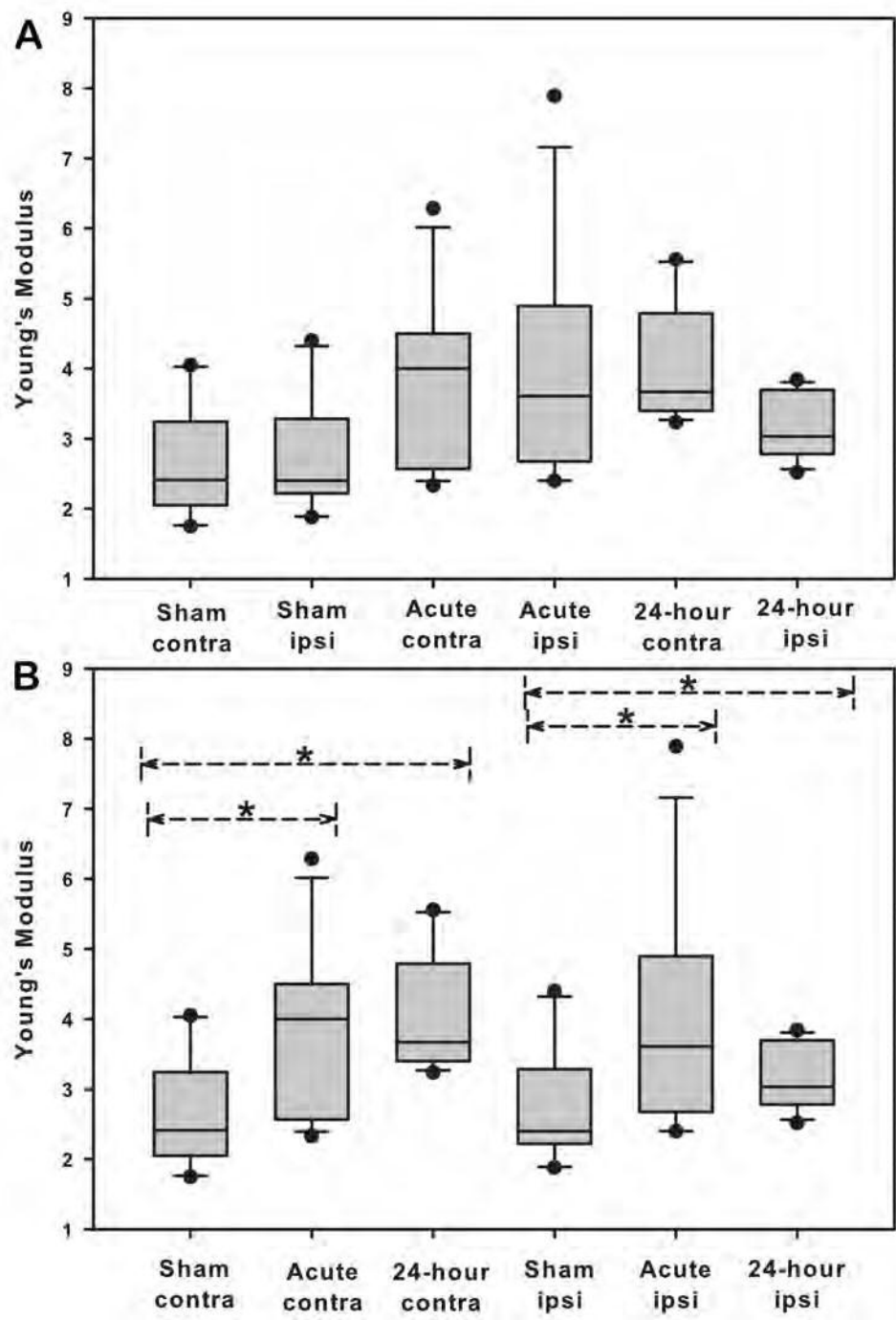


Fig. 3. Values of normalized Young's Modulus for ipsilateral and contralateral hemispheres of the brains of rats for all test groups. * = $p < 0.05$ between the two indicated groups.

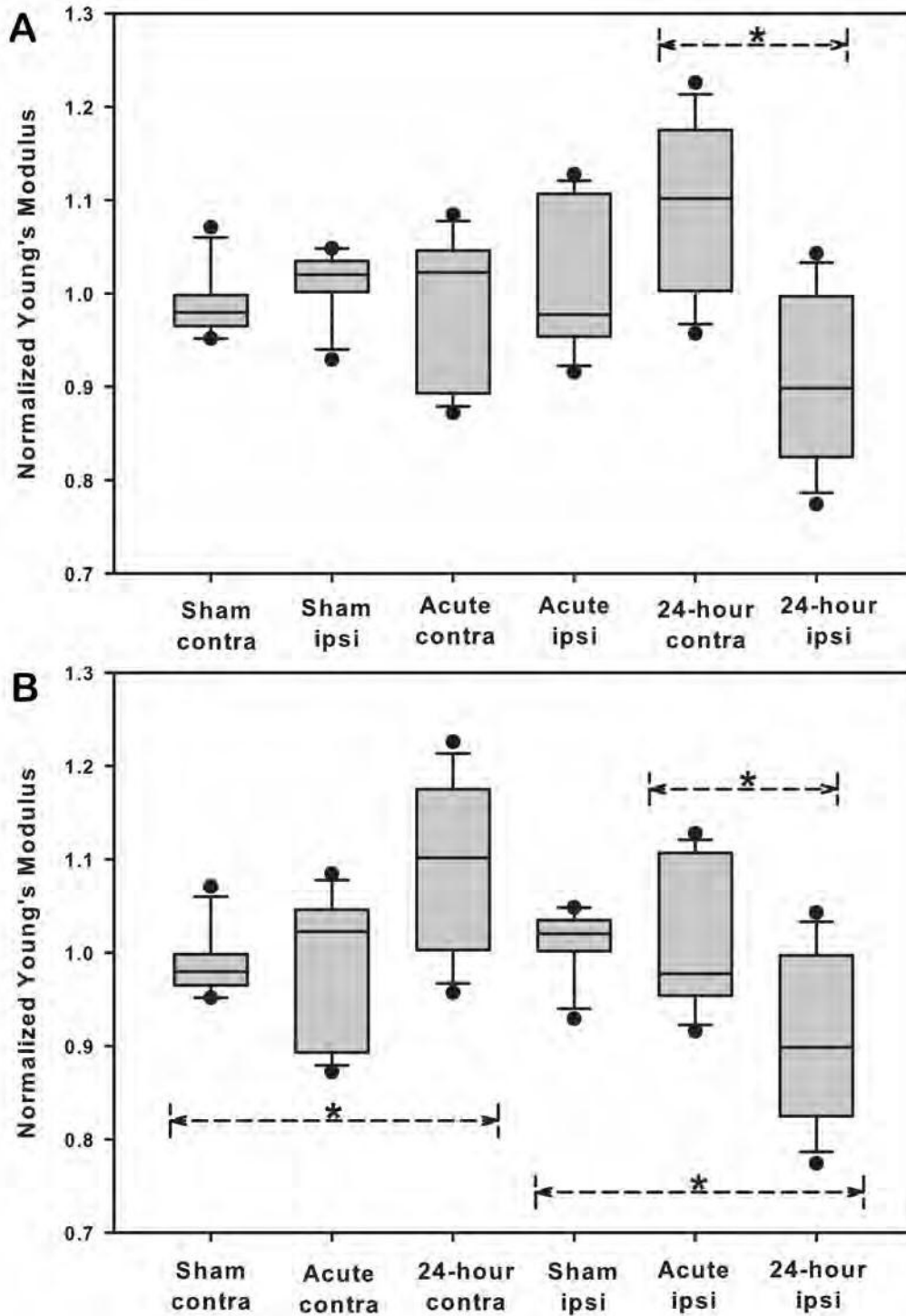
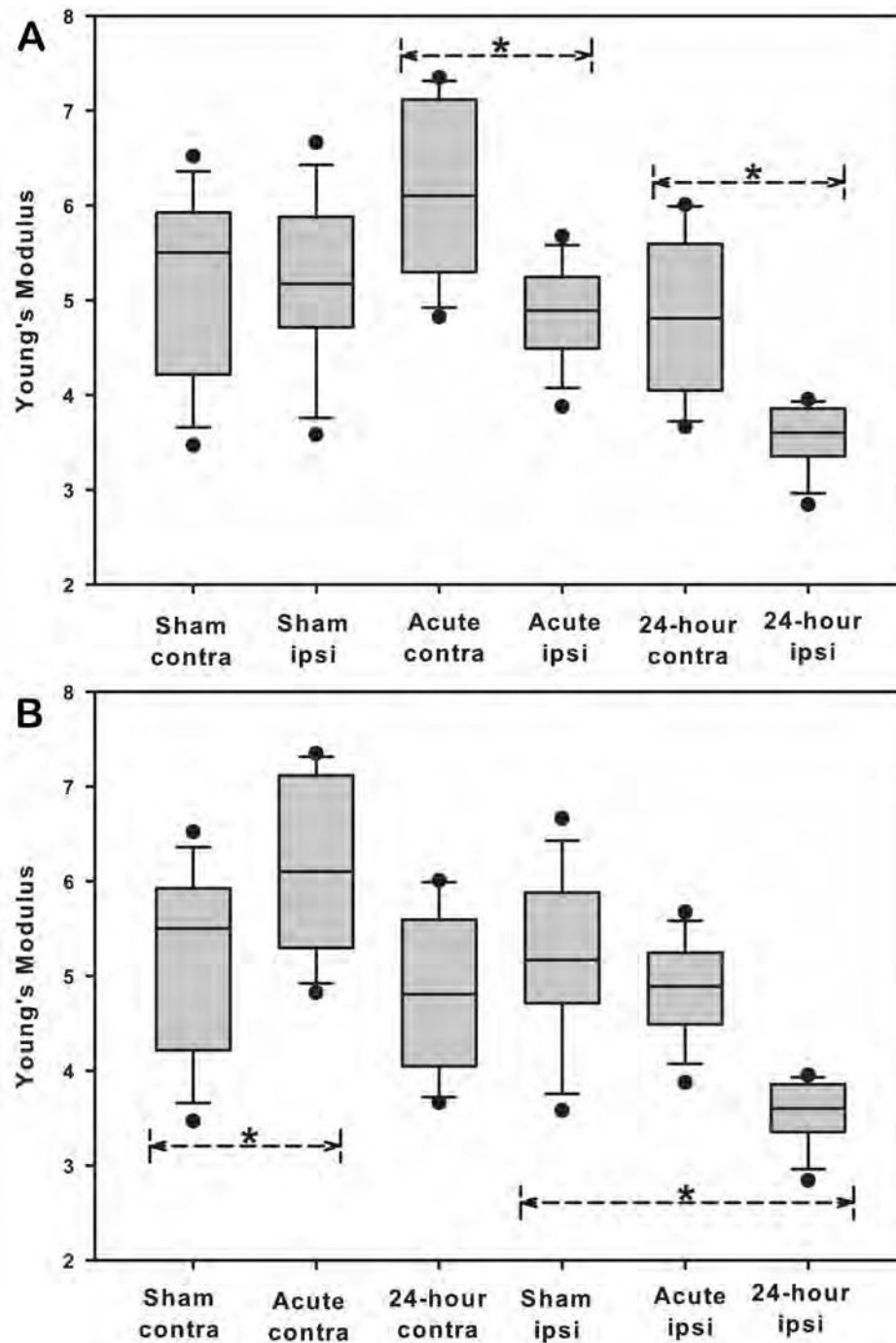
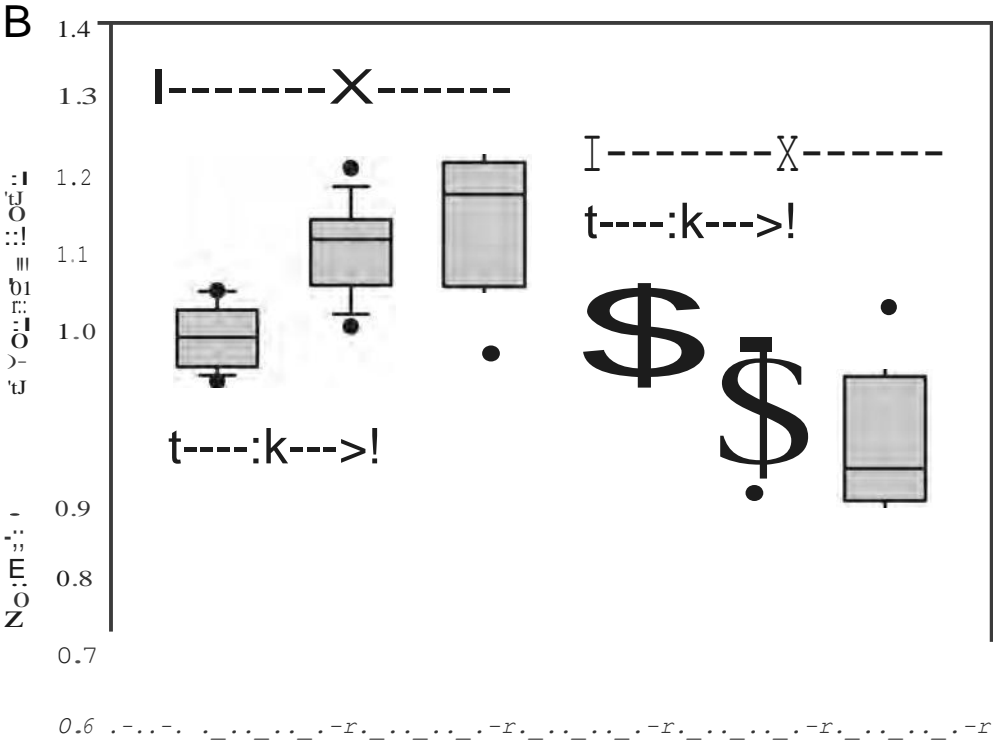
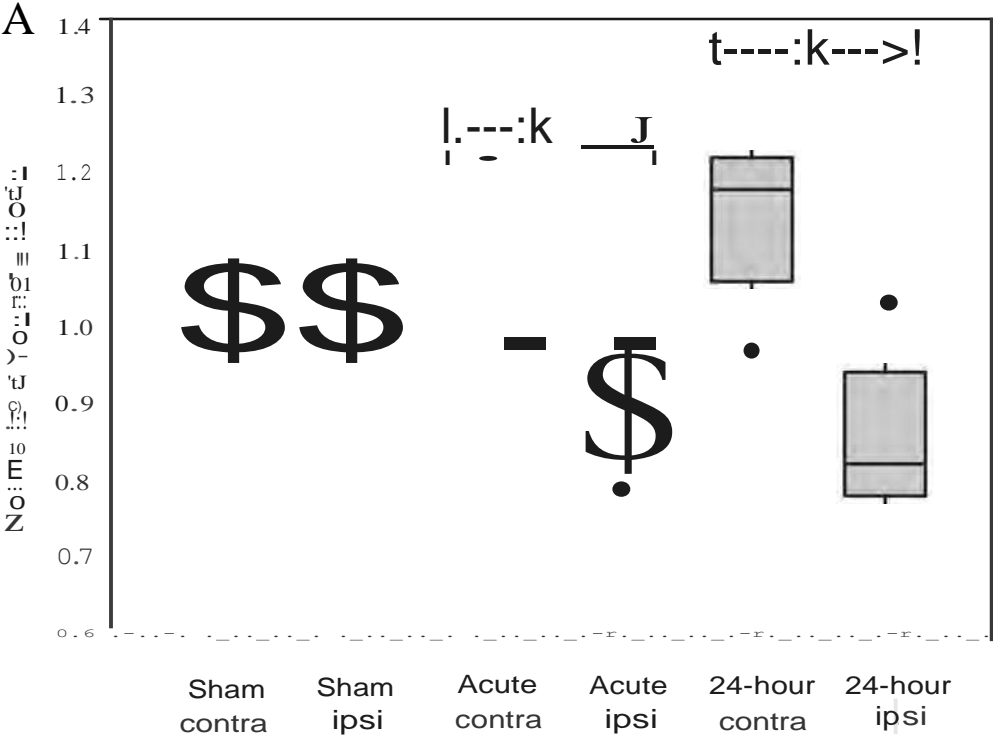


Fig. 4. Directly measured values of Young's Modulus for ipsilateral and contralateral hemispheres of the brains of mice for all test groups. * = $p < 0.05$ between the two indicated groups.



414 Fig. 5. Values of normalized Young's Modulus for ipsilateral and contralateral hemispheres
415 of the brains of mice for all test groups. * = p < 0.05 between the U.Vo indicated groups.
416



Sham contra	Acute contra	24-hour contra	Sham ipsi	Acute ipsi	24-hour ipsi
----------------	-----------------	-------------------	--------------	---------------	-----------------

References

1. Meyer K, Helmick K, Doncevic S, and Park R. Severe and Penetrating Traumatic Brain Injury in the Context of War. *J Trauma Nurs* 2008; 15:185-189.
2. Faul M, Xu L, Wald MM, Coronado VG. Traumatic brain injury in the United States: emergency department visits, hospitalizations, and deaths. Atlanta (GA): Centers for Disease Control and Prevention, National Center for Injury Prevention and Control; 2010.
3. Lee B and Newberg A. Neuroimaging in Traumatic Brain Imaging. *NeuroRx* 2005; 2:372-383.
4. Fryback DG, Thronbury JR. The Efficacy of Diagnostic Imaging. *Med Decis Making* 1991; 2:88-94.
5. Tanter M, Bercoff J, Athanasiou A, Deffieux T, Gennisson JL, Montaldo G, Muller M, Tardivon A, and Fink M. Quantitative assessment of breast lesion viscoelasticity: initial clinical results using supersonic shear imaging. *Ultrasound Med Biol* 2008; 34:1373-86.
6. Deffieux T, Gennisson JL, Larrat B, Fink M, Tanter M. The variance of quantitative estimates in shear wave imaging: theory and experiments. *IEEE Trans Ultrason Ferroelectr Freq Control* 2012; 59(11):2390-410.
7. Gennisson JL, Deffieux T, Fink M, Tanter M. Ultrasound elastography: principles and techniques. *Diagn Interv Imaging* 2013; 94(5):487-95.
8. Athanasiou A, Tardivon A, Tanter M, Sigal-Zafrani B, Bercoff J, Deffieux T, Gennisson JL, Fink M, and Neuenschwander S. Breast lesions: quantitative elastography with supersonic shear imaging--preliminary results. *Radiology* 2010; 256:297-303.
9. Garra BS. Elastography: current status, future prospects, and making it work for you. *Ultrasound Q* 2011; 27:177-86.
10. Derieppe M, Delmas Y, Gennisson JL, Deminière C, Placier S, Tanter M, Combe C, and Grenier N. Detection of intrarenal microstructural changes with supersonic shear wave elastography in rats. *Eur Radiol* 2012; 22:243-50.
11. Xu ZS, Lee RJ, Chu SS, Yao A, Paun MK, Murphy SP, Mourad PD. Evidence of Changes in Brain Tissue Stiffness After Ischemic Stroke Derived From Ultrasound-Based Elastography. *J Ultrasound Med* 2013; 32:485-494.
12. Macé E, Cohen I, Montaldo G, Miles R, Fink M, and Tanter M. In vivo mapping of brain elasticity in small animals using shear wave imaging. *IEEE T Med Imaging* 2011; 30:550-8.
13. Misgeld T, Kerschensteiner M, Bareyre FM, Burgess RW, and Lichtman JW. Imaging axonal transport of mitochondria *in vivo*. *Nat Methods* 2007; 4(7):559-561.
14. Lighthall JW. Controlled cortical impact: a new experimental brain injury model. *J Neurotrauma* 1988; 5(1):1-15.
15. Dixon CE, Clifton GL, Lighthall JW, Yaghmai AA, Hayes RL. A controlled cortical impact model of traumatic brain injury in the rat. *J Neurosci Meth* 1991; 39:253-262.
16. Green MA, Bilston LE, and Sinkus R. In vivo brain viscoelastic properties measured by magnetic resonance elastography. *NMR Biomed* 2008; 21:755-64.
17. Kruse SA, Rose GH, Glaser KJ, Manduca A, Felmlee JP, Jack CR Jr., and Ehman RL. Magnetic resonance elastography of the brain. *Neuroimage* 2008; 39:231-7.
18. McCracken PJ, Manduca A, Felmlee J, Ehman RL. Mechanical transient-based magnetic resonance elastography. *Mag Reson Med* 2005; 53(3):628-39.

19. Cherian L, Robertson CS, Contant CF Jr., Bryan RM Jr. Lateral Cortical Impact Injury in Rats: Cerebrovascular Effects of Varying Depth of Cortical Deformation and Impact Velocity. *J Neurotrauma* 1994; 11(5):573-585.
20. Colgan NC, Cronin MM, Gobbo OL, O'Mara SM, O'Connor WT, Gilchrist MD. Quantitative MRI Analysis of Brain Volume Changes due to Controlled Cortical Impact. *J Neurotrauma* 2010; 27:1265-1274.
21. Bryan RM Jr., Cherian L, Robertson C. Regional Cerebral Blood Flow After Controlled Cortical Impact Injury in Rats. *Anesth Analg* 1995; 80:687-95.
22. Baskaya MK, Dogan A, Temiz C, and Dempsey RJ. Application of 2,3,5-triphenyltetrazolium chloride staining to evaluate injury volume after controlled cortical impact brain injury: role of brain edema in evolution of injury volume. *J Neurotrauma* 2000; 17:93-9.
23. Elliott MB, Jallo JJ, and Tuma RF. An investigation of cerebral edema and injury volume assessments for controlled cortical impact injury. *J Neurosci Meth* 2008; 168:320-4.
24. Boulet T, Kelso ML, Othamn SF. Microscopic magnetic resonance elastography of traumatic brain injury model. *J Neurosci Meth* 2011; 201:296-306.
25. Boulet T, Kelso ML, Othman SF. Longterm *in vivo* imaging of viscoelastic properties of the mouse brain following controlled cortical impact. *J Neurotrauma* 2013; 30(17):1512-20.
26. Lundblad C, Grande PO, and Bentzer P. A mouse model for evaluation of capillary perfusion, microvascular permeability, cortical blood flow, and cortical edema in the traumatized brain. *J Neurotrauma* 2004; 21:741-53.

Region Specific Viscoelastic Properties of the Adult Rat Brain under Indentation following Traumatic Brain Injury

Lee F. Gabler, James R. Stone, Pierre D. Mourad, Jeff R. Crandall, Robert S. Salzar

Abstract Traumatic Brain Injury (TBI) is a serious health epidemic that places high societal and economic burdens on victims and their caregivers. Further, the associated neuropathological consequences that result from TBI are often complex and cause secondary injuries that are focal, diffuse and time dependent. Current computational models can predict loading and deformation associated with TBI; however, accurate knowledge of region specific material properties from both healthy and mechanically damaged brain is needed. In this study, the mechanical properties of both uninjured and traumatically injured brain tissue are presented. Adult male Sprague-Dawley rats were injured through a controlled cortical impact protocol. Ramp and hold indentation tests were performed at five locations on the surface of tissue samples excised from whole brain specimens. Force displacement data were analyzed using quasi-linear viscoelastic theory. An analysis revealed the tissue to be viscoelastic and spatially nonlinear with mechanical properties that depend on both region and level of injury. After normalizing the data, the nonlinear components of the instantaneous elastic force and shear modulus were found to be significantly lower, 26%, in the region containing the contusion cavity on severely injured samples compared to uninjured tissue at the same region in controls.

Keywords Traumatic brain injury, focal, diffuse, controlled cortical impact, mechanical damage, quasi-linear viscoelasticity

I. INTRODUCTION

Traumatic Brain Injury (TBI) is an important national health concern in the United States [1]. Approximately 1.7 million incidences and 52,000 deaths are reported annually due to automobile collisions, sports accidents, falls, and other head impacts [1]. Further, severe TBI has a high economic burden, costing nearly \$76.5 billion each year in medical and societal costs [1]. On the battlefield, improvised explosive devices have led to TBI in as many as 62% of soldiers sustaining head injuries, and an estimated 360,000 service members have been affected by TBI over the past decade [2], [3]. Since the 1960s there has been a dramatic improvement in understanding the complex pathobiological behavior associated with TBI [4]. Brain injury, as a result of an impact or insult to the head, leads to a number of complex neuropathological consequences that result in further tissue dysfunction and eventually cell death [5]. However, injury quantification remains challenging because the neurochemical cascades that accompany TBI often involve complex secondary sequelae that are focal, diffuse, and time dependent [6]. A better understanding of the mechanical response of the brain during these events would improve diagnosis and treatment of TBI in both clinical and battlefield scenarios.

The material properties of brain during an injurious event were studied as early as the 1940s [7]. Not until more recently has an emphasis been placed on understanding the complex mechanical behavior of the brain during loadings that lead to TBI. Much of this can be attributed to an increase in awareness of the damaging, long-term effects following even mild brain injuries [1]-[3]. Material properties of brain are reported in the literature as viscoelastic [8]-[13], both spatially and temporally non-linear [9], [10], anisotropic [11], age-dependent [11]-[14], inhomogeneous [12], [13] and nearly incompressible [15]. Additionally, experimental factors such as specimen preparation, temperature [16] and level of hydration [14], [17] have been shown to influence these properties. There is considerable variation in the mechanical response reported in these

studies. Much of this variation can be attributed to differences in the type of species, experimental protocols, and anatomical regions tested. Still, no definitive set of material properties exist for brain.

Computational models of TBI are commonly used to study the mechanical behavior of brain tissue during a traumatic event. Finite element modeling (FEM) can predict loading of various substructures through simulations of mild to severe TBI in rat brain [18]. These simulations have the added capability of predicting injury, because model-prediction of tissue strains were shown to correlate well with experimentally determined strain and strain rate injury tolerance criterion [19]-[21]. For more region-specific predictions of injuries, local material properties, including both traumatically injured and healthy brain tissue, need to be determined. Such knowledge would provide existing computational models with the added ability to predict the subsequent mechanical response of damaged tissue and allow for a better understanding of brain excitotoxicity beyond that of the initial trauma.

A survey of the literature revealed a number of studies that report thresholds for axonal damage. The reported mechanical limits for diffuse axonal injury are between 0.1-0.2 Lagrangian strain at strain rates greater than $10s^{-1}$ [9], [19]-[22]. However, there is little information regarding changes in the mechanical properties of traumatically injured brain tissue. Shafieian et al. [23] used an impact acceleration model (IAM) to generate diffuse axonal injury (DAI) in the brainstem of adult male Sprague-Dawley (SD) rats. They reported a 35% reduction in the linear coefficient of the instantaneous shear modulus in injured rats compared to uninjured controls. Saxena et al. [24] studied traumatic spinal cord injury in adult female SD rats over the course of 2 and 8 weeks post injury. They observed a 50% reduction in elastic modulus for injured compared to healthy tissue. The goal of this study is to acquire accurate, region-specific material properties for both traumatically injured and uninjured rat brain to better understand the mechanical behavior of damaged tissue and to improve existing models of TBI.

II. METHODS

Animal Injury

All animal protocols were approved by the University of Virginia's Institutional Animal Care and Use Committee. Twenty adult male SD rats of average weight (mean \pm SD), (320 \pm 27)gram, underwent surgical procedures for this study. Anesthesia was induced with a mixture of 4% isoflurane and 100% medical grade O₂ for 3-4 minutes in an induction chamber. Once the animals were sedated, the level of isoflurane was reduced to 2-2.5% and maintained for the duration of the surgery. The animals were then placed in a stereotaxic reference device (MyNeuroLab Leica Digital Stereotaxic Instrument, Leica Biosystems, Richmond, IL) and prepared for injury. A midline scalp incision was made along the forehead of each animal. The skin and underlying soft tissue were retracted exposing the sagittal, coronal, and lamboid sutures on the skull. A 4.5-5mm diameter hole was drilled from the skull above the right cerebral cortex exposing the dura at the coordinates of injury: A = -4mm bregma and L = 2mm (Ideal Micro-Drill™, Harvard Apparatus, Holliston, MA). An electromagnetically driven controlled cortical impact (CCI) device (MyNeuroLab Leica Impact One, Leica Biosystems, Richmond, IL) was used to deliver repeatable, severe, open head injury to nine of the animals; the remaining animals were prepared for *Sham* injury and used as controls. The 2mm diameter impact cylinder was positioned directly on the dura at the coordinates of injury. Contact between the probe tip and dura was verified via an electric circuit. The probe tip was then retracted from the dura and injury parameters were inputted to the device. Severe traumatic brain injury was delivered to the right ipsilateral cortex through a rapid 2.5mm compression of the dura, sustained for 200ms, with an initial impact velocity of 3.5m/s. In the instance of *Sham* injury, the impact probe was retracted from the dura, but no impact was performed on the tissue. The animals were then resuscitated and monitored for a period of twenty-four hours after which they were sacrificed and their brain tissue immediately collected.

Sample Preparation

Whole brain specimens were prepared for indentation tests immediately following tissue collection. To reduce the effects of temperature and level of hydration on the results, specimens were submerged in a physiological buffer (Millonig's Phosphate Buffer) for five minutes at room temperature (19-20)°C. Hydrated specimens were then placed into a coronal slice matrix (Braintree Scientific, Inc.) with incision planes spaced 1mm apart. Tissue cross-sections were cut to approximately 8mm in thickness from each whole brain specimen

using a 0.23mm thick razor blade (VWR Scientific, Media, PA). To accomplish this, two incisions were made in the coronal plane and parallel to each other. The first incision was made 1mm posteriorly to the injury plane at -5mm bregma and the second 8mm anteriorly to the first at 3mm bregma. In both Sham and severely injured specimens, the injury plane was identified by petechial hemorrhage on the dorsal surface of the tissue. However, in the case of a severe injury, the hemorrhage was more extensive and included a *contusion cavity*. Samples were then removed from the slicing matrix and placed on an aluminum test stage with the 5mm bregma coronal plane oriented upwards. The thickness of each sample deformed approximately 1mm under its own weight. The weight and dimensions of each sample were measured and recorded.

The coordinates of five regions, A-E, on the samples were determined using a stereotaxic reference frame [25] and are illustrated in Figure 1. Substructures of the brain under the indenter at these coordinates included both healthy and damaged tissue within the cerebral cortex, corpus callosum, hippocampus and midbrain. For severely injured samples, region A was located directly over the contusion cavity and within the injured hemisphere of the brain. Samples were assumed to be symmetric about the cerebral fissure, and regions B and D were located contralateral to regions A and C, respectively. Region E was positioned at approximately the center of the sample on the aqueduct. Coordinates were normalized to account for differences in the cross-sectional dimensions between samples due to intra-specimen variability. The normalization was performed by making length and width measurements on the cross-section of each sample; the five indentation coordinates were then multiplied by the ratio of the cross-sectional dimensions of the first sample tested under this protocol, ID NIB00287, to those of the sample of interest; the normalized coordinate locations were then dimensioned from region E using digital micrometers. Evan's Blue Dye was used to mark each coordinate on the tissue cross-section for a visual reference onto which the indenter could be positioned. The amount of dye under the indenter was assumed to have a negligible effect on the tissue properties. A total of 30 minutes were allotted for sample preparation, i.e. from the time of tissue collection to the time indentation testing began.

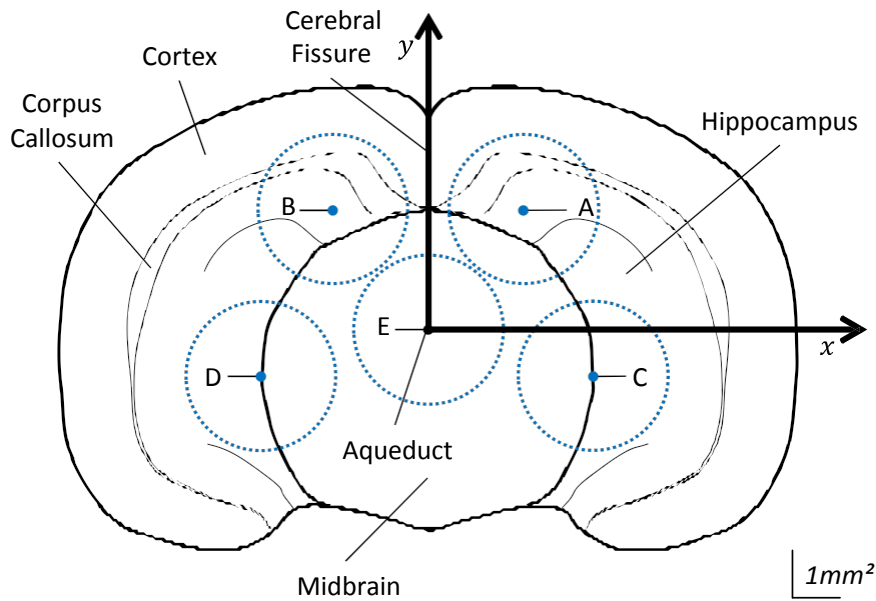


Figure 1: Schematic of a tissue sample showing the coordinate locations of the five un-normalized indentation regions A-E: A = (2, 2.5), B = (-2, 2.5), C = (3.5, -1), D = (-3.5, -1) and E = (0, 0). Dashed circles represent the cross-sectional area of the indenter overlaid onto the tissue sample.

Indentation Testing

The aluminum test stage with sample was mounted atop a 50gram load cell (Model 31 Low, Honeywell International Inc., Golden Valley, MN), and beneath a 3.18mm diameter plane-ended cylindrical indenter mounted to a linear actuator equipped with an LVDT to measure displacement (ElectroForce® 3100 Test Instrument, Bose Corporation – ElectroForce Systems Group, Eden Prairie, MN). Excess compliance in the test frame due to the motion of the actuator induced an inertial based force response in the load cell. A 500g linear accelerometer (Model#: 7264B-500, Humanetics Innovative Solutions, Plymouth, MI) was mounted to the test stage to subtract off this effect. Force, displacement, and acceleration data were acquired at 20kHz (DEWE-

2010, Dewetron Inc., Wakefield, RI). Regions were tested in a randomized order for each experiment. At each coordinate the indenter was centered on the Evan's Blue Dye. This was accomplished by mounting a 1.3mm diameter spherical tip punch to the actuator and positing directly over the dye via visual inspection. The spherical punch was exchanged with the plane-ended cylindrical indenter, which was assumed to be centered over the indentation coordinate. The indenter was advanced slowly toward the tissue at a rate of 0.01mm/s until a tare load of 0.3gram was achieved. The indenter tip was then pressed 0.6mm into the tissue, normal with respect to the local surface, in approximately 8ms and then held for 30s to measure the tissue's relaxation. A peak displacement velocity of 120mm/s, at an approximate strain rate of $17s^{-1}$, was observed during the ramp portion of the displacement. After each test the indenter was carefully removed from the tissue. Five minutes were allotted between tests to allow for tissue recovery and instrumentation adjustments [26]. The tissue was sprayed with Millonig's in between each indentation test. The protocol was repeated for the remaining four regions and all testing was completed within 75 minutes of animal sacrifice.

Mathematical Modeling

All data were filtered in accordance to the SAE-J211 standard, CFC 1000, using a zero-phase, digital IIR 8 pole butterworth filter at a Low Pass frequency of 1650Hz. The data were resampled in a logarithmically scaled time step to give equal weights to both ramp and hold portions of the test. Samples were assumed to be incompressible and isotropic [9], [10]. The force response, $\sigma(t)$, to the displacement input, $\delta(t)$, was modeled using a quasi-linear viscoelastic (QLV) mathematical framework [27]:

$$\sigma(t) = \int_0^t \dot{\delta}(\tau) \mathcal{R}(t-\tau) \mathcal{F}(\tau) d\tau \quad (1)$$

where $\mathcal{R}(t)$ is the instantaneous elastic response, $\mathcal{F}(t)$ is the reduced relaxation function, t is the time, and τ is a dummy variable over which the convolution integral (1) is evaluated. The instantaneous elastic response was modeled using the solution to the Boussinesq problem for a flat-ended cylindrical punch [28]:

$$\mathcal{R}(t) = \frac{4(1-\nu)}{1+\nu} \quad (2)$$

where a is the radius of the indenter, ν is Poisson's ratio, which was assumed to be 0.5, G is the shear modulus, and \mathcal{C} is a constant used to incorporate the effect of substrate on finite sample thickness [29]. Values of \mathcal{C} were obtained for each sample and found to be between 1.26 and 1.3. The shear modulus was chosen to be a second-order, even function of a to capture the spatial nonlinearity of the tissue [23]:

$$G = G_L + G_N \quad (3)$$

where G_L and G_N are the *instantaneous linear* and *nonlinear shear modulus coefficients*, respectively. Using this form for the shear modulus results in

$$\mathcal{R}(t) = \mathcal{C} \quad (4)$$

where \mathcal{C}_L and \mathcal{C}_N are the *linear* and *nonlinear coefficients* of $\mathcal{R}(t)$, respectively, described in (2). The mathematical solutions for the values of G_L and G_N in terms of \mathcal{C}_L and \mathcal{C}_N are determined through the use of equations (2-4).

$$G_L = \frac{1+\nu}{4(1-\nu)} \mathcal{C}_L \quad G_N = \frac{1+\nu}{4(1-\nu)} \mathcal{C}_N \quad (5)$$

A six term prony series with five time constants was chosen to model the relaxation behavior of the tissue:

$$\mathcal{F}(t) = \sum_{i=1}^6 \frac{\tau_i}{\tau_i + t} \quad \text{under the constraint that} \quad \sum_{i=1}^6 \tau_i = 1 \quad (6)$$

where α_i 's are the normalized relaxation coefficients of the corresponding time decades and α_{∞} is the coefficient of the steady-state response. Values for the thirteen coefficients $\alpha_0, \alpha_1, \alpha_2, \alpha_3, \alpha_4, \alpha_5, \alpha_6, \alpha_7, \alpha_8, \alpha_9, \alpha_{10}, \alpha_{11}, \alpha_{12}$, for $\tau = 1$ to 5 and α_{∞} were determined through a reduced gradient algorithm (Excel Solver®, Microsoft®, Redmond, WA) that was used to minimize the sum squared error between the model-predicted force, resulting from numerical integration of (1), and the experimental data. An individual set of optimal coefficients was determined for each indentation test. Preliminary analysis of the model fit to the first few data sets; test ID NIB00288A through NIB00288E, indicated marginal variability in the values for the optimized time constants, $\tau_0 \approx 0.001s$, $\tau_1 \approx 0.01s$, $\tau_2 \approx 0.1s$, $\tau_3 \approx 1s$, $\tau_4 \approx 10s$. To simplify the model the time constants were fixed at these decades for the remainder of the analysis and only eight parameters needed to be optimized through model fitting.

Statistics

The number of terms, n , in equation (6) were determined via an F-test [30]. Data from test ID NIB00318E was modeled with four, five, and six time constants to see if there was a statistically significant improvement in the model's fit to the data. The model with five time constants gave a significantly better fit ($F \approx 9$, $p < 0.001$) than the model with four time constants and the model with six time constants showed no improvement in fit over five time constants ($F \approx 0$, $p \approx 1$). Therefore the model with five time constants was chosen for the analysis. The critical F-statistic at the $\alpha = 0.05$ level of significance for both tests was $F_c \approx 1$. A total of $n = 8$ indentation tests were performed per region, A-E, and per injury treatment, Sham and severe injury, for a total of 10 groups. For each group, an average α_i and α_{∞} were determined using least squares optimization between the average and the eight individual measurements. The coefficients of the shear modulus, α_0 and α_1 were calculated from α_0 and α_1 of the eight individual curves using expression (5). An average α_0 and α_1 were then determined for

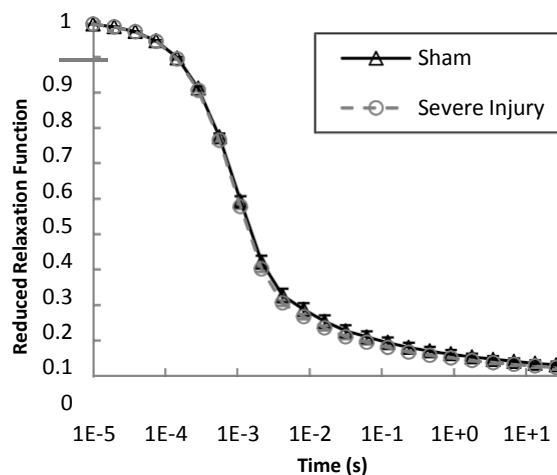
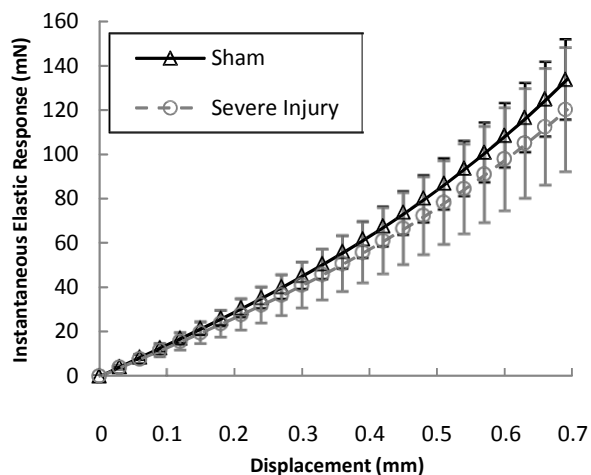
each group. Additionally, the coefficients of α_i and α_{∞} at regions A and C were normalized to the values

at the contralateral regions B and D, respectively. Specifically, normalization was performed by dividing the value of a particular absolute coefficient $\alpha_0, \alpha_1, \alpha_2$ and α_3 at region A by its corresponding absolute contralateral value at region B. For example, α_0 from indentation test ID NIB00290A was divided by α_0 from indentation test ID NIB00290B, etc. The process was repeated for the coefficients at region C, dividing by the corresponding contralateral values at region D. The absolute structural and material properties ($\alpha_0, \alpha_1, \alpha_2, \alpha_3, \alpha_4$, for $\tau = 1..5$ and α_{∞}) were compared separately to evaluate for the effect of region and injury treatment using a two-way ANOVA. *Post-hoc* comparisons were made using a student's t-test with the appropriate Bonferroni correction. Samples were assumed to be independent measurements of a particular tissue property, normally distributed and homoscedastic. To evaluate the differences observed in the normalized ratios, student's t-tests with a Bonferroni correction were used to make comparisons across injury treatment at a particular region. Specifically, a direct comparison was made between the normalized ratios of Sham and severely injured tissue at region A to evaluate the effect of injury at the location of the contusion cavity.

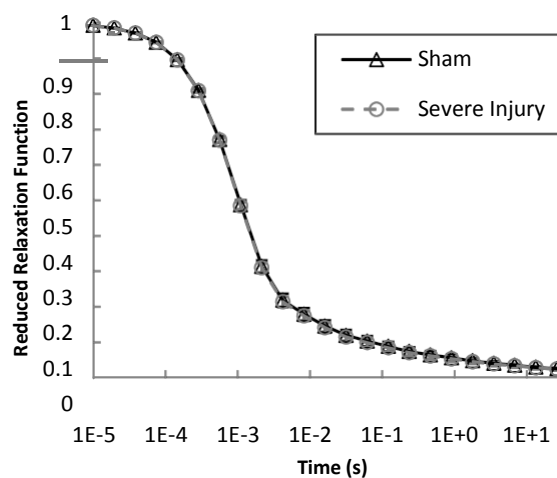
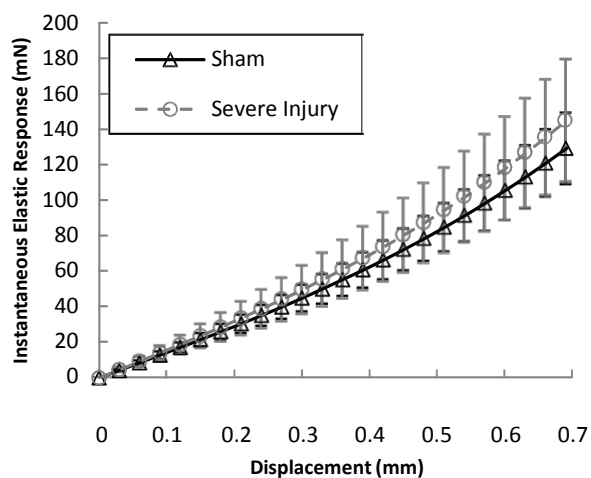
III. RESULTS

Eighty indentation tests were performed on the tissue samples, and data from 16 of the original 20 animals were used in analysis. The tissue from animal ID NIB00311 was damaged upon collection and the data from 3 additional experiments were compromised due to either unpreventable noise from the surroundings (animal ID NIB00287), or experimental error (animal IDs NIB00295 and NIB00298). Average α_i and α_{∞} for region and injury treatment are shown in Figure 2. Region specific, *absolute* structural and material properties, *normalized* ratios, and results of the t-tests are reported in Table 1 (see appendix). ANOVA indicated significant ($p < 0.05$) main effects of both region and injury treatment on the absolute coefficients. On average, α_0 and α_1 were higher ($p < \alpha = 0.005$) in region E compared to region A (α_0 : +36.3mN/mm, $p = 0.002$ and α_1 : +2.23kPa, $p = 0.002$). The relaxation coefficient, α_2 , was found to be higher while α_3 and α_{∞} were lower ($p < \alpha = 0.05$) in severely injured samples compared to Sham controls (α_2 : +0.011, $p = 0.0164$, α_3 : -0.003, $p = 0.008$, and α_{∞} : -0.003, $p = 0.044$). The student's t-test, revealed a significant decrease ($p < \alpha = 0.025$) in the value of the normalized ratios of α_0 and α_1 , (-26%, $p = 0.0084$ each), in severely injured tissue compared to Sham controls. Conversely, the t-tests revealed a significant increase in the normalized ratios of α_2 and α_3 , (+38%, $p = 0.0156$ each) on severely injured compared to sham controls in region C. The percentages reported here are calculated as percent differences in the sample means from Sham samples.

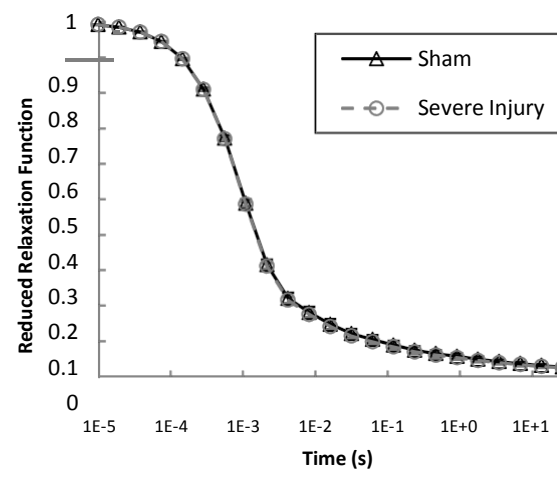
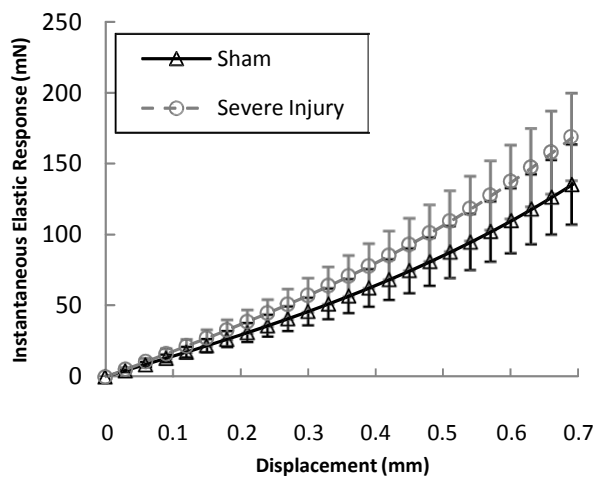
(Region A)



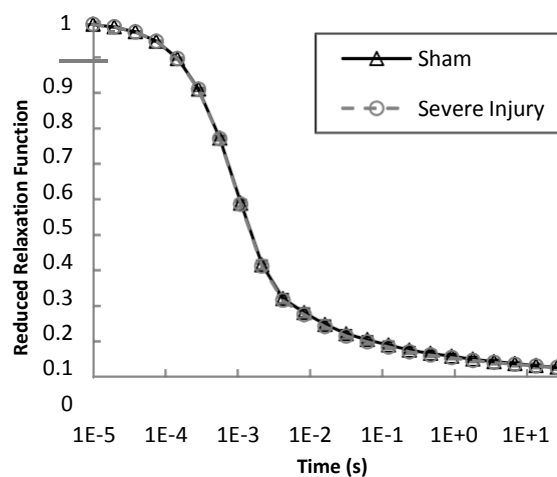
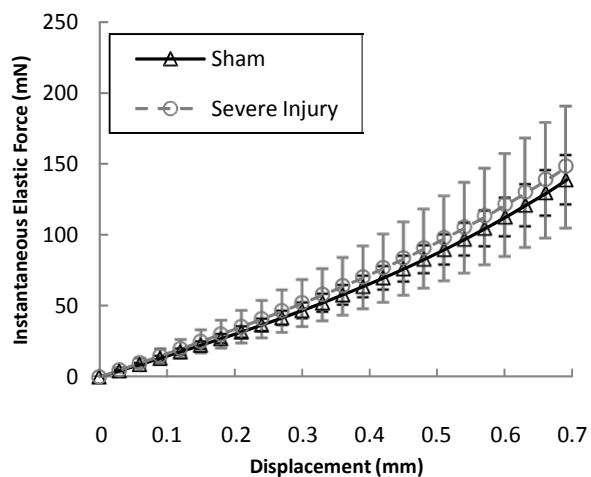
(Region B)



(Region C)



(Region D)



(Region E)

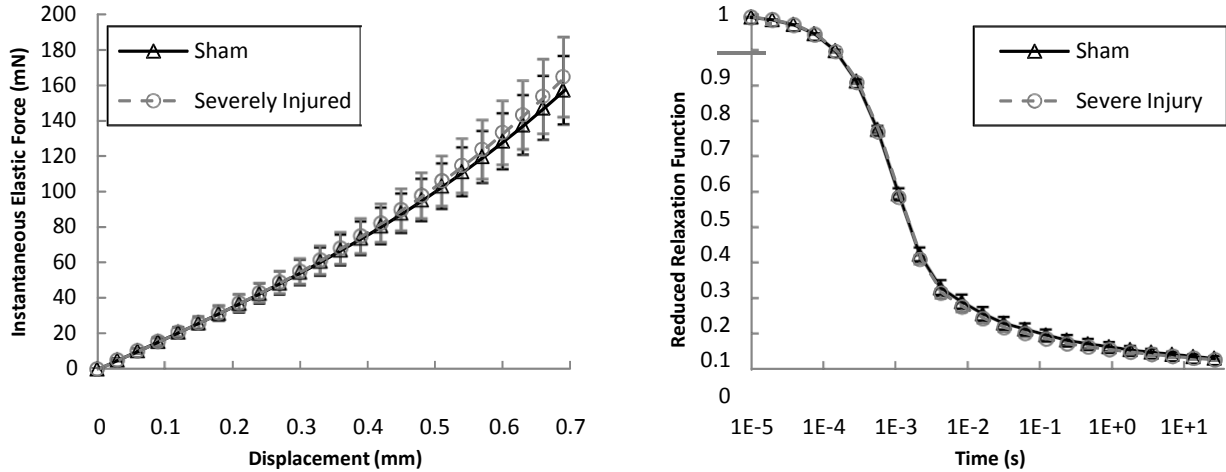


Figure 2: Average σ_{ij} and ϵ_{ij} for region and injury treatment. Error bars are 95% Confidence Intervals. Average σ_{ij} curves for severe injury were on average stiffer than the average Sham curves in all regions except for region A. The reduced relaxation functions were nearly identical in all cases.

IV. DISCUSSION

This study found the mechanical properties of the rat brain to be viscoelastic, spatially nonlinear, and dependent on both region and injury treatment. A linear viscoelastic model was fit to the experimental data, in addition to the QLV model, where equation (3) was assumed to be a function of ϵ_{ij} only. With the same number of prony series terms, the fits of both the linear and QLV models were visually assessed using tissue force time histories, and compared statistically using the F-test, Figure 3. The linear model fit the data well during the first half of the ramp and long term relaxation of the tissue; however, the addition of the nonlinear term through QLV showed a statistically significant improvement in the model fit ($p < 0.001$) to the experimental data, capturing the entire ramp, peak force, and initial tissue relaxation, Figure 3a. To justify the use of QLV over a fully nonlinear viscoelastic model the ratio of the relaxation forces from two different displacement steps were calculated and then checked to be approximately constant in time using linear regression. Two displacement steps, the first to 0.6mm and the second to 1.2mm, were applied to tissue from a severely injured animal; ID NIB00291 at region A and region E. Results from the linear regression were used to evaluate whether or not the slope of the force ratio was statistically significant from zero. Data up to 100ms after the peak force were not included in the analysis due to transience of the displacement ramp. The value of the regression coefficient, the slope, was found to be statistically significant (slope = $0.035s^{-1}$, $p < 0.001$) at region A and (slope = $0.007s^{-1}$, $p < 0.001$) at region E. However, the magnitude of the slope was not thought to be meaningful. That is, the ability to detect small changes in the value of the slope was due to the large amount of data being used, and that the resulting values were not influential, suggesting a relatively constant response over time. These results indicated that the relaxation behavior of the tissue was independent of displacement and that no temporal nonlinearities were observed up to approximately 18% sample penetration.

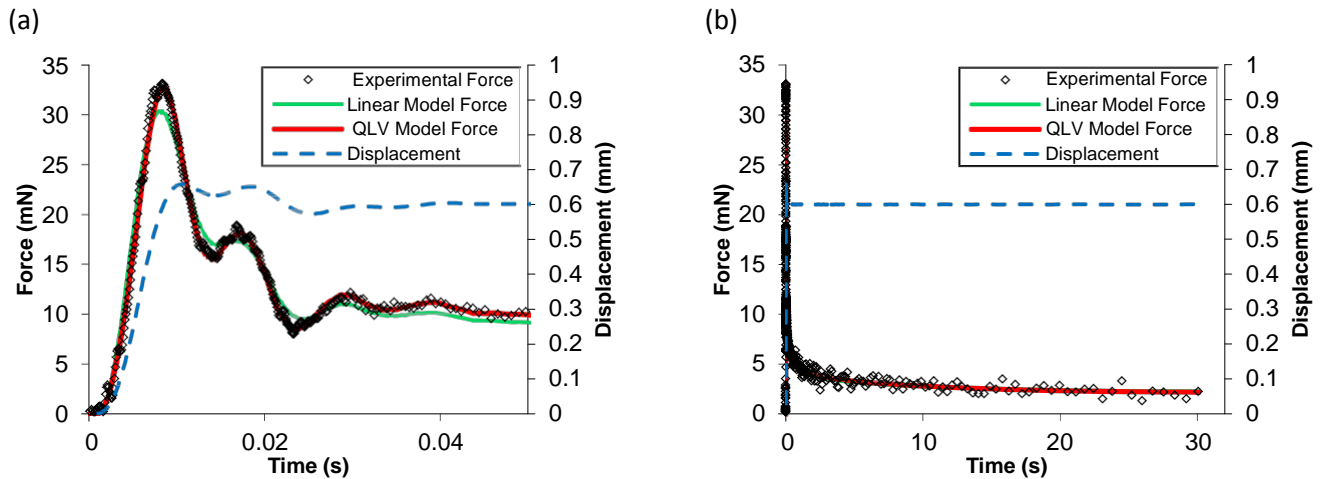


Figure 3: Examples of the QLV model fit to the experimental data for both the ramp (a) and hold (b) portions of an arbitrarily chosen indentation test (NIB00308B). The QLV model followed the experimental data more closely than the linear model during the ramp, peak, and initial relaxation of the tissue (a). Both models followed the data closely during the hold portion of the test (b). A similar result was observed when modeling other experimental data. The increase in force near 16ms and 30ms is due to the increase in displacement of the indenter into the tissue at these times.

Validation of the test methodology selected for the current study involves a comparison to other brain studies reported in the literature. The absolute mechanical properties and uncertainties found in the current study are consistent with those determined experimentally for shear [9], [31], compression [32] and indentation [23]. Further, the data fit within the reported range of shear moduli for brain tissue (0.1-22) kPa [8]-[16], [23] and [32]-[34]. Darvish and Crandall characterized bovine brain using QLV under oscillatory shear tests up to 200Hz and 20% Lagrangian strain [9]. They observed 16kPa and 2.62kPa for the linear and nonlinear instantaneous elastic shear moduli, respectively. On the other hand, Takhounts et al. tested both bovine and human brain up to 100% Lagrangian shear strain in ramp and hold tests and determined the instantaneous linear shear moduli to be approximately 2kPa and 1.5kPa, respectively [10]. Shuck and Advani found large variability in the shear modulus [31]. They performed oscillatory torsion tests on human brain up to 60Hz and observed (3-16)kPa. In each of these studies the brain was modeled under the assumptions of isotropy and incompressibility.

In regards to the results reported for indentation studies, Gefen et al. tested both young and mature rats in vivo and in situ under spherical indentation, and determined values for the instantaneous shear modulus between (1.2-3.3)kPa [15]. Further, Gefen and Margulies [33] compared the effects of in vitro, to in vivo and in situ on the material properties of porcine brain. They used a hemispherical indenter and found the short term shear modulus between (0.7-2.8)kPa. In both studies preconditioning was found to significantly reduce the value of the shear modulus and in vitro results tended to be lower than in vivo and in situ. Samples were not preconditioned in the current study as work by Shafieian et al. [23] suggests preconditioning may have damaged their samples and reduced the effect of injury. Various other studies have used micro-indentation to determine region specific material properties in rat brain [13], [34]. These studies observed values for the short term shear modulus on the order of (0.1-1.5)kPa, nearly one order of magnitude lower than the values reported in the current study. The material properties of brain have shown to be rate sensitive and increase with increasing strain rate or frequency [9] [10]. The load rates reported in these studies were less than 1mm/s, $(0.4-0.5)s^{-1}$, and much less than that of the current study which could explain this discrepancy. Additionally, these studies performed indentation tests up to depths of 40 μ m on the surface of tissue cross sections that had previously been blocked and then mechanically cut using a vibratome. Consequently, their findings may have been significantly altered from that of normal, healthy tissue. The tissue samples tested in the current study were hand cut and tested in vitro. As a result of sample preparation, a thin layer on the surface of the tissue likely sustained damage. Even though the indentation depths used in the current study were much higher than those used in micro-indentation, it is reasonable to expect some alterations in the mechanical properties from that of normal, healthy, living tissue.

In a similar study to the current, Shafieian et al. performed cylindrical indentation at two locations, PDx and PmJ, on the brainstem of impacted rats and found a statistically significant reduction in E_{avg} between uninjured and injured specimens [23]. They reported values for E_{avg} and E_{sec} between (1-10)kPa and (1-25)kPa/mm², respectively with similar uncertainties to that of the current study. The reported reduction in E_{avg} between injured specimens and Sham controls was 35%. This value was an average taken from both preconditioned and un-preconditioned samples and found to be in agreement with the work of Darvish and Crandall [12] who reported a 33% reduction in the linear shear modulus after non-recoverable strain conditioning. However, Shafieian et al. did not specify the significance of change in E_{avg} and E_{sec} with respect to injury treatment, making it unclear which parameter, if any, was driving the reduction in shear modulus after tissue damage [23]. On average, they saw a 28% and 47% reduction in E_{avg} and E_{sec} , respectively, for un-preconditioned samples at PDx. Further, they observed a 14% and 29% reduction in E_{avg} and E_{sec} for un-preconditioned samples at PmJ; however, this result was not statistically significant. In the current study E_{avg} and E_{sec} were reduced on average 17% and 26%, respectively at the location of the contusion cavity, region A. This was observed after normalizing the data and the reduction in E_{avg} was not statistically significant. In the case of

the absolute material properties, the observed differences in E_0 and E_{∞} between severely injured and Sham samples were not significant. Additionally, the reported 38% increase in E_{∞} at region C on severely injured compared to sham tissue contradicts the findings for the normalized properties at region A. Further investigation into this matter is needed; however there was no evidence of mechanical damage in this region when compared to the visible damage of the contusion cavity in region A.

Possible reasons for these discrepancies can be attributed to a number of factors. In the current study, a CCI model was used to deliver injury directly to the cortex [35]. On the other hand, Shafieian et al. chose an impact acceleration model to generate DAI in the brainstem due to its predictable pattern of injury there [23], [36]. Further, regions tested in the current study incorporate both white and grey matter and are heterogeneous compared to the brainstem which is comprised of predominantly white matter and is relatively homogenous and stiffer than the cortex [37]. Another explanation for these discrepancies is the rate at which the tissue samples were loaded under indentation. Peak Loading rates determined from the tests conducted by Shafieian et al. [23] were between (16-33)mm/s, (8-16)s⁻¹, while that of the current study was approximately 120mm/s, 17s⁻¹. High rate inputs are necessary to characterize the mechanical response of the brain during TBI [38]. The peak loading rates reported in the current study are within the range of those reported for impact traumas [13], [38], and [39]. An understanding of the brain's mechanical response at high load rates would be useful for computational models of these events. However, testing at these rates may cause further damage to the tissue and reduce the effect of injury on the mechanical properties. Strain and strain rate tissue tolerance thresholds have previously been studied and the reported values associated with axonal injury are between 0.1-0.2 Lagrangian strain with strain rates greater than 10s⁻¹ [9], [19]-[22].

The hypothesis that the tissue samples were damaged upon loading was examined in a separate analysis. A QLV model with only 1 time constant $\tau_Q = 0.001s$ was fit to the ramp portion the experimental data (n=16) for region A. The form of $\sigma = E_0 \epsilon + E_{\infty} (\epsilon - \epsilon_0) e^{-\frac{\epsilon - \epsilon_0}{\tau_Q}}$ was kept the same as expression (4). The model was fit in three ways. The sum

squared error was minimized between the model and experimental forces from: (1) the toe region to the force corresponding to the peak loading rate; (2) the force corresponding to the peak loading rate up to the peak force; and (3) over the entire ramp from the toe region to the peak force. Average E_0 and E_{∞} were determined from the (n=16) individual fits. ANOVA revealed significant ($p < 0.05$) differences between the three model fits. Post-hoc Bonferroni comparisons were made between individual samples and revealed the following information. The value of E_0 was approximately constant across all three models, while the value of E_{∞} decreased by 34% ($p < 0.001$) after the peak displacement rate of 120mm/s. This observation was made independent of injury treatment. The stability of the model was evaluated during each of the three fits due to the relatively small amount of data being fitted. Regardless of initial inputs, model parameters optimized to the same values, indicating a stable solution. These results suggest that the tissue may have been damaged during loading up to 5% tissue penetration and at a peak rate of 17s⁻¹.

V. CONCLUSIONS

This study presents an experimental methodology and analytical framework for modeling the region specific structural and material properties of mechanically injured and uninjured brain tissue. Force data were acquired under high rate loading inputs in the range of those related to impact traumas. Quasi-linear viscoelasticity, a popular, constitutive model that is commonly used to model soft biological materials was chosen to fit the experimental data over both linear and fully nonlinear viscoelastic models. The tissue was assumed to be isotropic and incompressible for model simplification. The mechanical properties were found to be viscoelastic, nonlinear, and regionally dependent. Additionally, these properties were quantified under a well characterized injury model capable of delivering repeatable levels of mechanical damage directly to the dura. To the authors' knowledge, this is the first study to examine the mechanical properties of the brain after CCI. The results for the shear modulus were within the range reported in the literature for shear, compression, and indentation tests. The material and structural properties were found to be roughly constant across region and injury treatment. However, after normalizing the region specific mechanical properties in regions A and C, there were statistically significant differences in the values of the nonlinear coefficients of the instantaneous shear and elastic response. A 26% reduction in the nonlinear material and structural coefficients were observed in severely injured samples compared to healthy controls at the location of the contusion cavity. The utility of this research is crucial for understanding the mechanical response of the brain after TBI. Knowledge of such

material properties may be useful to uniquely identify different types of brain injury and to better understand the mechanics of repetitive brain injuries.

VI. LIMITATIONS

There are a number of limitations that may influence overall response of the tissue samples during mechanical loading. First, the solution to the Boussinesq problem assumes indentation of a semi-infinite elastic half-space. The samples used in the current study have finite boundaries and exhibit damping as well as elastic properties. This solution was modified by [29] to incorporate the effect of a rigid substrate on finite sample thickness. The corrective factor β was developed for indentation on articular cartilage and subsequently applied to indentation tests performed on other soft biological tissues including brain [13], [23]. The factor β functions to reduce the applied load, measured within the tissue, by an amount that depends on the ratio of the indenter radius to sample height. As the indenter radius increases or sample height decreases, higher forces are transmitted from the substrate to the tissue. To avoid the effect of substrate on mechanical properties, a common rule of thumb is to limit indenter penetration to depths of no greater than 10% of the total sample thickness [40]. Penetration depths in the current study obey this rule. However, more recent work has observed noticeable substrate effects within 10% penetration and claim that the ratio of the indenter radius to sample height must be kept within 10% [41]. The ratio of radius to sample height is 20% in the current study and β was implemented to adjust for this limitation. In addition to substrate effects, other boundary conditions have been violated. In all regions except E, the distance between the indenter and edge of the tissue sample was less than the recommended distance of one indenter's width. This would have the effect of reducing the material properties observed in regions A-D compared to E. Indenter interference is an additional concern in this study. The process by which the coordinates were dimensioned on the surface of the tissue was imperfect. Slight offsets in the dimensioning may have led to overlapping indentation tests. Further, the indentations made on the surface of the samples were within one diameter of each other. However, adequate time was allotted for tissue recovery in between subsequent tests. Finally, contusion cavities can be problematic for material studies [23]. They are often near the edge of the sample and create discontinuities in the tissue surface making it difficult to obey boundary conditions under most mechanical tests. It is suggested that future studies involving contusion cavities be made in vivo or situ with the brain left in the skull.

A number of studies including the current have used the F-test to statistically determine an appropriate model for fitting experimental brain data [13], [23], [34]; however, there are limitations. The F-test assumes the data to be independently measured and normally distributed. In addition, there must be a linear relationship between independent and dependent variables in the models chosen to fit the data. The force data in the current study are not normally distributed and not independent measurements in time. Further, in both the linear viscoelastic and QLV models the relationship between force and time is not linear. Therefore it is not clear that hypothesis testing using the F-test is suitable or meaningful to determine the most appropriate model. In this case, visual inspection of the model fit to the data may provide a better indicator of goodness of fit.

VII. ACKNOWLEDGEMENT

This work was performed at the University of Virginia, and in collaboration with the University of Washington. Funded in part by the Defense Medical Research and Development Program (DMRDP), award No. DM090796.

VIII. REFERENCES

- [1] Faul M, Xu L, Wald MM, Coronado VG, "Traumatic brain injury in the United States: emergency department visits, hospitalizations, and deaths, Atlanta (GA): Centers for Disease Control and Prevention, National Center for Injury Prevention and Control, 2010", Internet: [\[http://www.cdc.gov/traumaticbraininjury/tbi_ed.html\]](http://www.cdc.gov/traumaticbraininjury/tbi_ed.html), January 7, 2013, [February 21, 2013]
- [2] Owens BD, Kragh JF Jr, Wenke JC, Macaitis J, Wade CE, Holcomb JB, Combat wounds in Operation Iraqi Freedom and Operation Enduring Freedom, *Journal of Trauma-Injury Infection & Critical Care*, 64(2):295-299, 2008.
- [3] Pascrell B Jr, Congressman, Introduction to the report of the international conference on behavioral health and traumatic brain injury, *The Clinical Neuropsychologist*, 23(8):1281-1290, 2009.

- [4] Farkas O, Povlishock JT, Cellular and subcellular change evoked by diffuse traumatic brain injury: a complex web of change extending far beyond focal damage, *Progress in Brain Research* 161:43-58, 2007.
- [5] McAllister TW, Neurobiological consequences of traumatic brain injury, *Dialogues in Clinical Neuroscience*, 13(3):287-300, 2011.
- [6] Povlishock JT, Katz DI, Update of neuropathology and neurological recovery after traumatic brain injury, *The Journal of Head Trauma Rehabilitation* 20(1):76-94, 2005.
- [7] Holbourn AHS, Mechanics of head injury, *The Lancet*, 2, 6267, 438-441, 1943.
- [8] Galford JE, McElhaney JH, A viscoelastic study of scalp, brain, and dura, *Journal of Biomechanics*, 3(2):211-221, 1970.
- [9] Darvish K, Crandall JR, Nonlinear viscoelastic effects in oscillatory shear deformation of brain tissue, *Medical Engineering & Physics*, 23:633-645, 2001.
- [10] Takhounts EG, Crandall JR, Darvish KK, On the importance of nonlinearity of brain tissue under large deformations, *Stapp Car Crash Journal*, 47:79-92, 2003.
- [11] Gefen A et al., Age-dependent changes in the material properties of the brain and braincase of the rat, *Journal of Neurotrauma*, 20(11):1163-1177, 2003.
- [12] Prange MT, Margulies SS, Regional, directional, and age-dependent properties of the brain undergoing large deformation, *Journal of Biomechanical Engineering*, 124:244-252, 2002.
- [13] Finan JD, Pearson EM, Morrison III B, Viscoelastic properties of the rat brain in the horizontal plane, *Proceedings of IRCOBI Conference*, Dublin, Ireland, pp. 474-485, 2012.
- [14] Thibault KL, Margulies SS, Age-dependent material properties of the porcine cerebrum: effect on pediatric inertial head injury criteria, *Journal of Biomechanics* 31(12):1119-1126, 1998.
- [15] McElhaney JH, Roberts VL, Hilyard JF, Handbook of Human Tolerance, Japan Automobile Research Institute, Incorporated (JARI), p. 143, 1976.
- [16] Arbogast KB et al., A high-frequency shear device for testing soft biological tissues, *Journal of Biomechanics*, 30(7):757-759, 1997.
- [17] Dobbing J, The later development of the brain and its vulnerability. In: Davis J A, Dobbing J (Eds.), Scientific Foundations of Paediatrics, *Heinemann Medical*, London, UK, 1974.
- [18] Mao H, Jin X, Zhang L, Yang KH, Igarashi T, Noble-Haeusslein LJ, et al., Finite element analysis of controlled cortical impact-induced cell loss, *Journal of Neurotrauma*, 27(5):877-88, 2010.
- [19] Elkin BS, Morrison B III, Region-specific tolerance criteria for the living brain, *Stapp Car Crash Journal*, 51: 127-138, 2007.
- [20] Cater HL, Sundstrom LE, and Morrison B, Temporal development of hippocampal cell death is dependent on tissue strain but not strain rate, *Journal of Biomechanics* 39(15):2810-2818, 2006.
- [21] Morrison III B, Cater HL, Wang CC, Thomas FC, Hung CT, Ateshian GA, et al., A tissue level tolerance criterion for living brain developed with an in vitro model of traumatic mechanical loading, *Stapp Car Crash Journal*, 47:93-105, 2003.
- [22] Bain AC, Meaney DF, Tissue-level thresholds for axonal damage in an experimental model of central nervous system white matter injury, *Journal of Biomechanical Engineering*, 122:615-622, 2000.
- [23] Shafieian M, Darvish KK, and Stone JR, Changes to the viscoelastic properties of brain tissue after traumatic axonal injury, *Journal of Biomechanics*, 42(13):2136-2142, 2009.
- [24] Saxena T, et al., Mechanical characterization of the injured spinal cord after lateral spinal hemisection injury in the rat, *Journal of Neurotrauma*, 29(9):1747-1757, 2012.
- [25] Paxinos G, Watson C, The Rat Brain in Stereotaxic Coordinates 5th Edition, Bregma -5.04 mm, *Elsevier*, Oxford, UK, 2005.
- [26] Hrapko M et al., The mechanical behavior of the brain tissue: Large strain response and constitutive modeling, *Biorheology*, 43:623-636, 2006.
- [27] Fung YC, Biomechanics: Mechanical Properties of Living Tissues, 277-280, *Springer*, New York, NY, 1993.
- [28] Sneddon IN, The relation between load and penetration in the axisymmetric Boussinesq problem for a punch of arbitrary profile, *International Journal of Engineering Science* 3(1):47-57, 1965.
- [29] Hayes WC, Keer LM, Herrmann G, and Mockros LF, A mathematical analysis for indentation tests of articular cartilage, *Journal of Biomechanics*, 5(5):541-551, 1972.

- [30]Motulsky HJ, Cristopoulos A, Fitting Models to Biological Data using Linear and Nonlinear Regression. A Practical Guide to Curve Fitting. 2003, GraphPad Software Inc., San Diego CA, www.graphpad.com.
- [31]Shuck LZ, and Advani SH, Rheological response of human brain tissue in shear, *Journal of Basic Engineering*, 94 (D), 905-911, 1972.
- [32]Estes MS and McElhaney JH, Response of the brain tissue of compressive loading. ASME, No 70-BHF-13, 1970.
- [33]Gefen A, Margulies SS, Are in vivo and in situ brain tissues mechanically similar? *Journal of Biomechanics*, 37:1339-1352, 2004.
- [34]Elkin BS, Ilankovan A, and Morrison III B, A detailed viscoelastic characterization of the rat brain, *Journal of Neurotrauma* 28:2235-2244, 2011.
- [35]Lighthall JW, Controlled cortical impact: a new experimental brain injury model, *Journal of Neurotrauma*, 5(1):1-15, 1988.
- [36]Marmarou A et al., A new model of diffuse brain injury in rats, *Journal of Neurosurgery* 80:291-300, 1994.
- [37]Arbogast K, Margulies S, Material characterization of the brainstem from oscillatory shear tests, *Journal of Biomechanics* 31(9):801–807, 1998.
- [38]Mertz HJ, Anthropomorphic test devices, In: Nahum, A.M., Melvin, J.W. (Eds.), *Accidental Injuries*. Springer, New York, pp. 72–88, 2002.
- [39]Hardy WN et al., A study of the response of the human cadaver head to impact, *Stapp Car Crash Journal* 51:17, 2007.
- [40]Bückle H, Progress in micro-indentation hardness testing, *Metallurgical Reviews*, 4(1):49-100, 1959.
- [41]Wang M et al., Nanoindentation of polymeric thin films with an interfacial force microscope, *Journal of the Mechanics and Physics of Solids*, 52:2329-2354, 2004.

IX. APPENDIX

Table 1: Absolute Structural and Material Coefficients of σ_{xx} , σ_{yy} , and σ_{zz} and Normalized Ratios for Region and Injury Treatment.

Absolute		A						B						C					
Unit	Coef.	Sham			Severe Injury			Sham			Severe Injury			Sham			Severe Injury		
mN/mm	F ₁	140.8	±	19.2	128.2	±	33.0	141.1	±	24.1	155.2	±	44.7	143.4	±	30.7	179.0	±	38.7
mN/mm ³	F ₃	111.6	±	24.1	96.6	±	19.7	97.3	±	17.4	115.6	±	22.3	110.8	±	23.6	138.1	±	16.4
kPa	μ _o	8.66	±	1.23	7.89	±	2.04	8.68	±	1.51	9.55	±	2.76	8.85	±	2.00	11.02	±	2.40
kPa/mm ²	μ ₂	6.88	±	1.57	5.95	±	1.23	5.99	±	1.12	7.11	±	1.38	6.83	±	1.53	8.50	±	1.03
-	G ₁	0.739	±	0.021	0.763	±	0.010	0.749	±	0.021	0.752	±	0.015	0.746	±	0.018	0.750	±	0.010
-	G ₂	0.122	±	0.007	0.117	±	0.007	0.121	±	0.006	0.123	±	0.004	0.122	±	0.006	0.126	±	0.004
-	G ₃	0.057	±	0.005	0.053	±	0.004	0.055	±	0.002	0.053	±	0.006	0.057	±	0.003	0.054	±	0.003
-	G ₄	0.029	±	0.005	0.026	±	0.002	0.029	±	0.008	0.028	±	0.003	0.027	±	0.005	0.027	±	0.002
-	G ₅	0.023	±	0.007	0.020	±	0.005	0.023	±	0.008	0.022	±	0.006	0.023	±	0.004	0.021	±	0.002
-	G _∞	0.029	±	0.009	0.022	±	0.005	0.024	±	0.003	0.022	±	0.003	0.025	±	0.004	0.023	±	0.004
	Absolute		D						E										
	Unit	Coef.	Sham			Severe Injury			Sham			Severe Injury							
	mN/mm	F ₁	145.7	±	18.4	163.6	±	54.1	170.8	±	24.0	170.7	±	21.8					
	mN/r m ³	F ₃	116.2	±	33.5	106.0	±	20.6	120.2	±	32.3	142.8	±	24.5					
	kPa	μ _o	8.96	±	1.15	10.07	±	3.35	10.49	±	1.42	10.51	±	1.39					
	kPa/r m ²	μ ₂	7.17	±	2.15	6.52	±	1.28	7.42	±	2.07	8.79	±	1.54					
	-	G ₁	0.746	±	0.015	0.750	±	0.009	0.737	±	0.024	0.756	±	0.015					
	-	G ₂	0.122	±	0.006	0.125	±	0.003	0.122	±	0.007	0.118	±	0.004					
	-	G ₃	0.055	±	0.004	0.054	±	0.003	0.059	±	0.004	0.056	±	0.004					
	-	G ₄	0.028	±	0.004	0.026	±	0.002	0.029	±	0.005	0.024	±	0.004					
	-	G ₅	0.024	±	0.007	0.020	±	0.004	0.025	±	0.010	0.023	±	0.005					
	-	G _∞	0.025	±	0.005	0.025	±	0.006	0.028	±	0.006	0.024	±	0.002					
Normalized Ratios		A						C											
Unit	Coef.	Sham			Severe Injury			Sham			Severe Injury								
-	F ₁	1.017	±	0.144	0.843	±	0.145	0.999	±	0.228	1.187	±	0.357						
-	F ₃	1.149	±	0.182	*	0.848	±	0.144	0.992	±	0.158	†	1.361 ± 0.275						
-	μ _o	1.017	±	0.144	0.843	±	0.145	0.999	±	0.228	1.188	±	0.357						
-	μ ₂	1.149	±	0.182	**	0.848	±	0.144	0.992	±	0.158	††	1.362 ± 0.276						

All symbols indicate a statistically significant result. Asterisks (*,**) and daggers (†,††) are comparisons between injury treatment at a particular region. (p = resulting p-value from a student's t-test and $\alpha = 0.025$ is the Bonferroni corrected significance level). (*p = 0.0084, **p = 0.0085, †p = 0.0156, ††p = 0.0156. All uncertainties are ±95%CI.

Transcranial vibro-acoustography can detect traumatic brain injury, in vivo

Martin W. Suarez¹, David D. Dever¹, Xiaohan Gu¹, P. Ray Illian², B.S., Caren Marzban Ph.D.

(Department of Statistics and APL), Edin Mehic¹, Pierre D. Mourad, Ph.D.^{1,2,3}

¹Department of Bioengineering, Univ. of WA; ²Applied Physics Laboratory, Univ. of WA;

³Department of Neurological Surgery, Univ. of WA

Corresponding Author:

Pierre D. Mourad

Department of Neurological Surgery

University of Washington

Box 356470

Seattle WA 98195-6470

(email) pierre@apl.washington.edu

For submission to Ultrasound in medicine and biology

BEFORE SUBMISSION RE-CHECK CITATIONS. ORDER IS MESSED UP.

terminology: acoustic emissions —> raw signal

Vibro-acoustic emissions —> binned data (unnormalized)

binning is important because it identifies noise from actual signal

Abstract

Vibro-Acoustography (Vibro) is an ultrasound modality that has proven to be effective in imaging and characterizing tissue structures based on their elastic properties. While Vibro has been implemented within a variety of tissue systems for diagnostic and therapeutic effects, applications to brain tissue remain nascent. Here we investigate the ability of Vibro to detect traumatic brain injury (TBI) *in-vivo* via the application of focused Vibro-acoustic emissions with difference frequencies between 200-270 kHz. Findings from Vibro applied to rats (sham N=6; acute TBI N=6) indicate that normalized acoustic emissions, captured near the site of TBI, are lower in magnitude for TBI animals at specific difference frequencies. This ability of Vibro to sense the acute changes in brain tissue caused by injury opens the possibility for new TBI detection methods based upon a Vibro-acoustic ultrasound platform.

Keywords:

Animal Models, Traumatic Brain Injury; Vibro-acoustography, Rat, Applied Radiation Force

Introduction

Traumatic brain injury (TBI) is a leading cause of death and disability, accounting for 30.5% of all injury related deaths within the U.S. alone (Faul et al. 2010). However, while TBI remains a serious concern in domestic settings, the dangers of TBI are severely pronounced within combat zones, with over 250,000 cases of TBI reported by the military between 2002 - 2012 (Fischer 2013). The true number of soldiers sustaining TBI is believed to be much higher. Military field tests report missing 40% of all TBI cases due to high levels of diagnostic subjectivity and patient variability (Miller et al. 2010). While current diagnostic tools such as computed tomography (CT) and magnetic resonance imaging (MRI) are capable of identifying TBI, their logistics make them ineffective diagnostic tools in the field, where rapid triage can significantly improve clinical outcomes. Here we investigate the possible use of Vibro-Acoustography (Vibro) as a basis for a portable TBI-detection device.

Vibro utilizes confocal transducers to converge two ultrasound beams of different carrier frequency to a single focus, spatially, and generate vibrations within a tissue as a result of the applied radiation force. These tissue vibrations will have a frequency equal to the difference between the two carrier frequencies. This emitted difference frequency, acoustic emission, can be captured and used to quantify the mechanical response of the tissue to the applied radiation force (Fatemi and Greenleaf 1998; Urban et al. 2011). Because trauma can alter the mechanical properties of tissue (Greenwald 2003; Boulet et al, 2011 and 2013), Vibro induced vibrations in damaged tissue will generate different acoustic emissions compared to normal tissue. In essence, Vibro exploits the differences in the mechanical properties between tissues to identify and differentiate between normal and abnormal tissue systems. Vibro has previously been implemented to distinguish between normal and calcified femoral arteries *in-vivo* (Pislaru et al. 2008), detecting calcifications within the prostate (Urban et al. 2011), and the detection of breast

lesions in humans (Alizad et al. 2012). Vibro has also been used to image lesions in the liver and to track brachytherapy seeds used in the treatment of prostate cancer (Urban et al. 2011).

Here we test the hypothesis that acoustic emissions generated by transcranially delivered Vibro are sensitive enough to detect the presence of TBI in rat brains with focal trauma generated by a controlled cortical impact (CCI).

MATERIALS AND METHODS

Transducer description

A dual-element 2 MHz focused ultrasound transducer (Figure 1)(Sonic Concepts, Model H-148, Woodinville WA) was used to generate the acoustic radiation force needed to generate tissue vibrations. This transducer has a radius of curvature of 63.2 mm, placing the center of the focus 51.74 mm from the exit plane. The inner element has an inner diameter of 22.6 mm and outer diameter of 48.29 mm. The outer element has an inner diameter of 49.05 mm and outer diameter of 64.0 mm. Linear simulations of both elements operating in unison (Figure 2) predict a focus that measures 8 mm axially and 1 mm radially as measured at the pressure half-maximum value.

Each transducer element was driven independently but in a synchronized fashion by a pair of function generators (33220A 20MHz Function/Arbitrary Waveform Generator, Agilent, Santa Clara, CA) through separate amplifiers (Model A150 RF Power Amplifiers, E&I, Rochester, NY). Driving signals were configured through the use of associated pressure outputs, as measured in degassed water with a needle hydrophone (HNR-100 S/N 1370, ONDA, Sunnyvale, CA), to ensure that each transducer element contributed an equal pressure to the mutual focus for each of the difference frequencies considered: 200-270 kHz, inclusive, in steps of 10 kHz. These selected difference frequencies lay within 10-13.5% of the transducers 2 MHz center frequency and are within the efficiency band of the transducer. The net pressure generated by both transducer elements at a given difference frequency was used to determine that the generated spatial-peak-temporal-average (SPTA) intensity ranged from 0.1 - 0.7 W/cm².

■
During experiments dFU within this intensity range was applied, at a given difference frequency, for 1000 μ s. Acoustic emissions from the tissue were recorded for 1200 μ s.

TBI induction.

All animal procedures were approved by the Institutional Animal Care and Use Committee (IACUC) of the University of Washington, Seattle, WA. Male Sprague Dawley® rats (Charles River, Wilmington, MA), weighing between 351 ± 80 g, were split into two experimental groups: a sham control group (N=6) and an acute TBI group (N=6). Three additional sham rats were used to determine the signal-to-noise ratios for various intensities of applied ultrasound.

(Three more rats were used to determine the difference between signals captured in rats with skull and those without.)

Animals were anesthetized with isoflurane (5% for induction and 1.5 - 3% for maintenance, with an oxygen flow rate of 1.5 L/min) then placed on a stereotactic surgical platform with metal bars that were fixed in the rats' ear canals to stabilize their heads for surgery, injury induction, and data collection. The head was then shaved and the remaining hair removed with Nair® (Church & Dwight Co, INC., Princeton, NJ, USA). Following epilation, subcutaneous lidocaine (0.08 mL, 20 mg/mL) and bupivacaine (0.08 mL, 0.32 mg/mL) were administered and spread across the surgical site by manual palpation. A heating pad was placed under the body to maintain a core body temperature near 37°C throughout the experiment.

An incision, along the sagittal plane, was then made from behind the ears to between the eyes. Following this, an area of skull approximately 1 cm in width was fully exposed by removal of the periosteum. A small bone drill was used to create a circular hole through the skull, at a location **3 mm anterior and 2 mm to the left of the lambda**, just exposing the surface of the brain. A rongeur was used to widen this cranial window radially to a diameter of approximately 3 mm, in order to accommodate the tip of a controlled cortical impact (CCI)

Martín Suárez 4/15/14 9:51 PM

Comment [1]:
add this in ...doesn't just using the word
additional accomplish this meaning? -LK

device (AMS 201, AmScien Instruments, Richmond, VA, USA). This marked the end of surgery for the sham group.

For each animal in the acute TBI group the tip of the CCI device was positioned directly over the cranial window and lowered to the surface of the brain. The device was then fired to induce a 2 mm deep impact into the brain (tip speed of 1.15 m/s), consistent with the protocol of Lighthall (1988) as refined by Dixon et al. (1991). This marked the end of surgery for the TBI group.

Application of diagnostic focused ultrasound (dFU)

All Vibro studies were conducted under anesthetic conditions. The face of the transducer was covered with a plastic coupling cone filled with degassed water for optimal ultrasound transmission to the brain (Figure 1). The front of this coupling cone was sealed with a sheet of acoustically translucent latex, the rear was closed with a focused polyvinylidene fluoride (PVDF) hydrophone (Harisonic® Y-107-7, Olympus Corporation, Tokyo, Japan). The focus of the hydrophone was selected such that it is confocal with the transducer. The hydrophone was then connected to an amplifier (Hydrophone Booster Amplifier, Precision Acoustics Ltd., Dorchester, Dorset, UK) and oscilloscope (LeCroy, Chestnut Ridge, NY, USA) to allow visualization of acoustic emissions from the brain. These acquired waveforms were then linked to a desk-top computer (Dell, Round Rock, TX, USA) for MATLAB-based (MathWorks, Natick, MA, USA) data processing.

The transducer and hydrophone were then mounted on a three-way micro-positioning system (Velmex, INC., East Bloomfield, NY, USA) to allow the ultrasound focus to be moved to any anatomical point of interest. A laser guidance system was implemented in order to identify the ultrasound focus during experiments. These lasers were affixed to the coupling cone such that their intersection marked the center of the transducers' focus. Utilizing the lasers, the transducer's position was adjusted via the micro-positioner such that the ultrasound focus

Martín Suárez 4/18/14 12:37 PM

Comment [2]:

All the company names here really ruin the flow of the paragraph, how can i alter this?

occurred 5 or 8 mm below the surface of the skull (as desired). The focus could then be moved to each of the two target locations in our study, relative to the site of injury, defined by their coronal position on the skull and the depth of dFU (Figure 3). Acoustic emissions from the brain across the range of predetermined difference frequencies (200 - 270 kHz, in steps of 10 kHz) were collected twice for each difference frequency. Collected waveforms were exported to MATLAB® for analysis. Within MATLAB the two waveforms from each difference frequency were then averaged to yield a final mean acoustic emissions signal. These final mean acoustic signals were collected three times for all difference frequencies and from each target location.

Immediately following data acquisition rats were euthanized with **390 mg/ml** Beuthanasia®-D via intraperitoneal injection.

Data analysis of acoustic emissions

Raw acoustic emissions from rat brain were captured via the PVDF hydrophone across a frequency range of 10 kHz - 15 MHz. During data analysis only emissions within the range of 10 kHz - 2.5 MHz were considered (Figure 4). Following acquisition, acoustic emissions were decomposed via Fast Fourier Transform (FFT) to examine their frequency components. Frequency bins centered at each difference frequency with a width of 7 kHz **where then created to consolidate portions of the acoustic emission to be considered Vibro-acoustic signal. Additional frequency bins centered half-way between each applied difference frequency with a width of 3 kHz were also created to consolidate background noise within the range of the applied difference frequencies. This narrow frequency range for noise was chosen so that it would not be skewed by the large spectral magnitudes found at the carrier frequencies. (frequency-frequency plot, Figure 5 —> reassign location of this picture.)**

Preliminary findings demonstrated that Vibro-acoustic signals from tissue varied significantly with the spectral magnitude at the carrier frequencies. Acoustic emissions also

varied with background noise in the range of our applied difference frequencies. To account for these affects two normalizations were developed:

$$N_1 = \frac{A^2}{C_1^2 + C_2^2} \quad N_2 = \frac{A^2}{\sqrt{C_1^2 + C_2^2} * RMS(\eta)}$$

A is the maximum spectral magnitude from within the frequency bin of an acoustic emission generated by a given applied difference frequency. C_1 and C_2 are the spectral magnitudes of the two carrier frequencies at this same difference frequency. η is a numerical set containing the root-mean-square (RMS) values determined for each of the 7 noise bins. Both N_1 and N_2 yield non-dimensional measures of Vibro-acoustic signal magnitude, whereas unnormalized signal was represented by the spectral voltage of the acquired signal for each applied difference frequency.

N_1 strictly seeks to compensate for fluctuations in the spectral magnitudes of the carrier frequencies. Because induced tissue vibrations are not expected in the range of the carrier frequencies changes in spectral magnitude at the carriers, captured by the hydrophone, may be attributed to an unexpected increase in ultrasonic intensity. Dividing acquired emissions by the carriers diminishes the influence of variation in the carriers on the signal generated by vibrating tissue. N_2 seeks to address fluctuations at the carriers as well as noise within the range of the applied difference frequencies. This noise may arise from variations in rat skull anatomy as well as from bubbles present within the ultrasound gel or the coupling cone. In these cases any captured emissions would be a sum of scatter from skull or bubbles as well as actual Vibro-acoustic signal. Dividing acquired emissions by noise and the carriers together allows a better representation of the signal generated by vibrating tissue alone.

Statistical Analysis

■ The magnitudes of Vibro-acoustic signals acquired from sham and TBI rats were compared via the Mann-Whitney U test (**Sigma Plot, Systat Software Inc., San Jose, CA, USA**), for each location and difference frequency. In all comparisons a p-value ≤ 0.05 was taken to denote statistical significance between the signals of TBI and sham rats.

Data analysis of signal-to-noise ratio (SNR)

Acoustic emissions from three sham rats were collected across a range of applied intensities: 0.4, 0.5, 0.6, and 0.72 W/cm² SPTA. This was done to determine if the application of transcranial Vibro could generate measurable Vibro-acoustic signals using intensity levels below the FDA limit of 0.72 W/cm² SPTA. For calculation of the SNR the signal component was taken to be the RMS value of the spectral magnitudes within the frequency bin of the applied difference frequency. The noise component was taken to be the RMS value of η (as previously defined).

Martín Suárez 4/18/14 4:01 PM

Comment [3]:
Pierre do we want to include this paragraph?

Martín Suárez 4/19/14 12:22 PM

Comment [4]:
the way signal is defined here is different than what we say signal is in the normalizations. —> why?does this matter?

RESULTS

Signal-To-Noise Ratio (SNR)

At an applied intensity of 0.4 W/cm² SPTA SNRs at the FR8 location were determined to fall between 3.2 ± 0.9 . SNRs from the FL8 location fell between 6.25 ± 2.0 .

Vibro-acoustic signals for sham versus TBI rats

Analysis of un-normalized Vibro-acoustic signals from sham versus TBI rats indicated that statistically significant differences were present at several locations and applied difference frequencies (Table 1), especially at the FL5 and FL8 locations (see Figure BLAH for an example of these results at FL8). In all cases unnormalized Vibro-acoustic signals for TBI rats were higher than those for sham rats, across all applied difference frequencies. Additionally,

in all un-normalized signals the spectral magnitudes measured at the carrier frequencies were higher in TBI versus sham rats. However, once normalized, Vibro-acoustic signals from sham rats appeared higher than those for TBI rats across all applied difference frequencies (see Figures BLAH for examples at FL8).

Discussion

In order to verify that our captured acoustic emissions represented more than simple backscatter from the skull we applied Vibro to rats (N=3) with and without skull at the same locations and depths as in the primary study, each rat acted as a self control. Signals acquired with skull were compared to those without skull via the Mann-Whitney U test (Sigma Plot, Systat Software Inc., San Jose, CA, USA), once again taking p-values ≤ 0.05 to be statistically significant. Comparisons indicated that the acoustic emissions acquired from rats with and without skull for any location and depth were not statistically significant. Additionally, Vibro applied with an intensity of 0.4 W/cm^2 SPTA, which marks the lower end of the applied intensity range, was able to generate acoustic emissions in which signal components were discernible from noise ($\text{SNR} > 1$). **From these analyses it follows that measurable Vibro-acoustic signals with SPTA intensities within FDA guidelines can be produced from the application of trans-cranial Vibro. Furthermore, comparison of these Vibro-acoustic signals from sham versus TBI rats indicates that Vibro is sensitive to the changes in tissue elasticity that occur following trauma. Given these findings Vibro presents a lucrative platform for new TBI detection technologies.**

Future Direction —> remove citation by Mao and Wagner 2011

With the basis set by these experiments work will continue in order to further refine the application of Vibro for the detection of TBI. In future studies additional measures will be considered in order to eliminate fluctuations in transducer output and amplifier gain. While the normalizations (N1 and N2) implemented here should minimize the influence of these fluctuations, further reduction may improve the ability to detect Vibro-acoustic signals from vibrating tissue. Additionally, future work would consider larger animals that have sustained closed-head TBI, such as from a focused blast, this would eliminate any influence the cranial window has on emitted acoustic emissions. Larger animals would also ensure that the ultrasound focus lays entirely within tissue and is not effected by the skull which is stiffer and less likely to respond to Vibro.

While Vibro presents a novel method by which to interrogate tissue for the presence of trauma its focal nature entails that scanning large regions would be inefficient. It appears that Vibro would be most successful if paired with a secondary TBI imaging modality with less resolution and specificity but a broader field of view. This would combine the high precision of Vibro with the capability to examine large regions quickly.

Conclusion

Vibro-acoustography (Vibro) applied trans-cranially is sensitive to the changes in tissue elasticity that follow trauma. As such, it represents a foundation for novel TBI detection devices that can be deployed in the field.

References

- Boulet T, Kelso ML, Othamn SF (2011) Microscopic magnetic resonance elastography of traumatic brain injury model. *J Neurosci Meth* 201:296-306.
- Boulet T, Kelso ML, Othman SF (2013) Longterm *in vivo* imaging of viscoelastic properties of the mouse brain following controlled cortical impact. *J Neurotrauma*. doi: 10.1089/neu.2012.2788.
- Deck MD, Henschke C, Lee BC, Zimmerman RD, Hyman RA, Edwards J, Saint Louis LA, Cahill PT, Stein H, Whalen JP. "Computed tomography versus magnetic resonance imaging of the brain. A collaborative interinstitutional study." *Clinical Imaging*. 1989 Mar;13(1):2-15.
- Dixon CE, Clifton GL, Lighthall JW, Yaghmai AA, Hayes RL. "A controlled cortical impact model of traumatic brain injury in the rat." *Journal of Neuroscience Methods*. 1991.
- Fatemi M and Greenleaf JF. "Vibro-acoustography: An imaging modality based on ultrasound-stimulated acoustic emission." *Proc. Natl. Acad. Sci. USA*. 1999.
- Faul N, Xu L, Waid MM, Coronado VG. Traumatic Brain Injury in the United States: Emergency Department Visits, Hospitalizations, and Deaths, 2002-2006. U.S. Department of Health and Human Services. March 2010.
- FDA. "Information for Manufacturers Seeking Marketing Clearance of Diagnostic Ultrasound Systems and Transducers." U.S. Food and Drug Administration. 9 September 2008.
- Fischer, Hannah. "U.S. Military Casualty Statistics: Operation New Dawn, Operation Iraqi Freedom, and Operation Enduring Freedom." www.fas.org. Federation of American Scientists, n.d. Web. 9 May 2013.
- Greenwald BD, Burnett DM, Miller MA. "Congenital and acquired brain injury. 1. Brain injury: epidemiology and pathophysiology". *Arch Phys Med Rehabil*. 2003.

Illian PR, Gross D, Lu W, Owen RN, Bailly MR, Mourad PD. "Interrogating and imaging renal stones using vibro-acoustography." J. Acoust. Soc. Am. Volume 129, Issue 4, pp. 2376-2376 (2011).

Kremkau FW, Barnes RW, McGraw CP. "Ultrasonic attenuation and propagation speed in normal human brain." J Acoust Soc Am. 70:29-38. 1981.

Lighthall JW (1988) Controlled cortical impact: a new experimental brain injury model. J Neurotrauma 5(1):1-15.

Mao H and Wagner C. "Material properties of adult rat skull." Journal of Mechanics in Medicine and Biology. 2011.

Miller, TC and Zwerdling, D. "Military Still Failing to Diagnose, Treat Brain Injuries". 2010 June 8. National Public Radio. <http://www.npr.org/2010/06/08/127402993/military-still-failing-to-diagnose-treat-brain-injuries>.

Park E, Bell JD, Baker AJ "Traumatic brain injury: can the consequences be stopped?" Canadian Medical Association Journal. 2008 April 22; 178(9): 1163-1170.

Pislaru C, Kantor B, Kinnick RR, Anderson JL, Aubry MC, Urban MW, Fatemi M, Greenleaf JF. "In Vivo Vibroacoustography of Large Peripheral Arteries." Invest Radiol. 2008.

Sauaia A, Moore FA, Moore EE, Moser KS, Brennan R, Read RA, Pons PT. "Epidemiology of trauma deaths: a reassessment." Department of Surgery, Denver General Hospital, CO. Journal of Trauma. 1995 Feb;38(2):185-93.

Urban MW, Alizad A, Aquino W, Greeleaf JF, Fatemi M. "A review of Vibro-acoustography and its Applications in Medicine." Current Medical Imaging Reviews. 2011 Nov 1.

Figure Captions

Figure 1A: H-148 HIFU transducer (black), confocal PVDF hydrophone (orange), and plastic coupling cone with aiming lasers. To couple the transducer to the rat's skull, the cone is filled with degassed water and sealed with latex. The volume of water in the cone can be adjusted with a pair of syringes connected to the cone's sides (not seen here).

Figure 1B: Mathematical simulation of the maximum pressure field generated by the H-148 transducer. The transducer face is depicted on bottom. In the pressure field, red indicates high pressure and blue low pressure.

Figure 2: Surgical procedure schematic. A hole was drilled in the skull 3 mm in diameter (red circle), located 3 mm anterior and 2 mm to the left of the lambda, which is the visible rear suture joint on the surface of the skull. Focused ultrasound was applied at the locations denoted by the yellow stars, which are both 5 mm anterior of the lambda and 3 mm left and right, respectively. The focus was aimed 5 and 8 mm deep at each location.

Figure 3A: Sample signal from an in vivo experiment, $\Delta f = 220$ kHz. The top panel displays the waveform collected by the PVDF hydrophone, unfiltered. The bottom panel displays the Fourier transform of the waveform. The two peaks occur at the carrier frequencies for the two elements, in this case 2.11 and 1.89 MHz. The emissions at the difference frequency are orders of magnitude below those at the carriers, but in most cases they stand out from those at neighboring frequencies (noise).

Figure 3B: Representative sample of the amplitude of the measured acoustic emissions of a given data collection run, with applied difference frequency along the horizontal axis and measured spectral frequency along the vertical axis. Each column represents the same signal such as that seen Figure 3A but after application of a Fast Fourier transform. The visible diagonal trend in the plot reaffirms that at each difference frequency, the acoustic emissions at that frequency stand out above the noise floor, indicating the presence of vibro-acoustography.

Figure 4A: Unnormalized Vibro-acoustic emissions from the Front Left 8mm location. Asterisks indicate a statistically significant difference.

Figure 4B: Vibro-acoustic emissions from the FL8 location, normalized with the N1 formula.

Figure 4C: Vibro-acoustic emissions from the FL8 location, normalized with the N2 formula.

TABLE

Table 1: Percent of difference frequencies at which Mann-Whitney U testing indicated a statistically significant difference in Vibro-acoustic emissions between sham and TBI rats.				
	FL5	FL8	FR5	FR8
Unnormalized	75%	62.5%	100%	0%
N1	0	50%	0%	0%
N2	37.5%	50%	0%	0%

Optimization of Ultrasound Elastography for Diagnosis of Traumatic Brain Injury

Capstone Design Project

Yayun Chen

ABSTRACT

Annually, an estimation of 1.7 million people in the U.S suffers from traumatic brain injury (TBI), in which 50,000 people die and another 85,000 people survive with long-term disabilities. CT and MRI are the current diagnostic tools for TBI, but the prevalent implementation of the devices is limited in undeveloped areas and near the battlefield. Consequently, a size deployable diagnostic tool that is able to present quantitative evaluation of TBI is needed. The purpose of the project is to optimize an ultrasound elastography machine for detection and quantification of TBI based on the theory that abnormal brain elasticity will be observed in presence of hemorrhage and edema. The goal is achieved in three steps: develop and test shear wave tracking algorithm in breast phantom and alginate, test, reproduce and modify the algorithm on control mouse brains, and finally construct elastograph on severe TBI mouse and find the most sensitive parameter for TBI diagnosis through quantitative statistics. The accuracy of elastograph will be ensured by SSI machine in breast phantom and alginate. Successfully optimized ultrasound elastography machine displays quantitative elastograph of brains, which simplifies diagnostic procedures. Furthermore, implementation of the device in hospitals and battlefields enables early TBI detection, which will potentially reduce TBI-related deaths, lower TBI-related treatment costs and greatly enhance residents' life quality.

Introduction:

Statement of Problem:

Traumatic brain injury (TBI) can be classified into three levels: mild, moderate and severe. Top three causes of TBI are car accidents, firearms and falls.^{1,2} Different levels of TBI will result in various extents of brain hemorrhage and edema. TBI symptoms include continuing and worsening headaches, loss of consciousness or memory, and in severe cases, dilation of pupils.^{1,3} Patients with mild TBI are able to recover in a few weeks or months. However, many troops back from the war suffer from moderate to severe brain injury, which will never fully recover and may need lifelong treatment.²

Operable scanning equipment such as Computed Tomography (CT) and Magnetic Resonance Imaging (MRI) has been used for TBI diagnosis.³ However, their bulky size limits their wide application; experienced operators are also required in order to give meaningful analysis of the image.⁴ Consequently, patients with brain injuries will have to be transported far away in order to receive proper diagnosis, which is a waste of time and money and can lead to further damage to the brain.⁴

Ultrasound transient elastography is a prominent candidate for TBI diagnosis due to its deployable size and potential to give a quantitative analysis. According to previous works conducted on ultrasound transient elastography, it is able to detect changes in brain elasticity after schematic stroke.^{4,5} It is also capable of measuring brain anisotropy in different regions.⁶ However, ultrasound elastography is not yet able to detect TBI due to factors such as low signal to noise ratio and huge skull artifacts.

The Verasonics ultrasound engine (VUE)¹¹ is a completely programmable PC-based ultrasound device. By coupling it with a conventional diagnostic probe, which pushes tissue non-destructively via acoustic radiation forces from focused diagnostic ultrasound (FDU), VUE can be programmed to perform ultrasound imaging. By post-processing the data and modifying ultrasound parameters, VUE has the potential to display brain elastography. According to the previously proved hypothesis, brain elasticity will vary in presence of edema and hemorrhage. Consequently, the ultimate goal of the project is to design and optimize VUE, so that the machine will be able to generate TBI sensitive ultrasound elastography that is able to detect, classify and quantify TBI with minimum artifacts.

Significance:

According to the statistics compiled by the Centers for Disease Control and Prevention (CDC), an estimated 1.7 million people suffer from TBI each year and the condition has become a leading factor 30.5% of injury-related deaths in the United States.¹

³ Moreover, “TBI and concussion” is reported to be the most common combat-related injury and account for nearly 25% of combat casualties.² Although protection strategies such as body armor and Kevlar helmets are available, the head remains insufficiently protected.² These advances increase the number of survivors from the war but also results in more soldiers with permanent defects in their brain due to TBI.² Since traumatic brain injury is influencing more and more people’s lives, especially the welfare of soldiers coming back from war, proper diagnostic methods are definitely needed in order to perform the right treatment. Because current approaches to TBI, i.e. MRI, magnetic resonance elastography (MRE) and CT, have many limitations in terms of accessibility, accuracy, and diagnostic time, the need for a highly accurate and accessible TBI diagnostic approach becomes more and more urgent. Not only medically, the project is also technically significant because ultrasound elastography is a recently developed technology that has only been working on breasts in the clinic. Applications of the technology on many other organs, including liver, kidney and brain are under extensive research. Consequently if the design and optimization of VUE for brain imaging is successful, it will become a new scientific breakthrough, which proves the sensitivity of shear wave in tissues other than breasts. Additionally, the technology will be widely applied in the medical field because of its capability to produce real-time brain elastographies with little or no artifact from the skull. By referring to the shear modulus maps constructed by VUE, the operator may be able to diagnose brain injury according to the highlights in the image. Classification with respect to level of injury can be achieved by looking at the amount of change in elasticity. Due to its portability and reasonable price, VUE will ultimately be implemented in battlefields, hospitals and other places where effective imaging machines are not available, and the broad application of the device will enhance the lives of millions of people.

Ethical and social issues

Animal models in the experiment can cause ethical concerns because rats and mice will undergo mild to moderate TBI surgery, imaging and finally perfusion. However, the Institutional Animal Care and Use Committee (IACUC) approved all surgery protocols, anesthesia and chemicals used in the experiment.⁷ IACUC is an entity that regulates proper use of laboratory animals for research and instructional purposes. By strictly complying with IACUC laws on animal handling and surgery, ethical issues associated with animal experimenting can be avoided.

Successful research outcomes provide an accessible and portable approach for early detection and diagnosis of traumatic brain injury. This will largely benefit society by reducing TBI-related deaths and enhancing life quality of residents. In addition, annual cost of TBI treatment in the U.S has been estimated to be 48.3 billion dollars, and individuals suffering from severe TBI tend to spend 4 million dollars over the entire life.⁸ Consequently early detection of the disease prevents deterioration of TBI and can potentially benefit the society by reducing medical costs.

Economic issues:

The project requires large economic support because experiments consume huge number of animal models, including rats, mice and potentially, pigs. Drugs such as Lidocaine, Buprenorphine and Bupivacaine and chemicals such as paraformaldehyde (PFA) and isoflurane are also inevitable as they are required for surgical procedures according to IACUC. Instrumentation used in the lab is SSI and VUE, which costs millions of US dollars and needs regular updates and renewals.

The military is the sponsor for the project because a large portion of casualty from war suffers from blast-induced neurotrauma (BINT), which is a typical type of TBI.⁴ Owing to the fact that there is currently no portable equipment near the battle field able to perform TBI diagnosis, the military is interested in funding the project since the construction of a portable and accurate TBI diagnostic machine will greatly enhance the clinical condition and welfare of soldiers. Other organizations such as National Institute of Health (NIH) may also be willing to fund the project because the diagnostic machine can be implemented in hospitals and ambulances, which will greatly benefit residents.⁴

Technical Background

Theory:

The project aims to quantify TBI using ultrasound elastography based on the hypothesis that tissue elasticity value will vary in the presence of injury due to hemorrhage and edema. The hypothesis has been proven through the preliminary work in the lab on a total of 60 rat models, and conclusions have been drawn that normal brain tissues have a significantly higher shear modulus than damaged tissues.

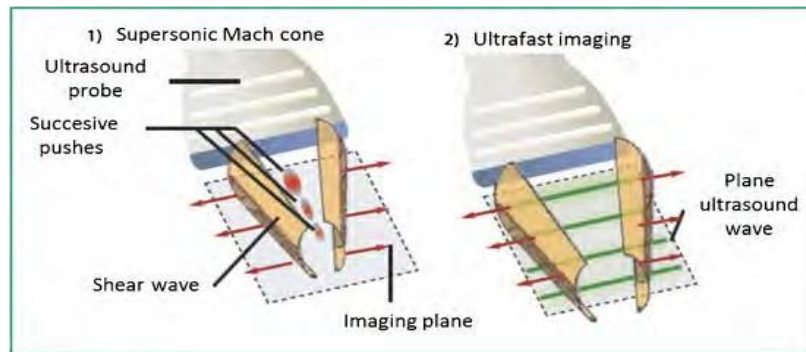


Figure 1: 1) FDU probe sends out “push” beams at focal spots, inducing SW propagation in imaging plane. 2) Ultrafast imaging system image shear wave propagation plane after “push”.⁹

Ultrasound elastography displays tissue shear modulus via focused diagnostic ultrasound (FDU) beams. The FDU transducer (fig.1) connected to VUE is able to send out sequences of radiation “pushes” to induce non-destructive tissue displacements. The tissue displacements generated by the sequences at one location will then form a downward wave front (fig.2), which is able to propagate transversely through the tissue. The wave caused by the induced tissue displacements is called a shear wave (SW). After sending out “pushes”, the probe will start taking images (fig.1 and fig.2) at an adjustable frequency with the highest value of 8000Hz, which records videos of (SW) propagation at different time frames. Post processing and filtering of the pictures will produce a video clip (fig.3), displaying the propagation of wave front caused by the downward tissue displacement.

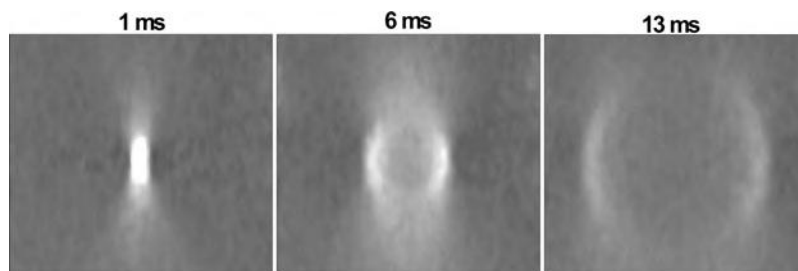


Figure 2: SW propagation three time points after “push” in B-mode. White scale indicated tissue displacement.¹⁰

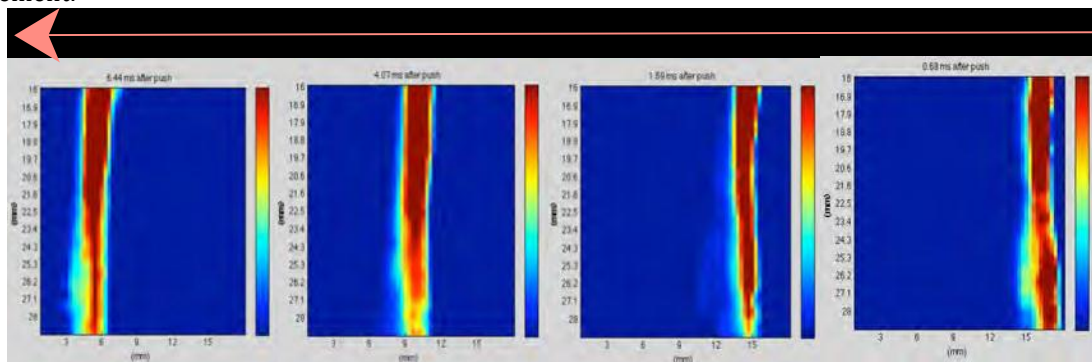


Figure 3: Fragment of SW propagation over time in alginate: red indicates local maximum vertical displacements. Notice that the SW starts on the right and propagate toward the left.

Due to the fact that similar shapes of wave fronts will form along the length of tissue when SW moves through, the propagation can thus be tracked by cross correlating displacement data between two different time frames at each depth of the image (fig.4).^{9, 10} The cross correlation algorithm calculates pixels moved in order to most accurately overlap two waveforms, and the resulting number of pixels is equal to the SW propagation distance. As a consequence, SW velocity can be found with distance moved in the known amount of time difference. Referring to papers in the related field, shear modulus (G) is related to SW velocity in the form $G = 3 * \rho * c^2$, in which ρ is the density of tissue under imaging and c is the speed of SW.¹⁰ By applying this equation, the shear modulus for each grid can be calculated and put together to construct a map. In the preliminary stage of the design period, a commercialized Aixplorer Multiwave Ultrasound System (SSI) for breast imaging will be used as a standard test for the accuracy of VUE.

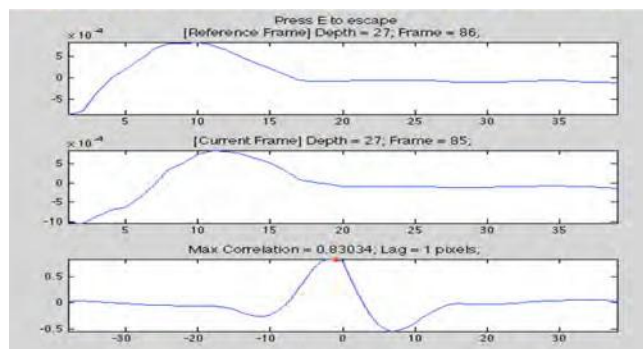


Figure 4: Cross correlation method. The first window is the waveform at an early time frame, and the second window is the waveform at the latter time frame. The third window shows the correlation function of the two waves.

Review of Literature:

CT and MRI, shown in fig.5 have been two commonly used ways in diagnosis of TBI over the past twenty years⁴. The way they work is to provide visualization of brain structures, shown in fig.6.¹²

MRI has been widely used clinically to diagnose central nervous system disease, cardiovascular disease, tumor, and head and neck health.¹³ MRI is very safe because it uses non---ionizing radiation. The imaging modality involves the use of paramagnetic contrast agents, thinner slices and surface coils, which provides high spatial resolution and specificity.¹³ Compared to CT, MRI is able to give more detailed information about the brain: small brain damage, usually 1---2mm, can be seen on an MRI.¹⁵ One major limitation of MRI is that it cannot be operated on patients with ventilation equipment or pacemaker because of the magnetic field it creates. Additionally, according to Sahraian and Eshaghi¹⁴, MR imaging has no pathological specificity when used to infer microstructural information (i.e. any change in brain tissue composition (inflammation, edema, or demyelination) can change MRI signal).

Diffusion tensor MR imaging (DT---MRI) specifically targets brain white matter. The technology studies the diffusion of water molecule in tissues containing a large amount of fibers, such as white matter.³⁵ Water tends to diffuse fastest along the direction of fibers. Consequently, based on how water diffuses in tissue, DT-MRI is able to produce 3D representation of the tissue.³⁵ Studies have shown that this imaging modality is able to have a more complete assessment of brain health and disease.^{34,35} However, many patients find MRI intolerable as the process is long and often takes place in a confined space.¹²

CT, on the other hand, is better at detecting the presence of fresh blood around the brain and is mostly used in acute TBI diagnosis.¹² Both MRI and CT require highly trained and experienced operators so as to give a meaningful interpretation of the image, which increases the chance of human bias and error during diagnosis.¹² Moreover CT has poor resolution, low post---acute value and can induce cell death, cancer or other health problems due to the exposure to x-rays, which is a high-level ionizing radiation.¹²



Figure 5: [Left] Schematic graph of MRI (left) and CT scanner (right) ¹² [Right] Brain image from MRI (left) and CT scanner (right) ⁴

Magnetic Resonance Elastography (MRE) is a new imaging technique (fig6) that has recently been studied in vivo on both small animals and humans. MRE is a non-invasive technique; it works by providing visualization as well as quantitative viscoelastic properties of the tissue being imaged, shown in fig.6.⁹ MRE determines the shear modulus of tissue by obtaining the propagation speed of shear wave generated via an external vibrator based on the fact that shear wave travels at various speeds in tissues with different elasticity.⁹ By measuring the elasticity change in tissue, which often times is an indication of disease, MRE will be able to detect the region of abnormality.

The technology has been applied to several parts of human bodies such as breast, skeletal muscle and prostate to assess tissue properties.^{6,19} Meanwhile, extensive research targets the use of MRE to non-invasively study the viscoelastic properties of human brains in vivo.^{16,17,18} Recent reports from Murphy et al. suggests a decrease in the elastic properties of human brains with neuroinflammatory and neurodegenerative disorders, including Alzheimer's disease, using MRE.²⁰ U Hamhaber et al. used MRE to measure SW velocity in human brain, and found the average velocity to be 1.88 m/s.²¹

However, when MRE is used to evaluate local brain properties, large discrepancies appear in literature in terms of the exact shear modulus value in the specific regions of the brain. Referring to the previous research conducted on MRE in vivo, the elasticity of brain is significantly different between white matter and grey matter. According to McCracken¹⁶, the brain white matter has a shear modulus of 10.7 ± 1.4 kPa and the grey matter has a shear modulus of 5.3 ± 1.3 kPa; while Michael A. Green¹⁹ and his colleagues who measured brain viscoelasticity via 3D reconstruction method got a shear modulus value of 2.7 ± 0.1 kPa for brain white matter and 3.1 ± 0.1 kPa for brain grey matter. Many similar

experiments were performed and the value of shear modulus varied from 1--12 kPa.^{16, 18, 19,}
²¹ The lack of consistency can be attributed to variation in sample types, methods, and imperfection in the technology such as artifacts.

MRE needs a very long acquisition time, usually 20 minutes, in order to obtain a quantitative evaluation of the tissue under imaging.²² Short scan times, which is usually the case in human study, leads to acquisition of data with poor spatial resolution.²² Due to its limited spatial resolution, MRE is only able to give averaged mechanical properties over the whole brain or over large ROIs, which disables its application to diagnose localized injuries.²² Moreover, the amplitudes of high frequency vibrations generated by MRE attenuates rapidly in the middle of the brain, which significantly lowers the signal to noise ratio of the deformation data.²² Therefore, the application of this technology as a routine diagnostic tool for both research and clinical use is limited.

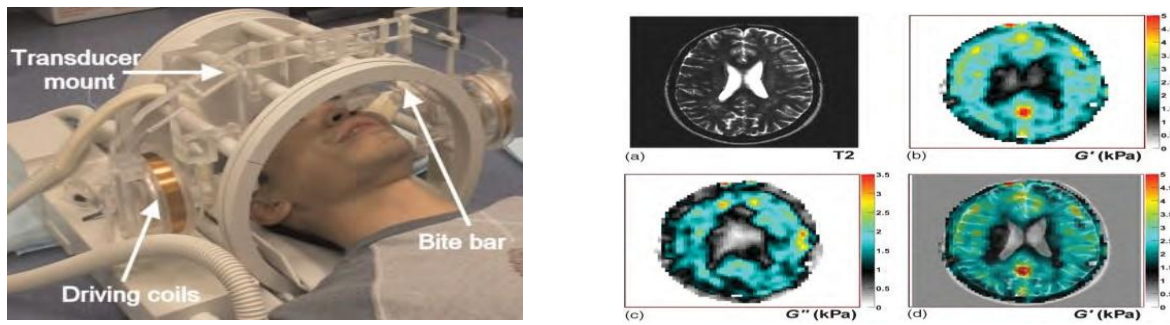


Figure 6: [Left] MRE set up with external vibrator, transducer mount, driving coils and bite bar. [Right] MRE in vivo image (a) T2-weighted MR image; (b) G' (kPa) image; (c) G'' (kPa) image. (d). overlapped image of b) and a).¹⁹

Ultrasound transient elastography was first developed in the 1990's.²⁵ The technology uses the same concept as MRE, in that tissue viscoelasticity can be evaluated via shear wave propagation, an example of shear wave is shown in fig.7. Different from MRE, ultrasound transient elastography utilizes a transient mechanical excitation of tissue instead of prolonged vibration, which naturally separates shear wave from compression waves as shear wave travels three times slower.^{9, 23} This technology effectively reduces wave overlapping and thus increases SNR. In order to more specifically study the shear wave propagation in medium, the Institute Langevin developed an ultrafast ultrasound imaging acquisition system in 1997, which allows storing of 2D data acquired at a frame rate of 5000 to 30,000 images per second, followed by conversion of which into a map of

shear modulus.^{9, 23} The combination of the two ideas (transient excitation and ultrafast imaging) results in today's shear---imaging technique.⁹

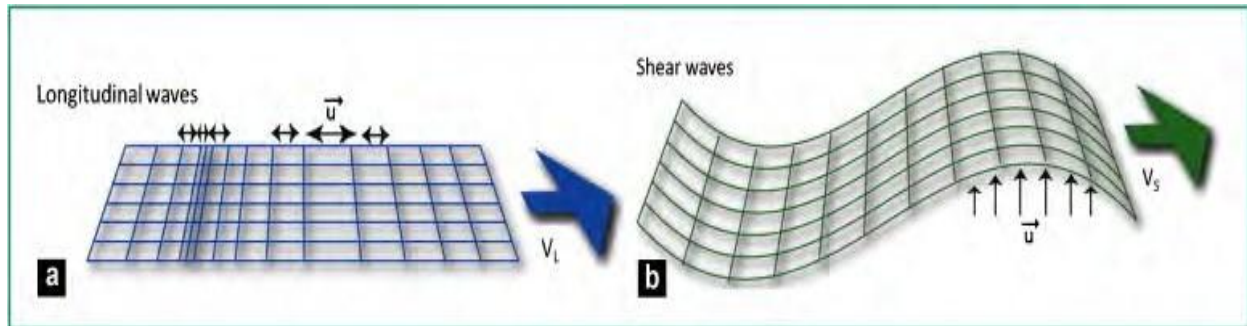


Figure 7: Comparison of ultrasound wave to shear wave. [Left] Longitudinal ultrasound wave induce medium movement in the same direction of propagation. [Right] Shear wave results from perpendicular medium movements relative to the direction of propagation.⁹

Shear imaging technique has been widely applied to study many organs, including thyroid, gastro-intestinal tract, kidney, and, most successfully, breast and liver.^{24, 25, 26, 27, 32} BK. Kim et al. reported that shear imaging provided an alternative non---invasive method to access severity of liver fibrosis.²⁸ Additionally, the technology is able to provide more detailed prognostic information than traditional liver biopsy by tracking dynamic changes in fibrotic burdens.²⁸ According to an in vivo study conducted at Institute Curie on human breasts, 50 patients with or without breast lesions were involved, and shear imaging was demonstrated to clearly differentiate between benign and malignant tissue (fig.8).²⁹ Further study by W.A. Berg et al. in 939 patients with breast cancer showed that shear imaging had high specificity for breast lesion characterization.³⁰

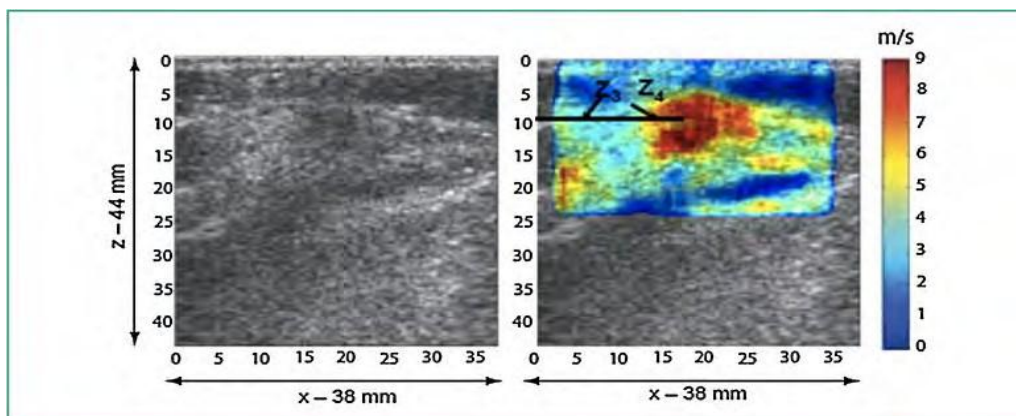


Figure 8: Ductal infiltrating carcinoma. [Left] B-mode image shows only blurry edge of the lesion. [Right] Shear imaging highlights the lesion with observably high shear wave velocity, which corresponds to high tissue stiffness.²⁹

Because of shear imaging's high spatial resolution to provide local tissue stiffness, efforts have been made to apply the technique on brains in small animals such as rats and mice. However, the technology fails to measure brain viscoelasticity due to huge amount of artifacts resulting from the brain's tiny size plus the presence of skull, which reflects shear waves from the edge and causes them to overlap.^{4, 6, 31} Consequently, extensive research is going on regarding optimization of ultrasound transient elastography that can overcome current roadblocks, thus allowing accurate evaluation of brain stiffness.

Previous Work:

In Mourad's lab, experiments and data acquisition on rat and mouse brains after surgeries were carried out using SSI with linear SL 15-4 MHz transducer in order to prove the hypothesis on decreased tissue elasticity due to injury. Because the SSI machine is designed for imaging in breast tissue, its application on brain results in huge artifacts due to SW overlaps at the brain edge and skull reflections. An example of SSI imaging result on mouse is shown in fig.9.

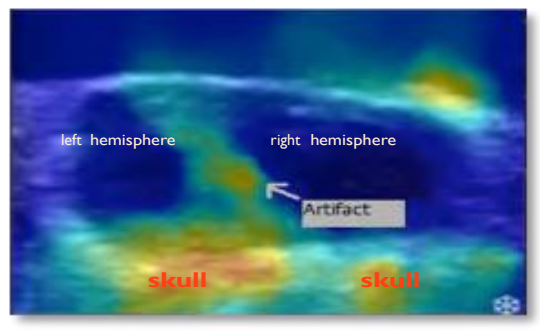


Figure 9: Shear modulus map of mouse brain with two cranial windows imaged by SSI. The arrow indicates site of artifacts caused by the skull, which has much higher elasticity value than actual brain.⁴

In stroke surgeries, ultrasound transient elastography was performed on mouse brains 24 hours and 72 hours after occlusion in the middle cerebral artery.⁵ Shear moduli were obtained for both ipsilateral and contralateral hemispheres and the data were compared to that of the control mouse brains. According to the result of the experiment, shown in fig.10, stroke mouse brains after 24 hours displayed significant shear modulus decrease in the ipsilateral hemisphere and significant shear modulus increase in the contralateral hemisphere, both with p values less than 0.01. No difference was found between 72---hour brains ($p>0.05$) but the shear modulus for 24---hour and 72---hour mouse

brains varied greatly in both hemispheres ($p < 0.01$). The experiment proves the ability of this specific version of ultrasound elastography to detect subtle changes in brain elasticity in the presence of artifacts after induction of ischemic stroke.⁵

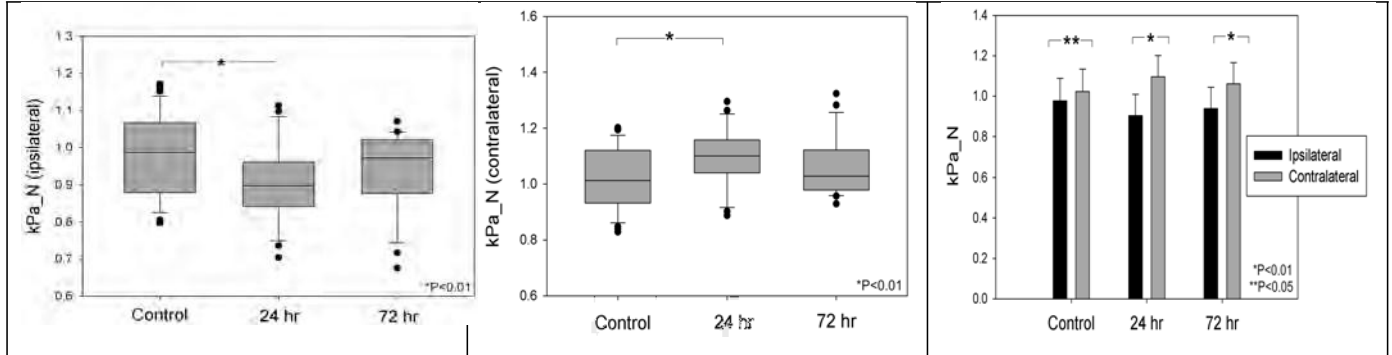


Figure 10: [Left] Normalized Ipsilateral Shear Modulus for control, 24-hour and 72-hour mice ($P < 0.01$) [Middle] Comparison of normalized mean shear modulus of ipsilateral and contralateral hemisphere for all three populations: Control, 24-hour and 72-hour mice. * $P < 0.01$ ** $P = 0.04$ [Right] Normalized Contralateral Shear Modulus for control, 24-hour and 72-hour mice ($P < 0.01$)⁵

In TBI surgeries, brain shear modulus values were evaluated acute and 24-hour after moderate TBI simulations using the same SSI machine. A total of 60 live rats were used in the experiment, and each 20 of them were 24-hour, acute and control rats respectively. TBI surgery was performed through a 1-mm cortical impact on the right hemisphere, and skulls were removed on both sides of the brain, leaving the middle line intact. MATLAB was used to contour the images for clear visualization, and ANOVA was applied to provide statistical analysis, including mean, standard deviation and p value of the two hemispheres. The brains were perfused after imaging to obtain histology results of the injury. According to coronal images, the average rat brain shear modulus was different between 24-hour TBI and control rats while no significant difference was observed between acute TBI and control rats. The experiment showed that 24-hour after TBI, the injured hemisphere had significantly decreased stiffness, which, according to histology results, was due to presence of edema and hemorrhage. Fig.11 illustrates the experiment's statistical results.

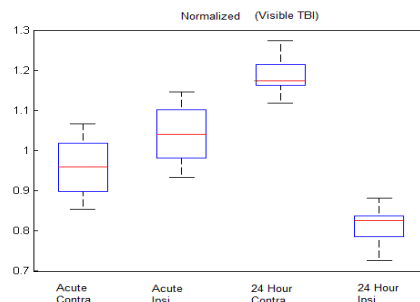


Figure 11: Bar plots of normalized acute, 24-hour contralateral and ipsilateral brain stiffness values, in which the 24-hour brain has decreasing stiffness in injured hemisphere and increasing stiffness in contralateral hemisphere. ($P < 0.01$)

The preliminary data prove that brain elasticity will change due to edema and hemorrhage caused by TBI or stroke, and the change is statistically detectable even using the SSI machine, which is not optimized and has huge artifacts. This result supports the hypothesis for the project. Therefore, modification and optimization of VUE to enable detection and classification of brain injuries becomes a promising goal.

Outstanding Technical Issues:

Presence of artifacts in SSI was the most outstanding issue in the beginning of the project. Because of the unavoidable artifacts from skull, it became impossible to determine the real shear modulus of brain under imaging. Consequently, the newly generated SW tracking algorithm could not track the SW movie exported from SSI. As a result, the design of VUE was prohibited due to lack of a standard comparison.

Another technical problem that emerged at the outset was the low signal to noise ratio of displacement data exported from VUE. As SW propagated through tissue, the intensity of which dissipated, and there were reflections coming from boundaries due to the tiny size of the brain. This made the detection of wave very hard.

The brains were then put into alginates to eliminate reflection from skull. However, since the SW impedance of alginate did not match that of the brain, although SW appeared to be perfect in alginate, it became a mess when hitting the brain---alginate interface, and disappeared or broke apart when entering the brain. Because there is no reliable literature that indicates brain SW impedance, many alginate molds with different percentages varied by 0.1% were tested in order for SW to propagate smoothly. This procedure significantly slowed down the experiment progress.

Design of Tools, Device, and Experiments:

Overview:

The goal of this project is to build and optimize a deployable sized ultrasound elastography device VUE capable of highlighting and classifying areas of damage caused by moderate and mild traumatic brain injury (TBI). The device should be able to differentiate injury types (i.e. hemorrhage, edema and traumatic axonal injury) and classify damage

extents (mild, moderate) from TBI. Traditional approaches such as MRI and CT are mainly limited by their size and cost; newly developed MRE uses external vibration source to induce tissue displacement inside the brain, but the technology requires very long acquisition time, which limits its application for routine diagnosis. VUE is an alternative promising candidate to achieve the goal: the diagnostic probe in VUE sends out radiation “pushes” to induce non-destructive tissue displacement, after the pushing sequence VUE is able to take images as SW propagates through the tissue and convert the data to shear modulus values, enabling real time visualization of elasticity images. Because VUE is fully programmable, modifications can be made on pushing sequence, duration and averaging pixels, which are capable of avoiding SW overlap due to skull reflection. Successful programming and design will enable VUE to produce brain elasticity maps that quantifies and classifies various types of TBI with high level of accuracy.

Phase 1: The goal of this phase is to construct stiffness maps in breast phantom and alginate. This is achieved by post-processing of ultrasound data from VUE and performing shear wave tracking in MATLAB. The outcome of this phase is the construction of shear modulus images that are able to display accurate breast phantom stiffness and detect lumps.

Phase 2: The goal of this phase is to construct stiffness mapping in rats with moderate TBI. This is achieved by post-processing of ultrasound data from VUE, and performing SW tracking in MATLAB. Additional work such as rat surgery, perfusion, histology and artifacts prevention are required in the process. The outcome of this phase is the construction of artifact-free shear modulus image that is able to highlight moderate TBI sites.

Phase 3: The goal of this phase is to apply the outcomes from phase 2 to detect mild TBI in rat brains. This is achieved by modification of previous MATLAB codes in phase 2 to fit for mild injury detection. Mild TBI surgery on rats is required in the process. The outcome of this phase is the construction of a shear modulus image that is able to highlight as well as differentiate mild TBI sites from moderate ones.

Revised Methods:

In phase 1 of the project, SW tracking in breast phantom and alginate turned out to be successful at early stage. However, in phase 2, due to the small size of rodent’s brain, and the unavoidable skull interference, SW propagation in brain tissue in vivo became very

noisy and untraceable. Consequently, further experiments were carried out in vitro. Control mouse brains were taken out and submerged in different percentage of alginate molds to optimize imaging. SW tracking algorithm was also modified to optimize brain elastograph. In phase 3, both 24-hour TBI and control mice were studied to determine the most TBI-sensitive imaging parameters, and give a quantitative idea of the stiffness of mice brains. The purpose of this significant revision of the design process is to create an imagine media that is big enough to fit the transducer head, and which also has the closest SW propagation impedance as the brain itself, so that when FDU generates pushes, SW will propagate smoothly from the alginate media into the brain tissue, and the tracking algorithm will be able to capture any abnormality of the propagation caused by the presence of injury.

Materials and Methods:

Animal models of mice were used in both phase 2 and 3 of the study. Drugs used associated with animal surgeries were B-euthanasia, Lidocaine, Buprenorphine, and Bupivacaine. Other materials included breast phantom, alginate powder, sodium chloride, and sodium dithionite. The devices used were SSI, VUE, Pneumatic Impact Device³³, and L4-7 ultrasound transducer.

The design strategy was composed of two major parts. One part was to optimize SW tracking algorithm. To achieve this goal, two sets of algorithms with different correlation methods were developed and tested in alginate; various time frame lag for SW tracking were chosen and compared; weighted space averaging and interpolation of correlation coefficients were also coded into the tracking algorithm. The other part was to optimize SW propagation through media. To achieve this goal, various percentages of alginates were made and imaged; different “push” duration and active “push” elements were chosen and tested; averaging effect of time frames and pixels were studied; color percentage of SW visualization was also manipulated to show the best propagation.

Data with different combination of “push” duration and active “push” elements were collected using SSI and VUE at the same position on breast phantoms, alginates and brain-containing alginate molds (the set-up of the alginate molds is shown in fig.12). Displacement data from both devices were exported, as well as the elastograph from SSI. The exported displacement data were post-processed according to the strategies above, and then fed through different SW tracking algorithms, giving elasticity maps. Mean and

standard deviation were calculated from each generated elastograph, and the results of breast phantom and alginate were compared to the standard image from SSI.

Mouse brains were used to test the alginate recipe and SW tracking algorithm to give the best and most consistent result. Control animals were sacrificed by cervical dislocation (mice) or B-euthanasia (rats). Their brains were later put into alginate molds. TBI animals were given severe TBI surgery, in which a small hole in the animal skull will be drilled on the right hemisphere to just fit the cortical impactor, then the animal will be impacted by 1mm into the brain. The animal will be sutured up 10 minutes after impact and sacrificed after 24 hours.

Costs: (1 page excel):

Table 1: experimental costs

Item	Cost
VeraSonics Ultrasound Engine	\$58,000
L7-4 Transducer	\$2400
180-220g Sprague Dawley Rats	\$24.25/rat
Mito mice	(Free) bred in lab
Nitrogen tank	\$13.66/tank
Oxygen tank	\$11.51/tank
Roungours	\$335.00 each
Forceps #45	\$25.50 each
Buprenorphine Hydrochloride Injection	\$31/1ml
Lidocaine	\$5/bottle
Bupivacaine	\$5/bottle
B-euthanasia	\$98/bottle
Isoflurane	\$10/bottle
Alginate	\$14.10/lb
Simethicone	\$3.24/1 fl oz
Sodium Chloride	\$36.10/500 g
Isopropanol	\$209.85/4L
Sodium Dithionite	\$15.03/500 g

Design Process:

In part 1 of the design process, data were obtained from breast phantom and 2.5% alginates because of their homogeneous medium property. The resulting images were compared to that of SSI in the same ROI in terms of mean, standard deviation, minimum and maximum values.

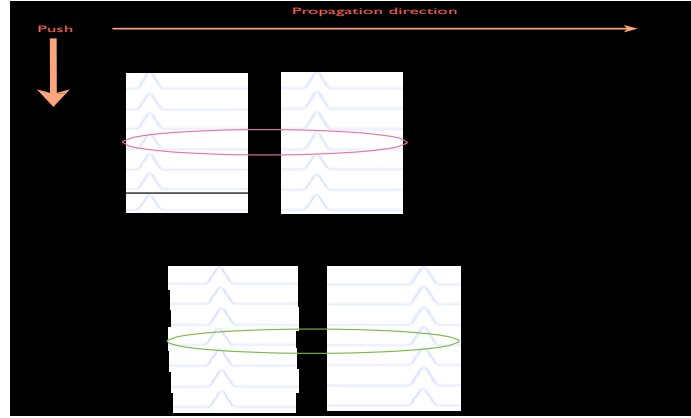


Figure 12: Example of correlation overview: correlation occurs between the 1st frame and the 9th frame, the 2nd frame and the 10th frame and so forth. K is equal to 8 in this case.

Correlation methodology:

Recall in fig.3 that SW propagation data is composed of 111 2D maps over a total time period of 20ms. Each 2D map represents the vertical displacements of elements in the ROI at one time frame, and correlation method was used to find SW velocity and thus tissue elasticity. The overall correlation pattern, shown in fig.12 as an example, was designed to correlate data in the n th frame with that in the $(n+k)$ th frame, the $(n+1)$ th frame with that in the $((n+1)+k)$ th frame, and so forth, in which k is the number of frame lags used in the tracking. The resulting SW velocity and shear modulus was assigned to all the horizontal pixels involved in the k frames.

Two separate correlation methods were designed and tested. Linear correlation method correlates the entire line of data. Max value correlation finds the start of wave front, and defines region of correlation to be pixels starting from wave front to the end of the line, and same region k frames later, as shown in fig.13. For each set of data, post-processing was performed using two correlation methods with frame lag k chosen to be 5, 10 and 15 respectively.

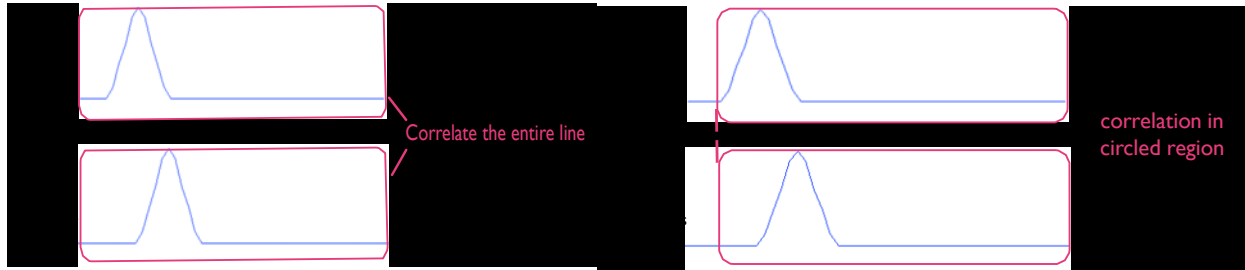


Figure 13: [Left] Same line of displacement at two time frames separated by 8 units, correlation occurs over the entire line of data. [Right] Same line of displacement at two time frames separated by 8 units, correlation occurs in regions of red boxes.

Interpolation of cross correlation:

Recall from fig.4 that a cross correlation function gives correlation coefficient and horizontal movement of two waveforms in pixels in order for them to overlap. This leads to a shortage of the algorithm in that SW movement less than 1 pixel cannot be detected. Consequently, interpolation of the cross correlation function was performed in MATLAB using “polyfit”, which refits the function with a polynomial, and increases the accuracy and spatial resolution of elastograph by detecting SW movements within 1 pixel.

Weighted average based on correlation coefficient:

Weighted average of SW velocity and thus shear modulus was performed based on correlation coefficients. Correlation coefficients vary from 0 to 1 for no correlation to perfectly positive correlation. These coefficients are used to weight the shear modulus when averaging. As SW movement overlaps spatially in each tracking (i.e. 1st and 9th frames, 2nd and 10th frames and etc.), averaging algorithm in space was used to enhance the accuracy of results. Fig.14 shows how spatial averaging was performed in the horizontal direction at a certain depth.

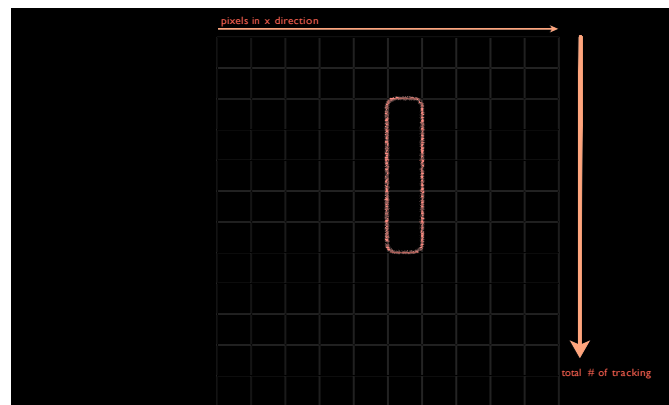


Figure 14: Weighted average example: spreadsheet shows the obtained SW velocity after each tracking at a certain geometric depth. Weighted average is performed using correlation coefficient and vertically, where there are overlapping values in the same x pixel, as circled out in orange.

Cross correlation coefficient is used for weighted average of SW velocity in each line. According to figure 4, weighted average is performed through each column among the non zero pixels, and finally form a line of averaged SW velocity. The velocities are then used to calculate shear modulus, and the same algorithm is applied to each line of displacement data.

In part 2 of the design process, different percentage of alginate modes, ranging from 4.4% to 4.7%, were made. 0.9% saline was used as solvent to protect brain damage from osmotic pressure, and the solution was kept at 4°C to slow down the alginate solidifying reaction. 2% of isopropanol, 0.3ml/100ml of Simethicone and 0.5g/1.0L of Sodium Dithionite were added to increase the homogeneity and decrease bubble formation in alginate. The goal was to find an alginate recipe that has same SW impedance as that of brain, which is equal to the product of medium density and SW velocity. Two layers of alginate were poured into the container, in which the bottom layer acted as a platform for brain to sit on, allowing the top layer to cover the brain. As alginate tends to change its elastic property over time, data were collected between 10-30 minutes after solidification of the top layer. Animals were sacrificed after the settlement of bottom alginate layer, and the brain was kept in 0.9% saline solution to reduce its change of property. SW movie collection was performed at four different positions around the brain, shown in fig.15. At each position, five various combinations of “push” parameters were chosen respectively for data acquisition, and the filtering parameters were altered to reduce noise in SW propagation, shown in fig.16.

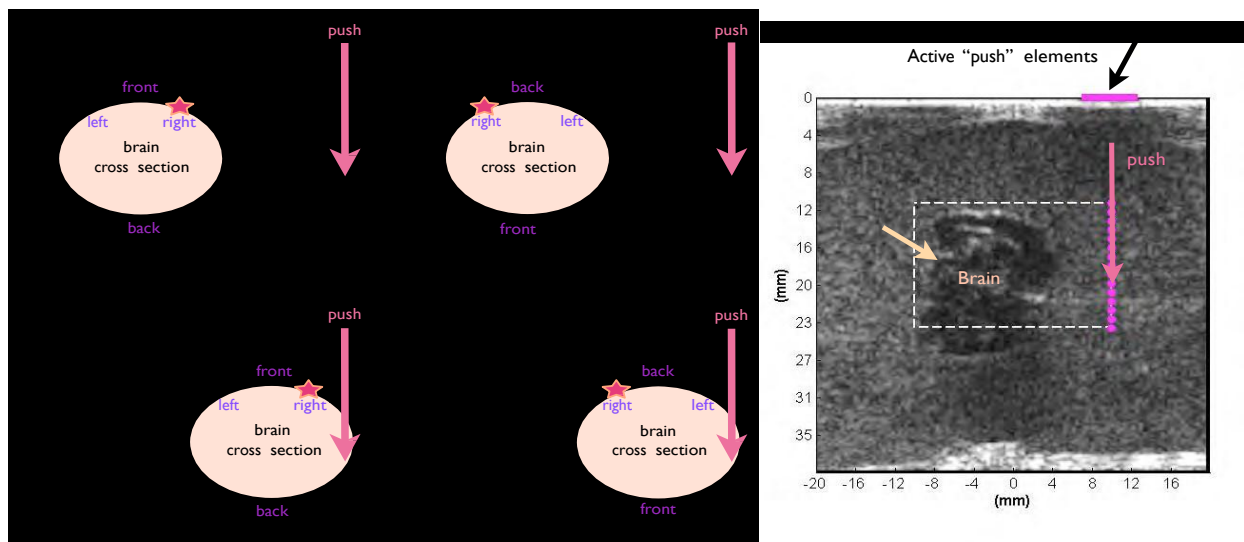


Figure 15: [Left] Schematics of brain-alginate setup and imaging positions 1–4. In position 1 and 2, SW initiates in alginate, and propagates through the alginate into the brain. In position 3 and 4, SW initiates in brain, and propagates through the brain into alginate. The pink star indicates site of TBI injury for TBI animals. [Right] A real example of schematics in B-mode image: the dotted square indicates ROI, in which the data were post-processed in MATLAB, the pink arrow indicates position of FDU “push”, the yellow arrows indicates the brain, and the horizontal pink line at the top is the actual active pushing element in the transducer.

Combinations	1	2	3	4	5
<u>Push Duration (us)</u>	24.25	28.625	32.125	36.5	40
<u>Active Push Elements (#)</u>	16	28	40	52	64

Filter Width [2-64] 5
Filter Depth [2-128] 30
Filter Frames [2-60] 3
Lower Color Prctile 75
Upper Color Prctile 95

Figure 16: [Left] Table of five parameter combinations: data were collected accordingly in order to find the push type that works best. [Right] Data filtering options: the parameters can be manually altered to smooth out SW propagation in brain.

The brain hemispheres were accurately contoured (accuracy up to 0.5mm) out during elastograph analysis according to B-mode images. The hemisphere difference and image quality were first determined qualitatively based on mean value and homogeneity in alginate, presence of artifacts, and inter-hemisphere difference in brain. Then, parameters with equal image quality underwent quantitative analysis in the same specified region for mean, standard deviation, and ANOVA tests. The goal of the quantitative analysis is to find a parameter combination that is most sensitive to diagnose TBI.

[illegible]

til Q
■ ■
..S Q)
til ()
E-0

Data:

Breast Phantom and Alginate Elastograph:

At the end of summer 2012, a preliminary SW tracking algorithm was designed. There was no averaging or interpolation of data. The algorithm was tested in breast phantom use SSI.

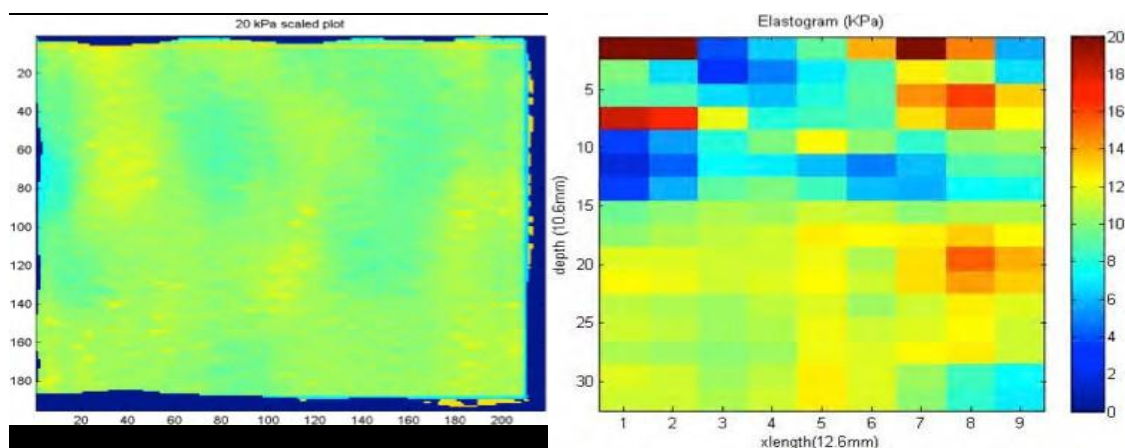
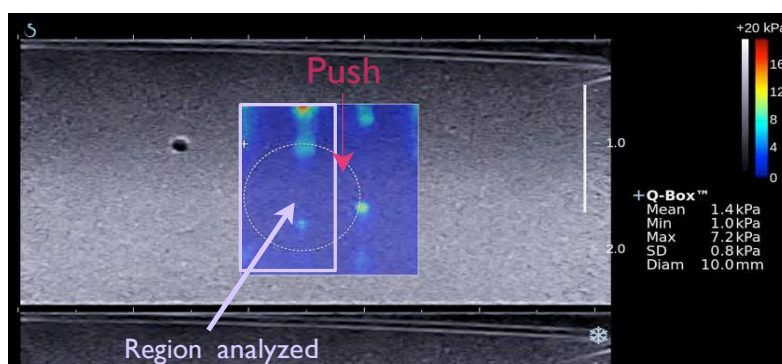


Figure 17: [Left] Breast phantom elastograph in the scale of 20 kPa generated by SSI. [Right] Same breast phantom elastograph in the scale of 20kPa generated by SW tracking of the SW data exported from SSI.

In fall 2012, the SW tracking pattern was modified to largely increase spatial resolution and two SW tracking algorithms were developed (linear and max value tracking). The effects of different frame lags k (recall that it is the parameter that determines the frame separation of correlation data pairs) were also studied. Data acquisition and comparison were conducted in 2% alginate in both SSI and VUE.



Figure

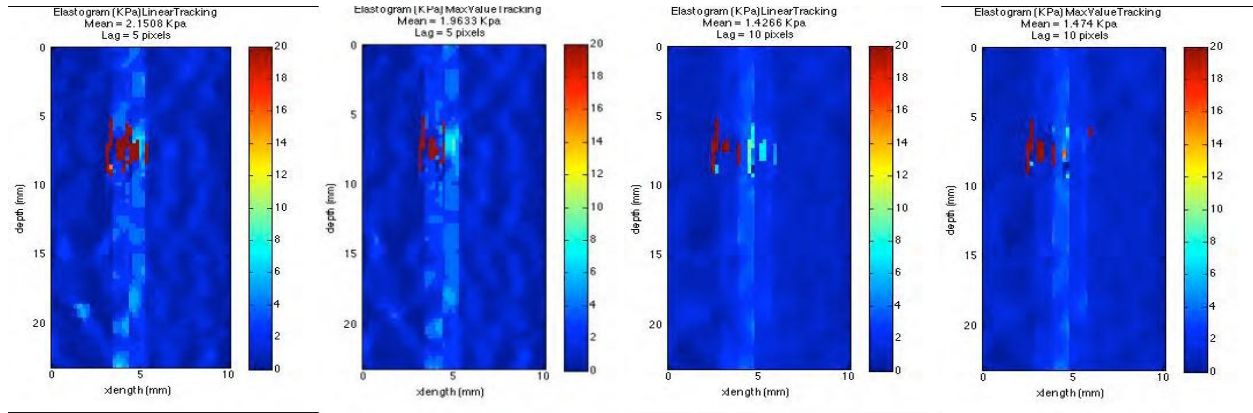


Figure 19: Elastograph generated by SW tracking of data exported from SSI in fig.18 ROI using different methods. [Left] LINEAR tracking + 5 frame lag [Middle Left] MAXVALUE tracking + 5 frame lag [Middle Right] LINEAR tracking + 10 frame lag [Right] MAXVALUE tracking + 10 frame lag

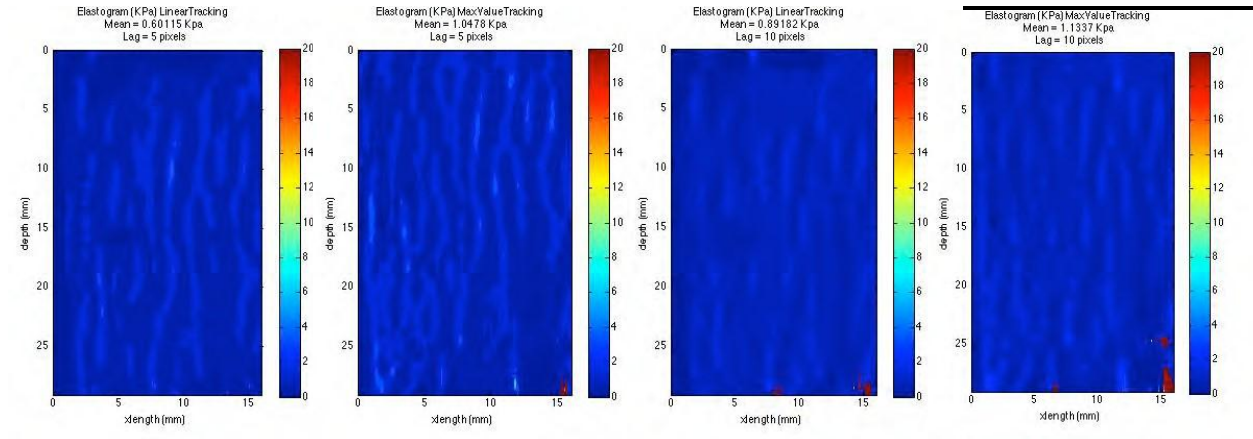
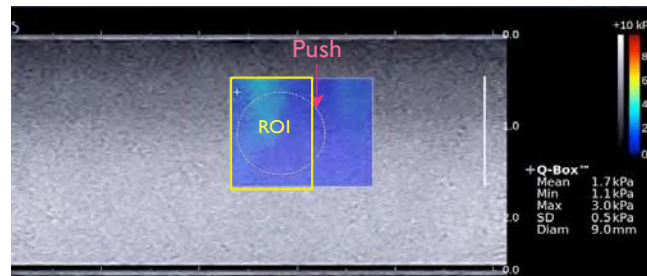


Figure 20: 2% alginate elastograph generated by SW tracking of data exported from VUE in fig.18 ROI using different methods. [Left] LINEAR tracking + 5 frame lag [Middle Left] MAXVALUE tracking + 5 frame lag [Middle Right] LINEAR tracking + 10 frame lag [Right] MAXVALUE tracking + 10 frame lag

According to the result, $k = 10$ frame lag became preferred to 5 because it gave more homogeneous and consistent results in alginate. However, in order to increase spatial and temporal resolution of tracking, $k = 8$ frame lag, which had comparable results to that of $k = 10$, was chosen.



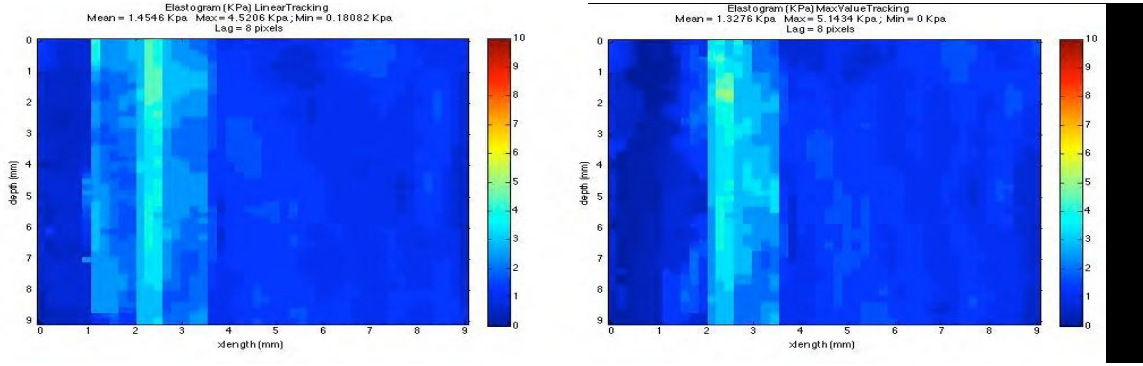


Figure 21: [Top] SSI elastograph of ROI in 2% alginate. [Bottom] Alginate elastograph generated by SW tracking of data exported from SSI in ROI using [Left] LINEAR tracking + 8 frame lag [Right] MAXVALUE tracking + 8 frame lag

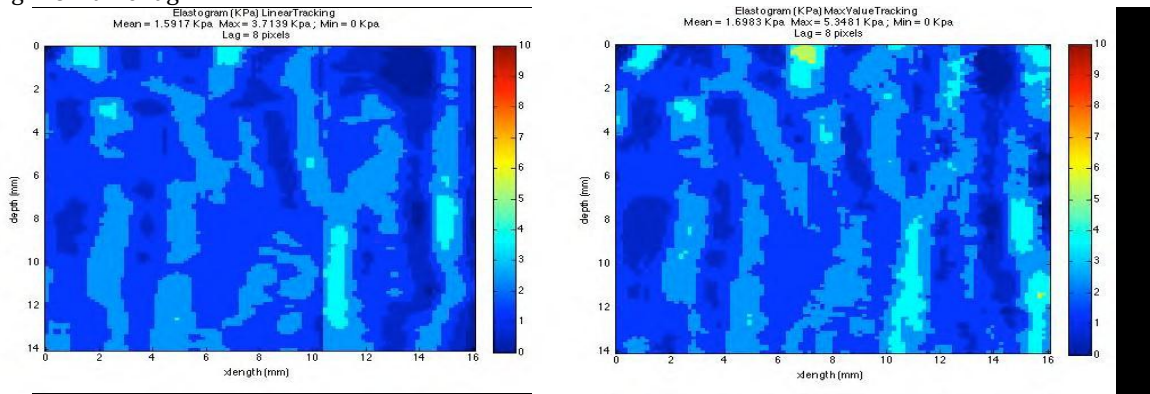


Figure 22: 2% alginate elastograph generated by SW tracking of data exported from VUE in same ROI using [Left] LINEAR tracking + 8 frame lag [Right] using MAXVALUE tracking + 8 frame lag

Statistical analysis was conducted on a total of 12 elastographs collected from 3 different 2% alginate using VUE, and compared to SSI results to determine the accuracy of the two tracking methods. Max value tracking method was chosen accordingly.

Table 2: Statistical results of mean shear modulus difference between VUE and SSI and standard deviation of VUE using max value and linear tracking methods.

2% Alginate	Mean (% diff)	STDEV
Max	5.02%	1.0449
Linear	8.1%	0.9270

Moving on, more optimizations were applied to SW tracking algorithm. Weighted average and interpolation of cross correlation functions were encoded to increase shear modulus accuracy and give rise to even higher spatial resolution.

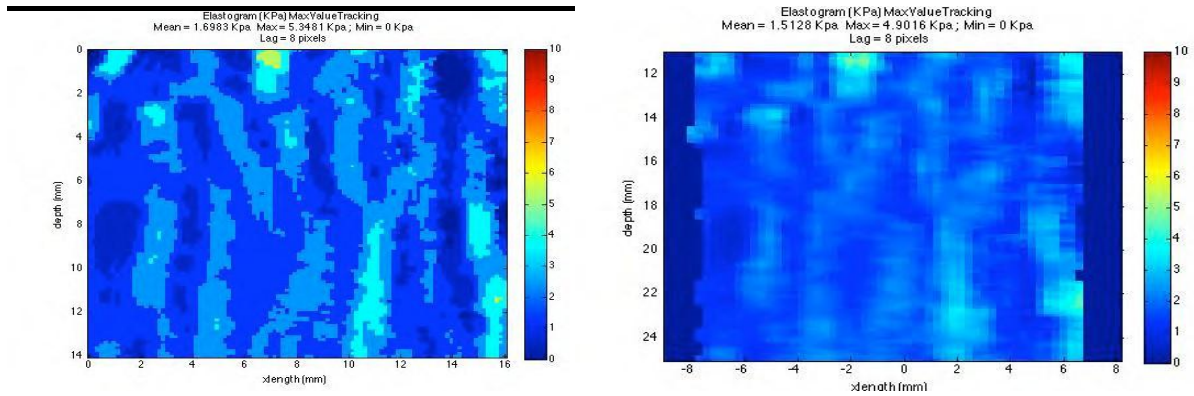


Figure 23: 2% alginate elastograph generated using data from VUE. [Left] Without averaging or interpolation [Right] With averaging and interpolation

Rat Brain Elastograph:

After optimizing alginate elastograph, control and TBI rat brains submerged in 2% alginate were studied in winter 2013. However, the result made no sense: SW became a mess when hitting the brain and the elastograph displayed unreasonably high or low stiffness in and around brain.

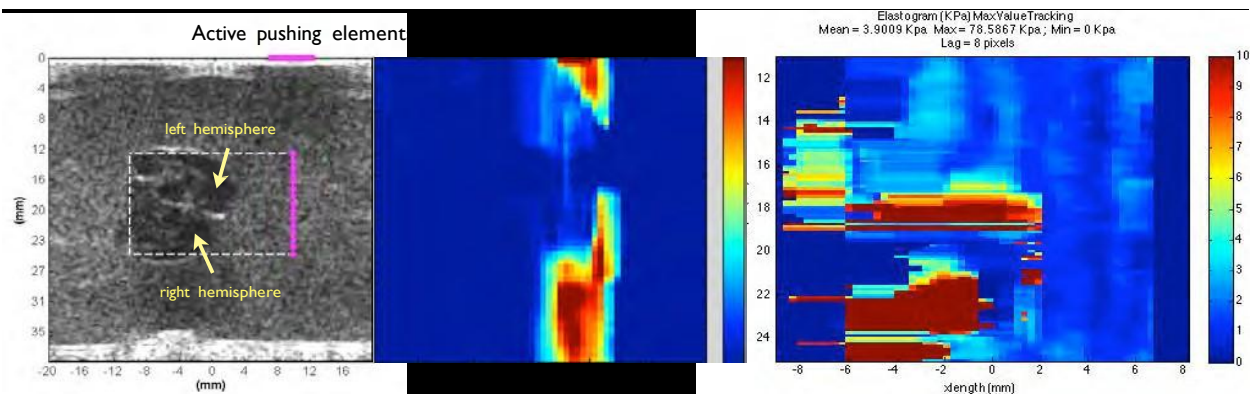


Figure 24: [Right] Control rat brain submerged in 2% alginate in VUE's B-mode ultrasound image. The box indicates ROI. Ultrasound "push" locates at the red dotted line. [Middle] Static SW movie from VUE when SW encounters the brain-alginate interface [Left] Brain elastograph generated using data from VUE.

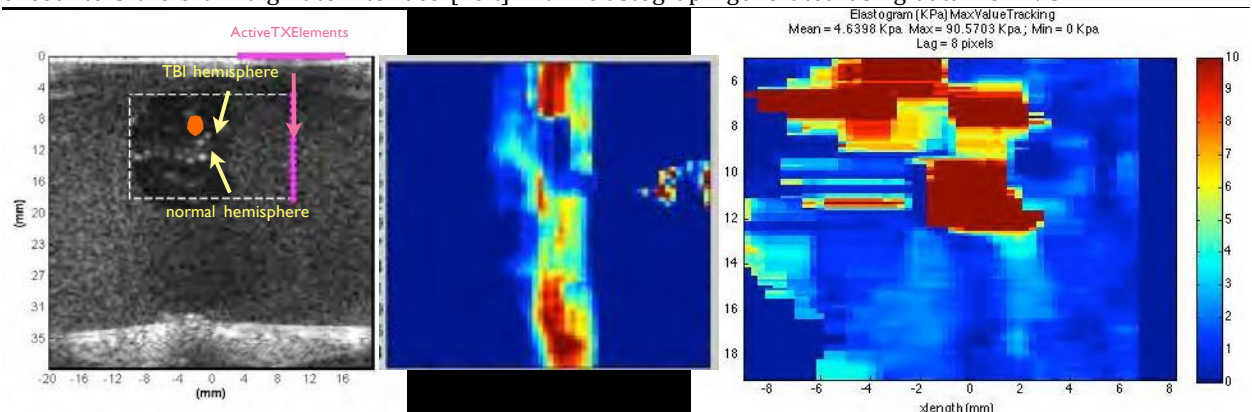


Figure 25: [Right] TBI rat brain submerged in 2% alginate in VUE's B-mode ultrasound image. The box indicates ROI. Ultrasound "push" locates at the red dotted line. [Middle] Static SW movie from VUE when SW encounters the brain-alginate interface [Left] Brain elastograph generated using data from VUE.

Mouse Brain Elastograph:

Because SW tracking algorithm was working very well in alginate, the hypothesis for such messiness in brain---alginate interface is that SW impedance of 2% alginate and brain does not match. According to literature, MRE was used to measure SW velocity in human brains. The value was used in this study to represent that in mouse brains. Measurements of SW impedance were conducted in different percentages of alginates in order to match that of brain. Recall that SW impedance equals to density * SW velocity in the medium. Mouse brains were used in the study.

Table 3: The measured SW impedance of 3.3% to 6% alginate. SW did not appear in 5.5% and 6% alginate. According to the table, 5.3% alginate has the closest SW impedance to mice brain assuming the literature measurement on human brain is correct.

Alginate (%)	G (kPa)	Density (kg/m ³)	Velocity (m/s)		Density	Velocity	Impedance
3.3	1.9113	1034	0.828571163				
	2.0872	999	0.865859483				
	1.8357	1056	0.812019088	AVG =	1029.66667	0.83548324	860.269248
3.7	3.3025	999	1.089147748				
	3.569	1004	1.13224043				
	2.958	1032	1.030776406	AVG =	1011.66667	1.08405486	1096.70217
4	4.5467		1.277949035				
	4.3034	1005	1.24328657	AVG =	1005	1.2331897	1239.35565
	3.8655		1.178333496				
5	7.5571		1.647566562				
	6.5148	1007	1.529734031	AVG =	1007	1.53275983	1543.48915
	5.6214		1.4209789				
5.3	9.5839	1032	1.855395596				
	8.3632	1025	1.733211755	AVG =	1029.66667	1.68008211	1729.92455
	5.8666	1032	1.451638986				
5.5	NA			Brain	1100	1.88	2068
6	NA						

Referring to table 3, SW imaging was conducted in 4.4%, 4.5%, 4.6% and 4.7% control brain---alginate molds. Meanwhile, 5 different combinations of ultrasound push parameters (recall from figure 16) were chosen for SW movies collection. Figures below show the elastograph of 4.4% and 4.7% alginates with brain.

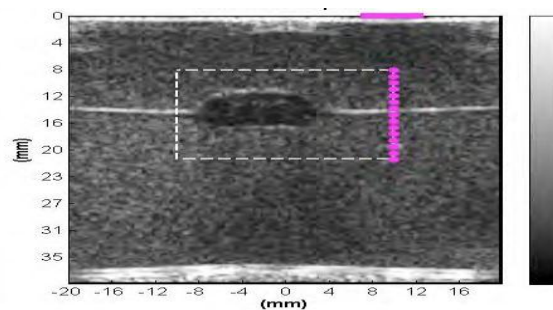


Figure 26: B-mode image of control mouse brain submerged in 4.4% alginate.

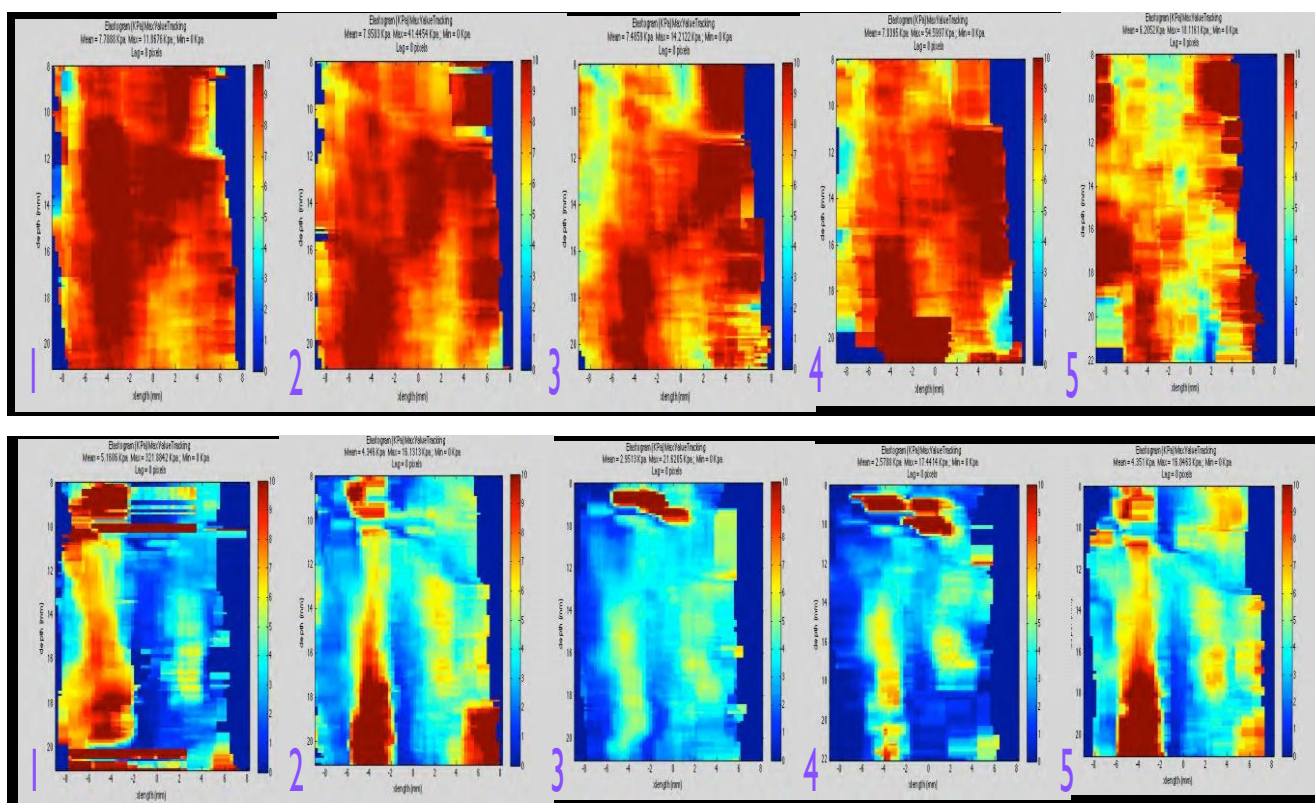


Figure 27: Shear modulus maps using 1-5 push parameters of [Top] 4.4% alginate alone and [Bottom] Control mouse brain in 4.4% alginate.

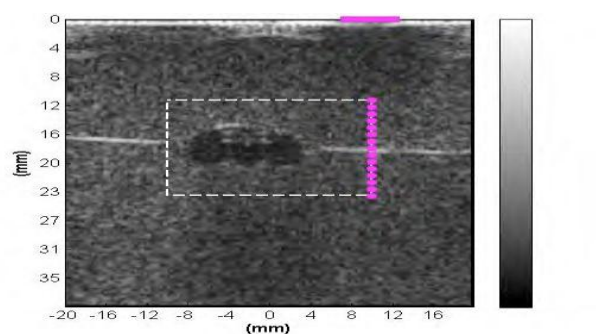
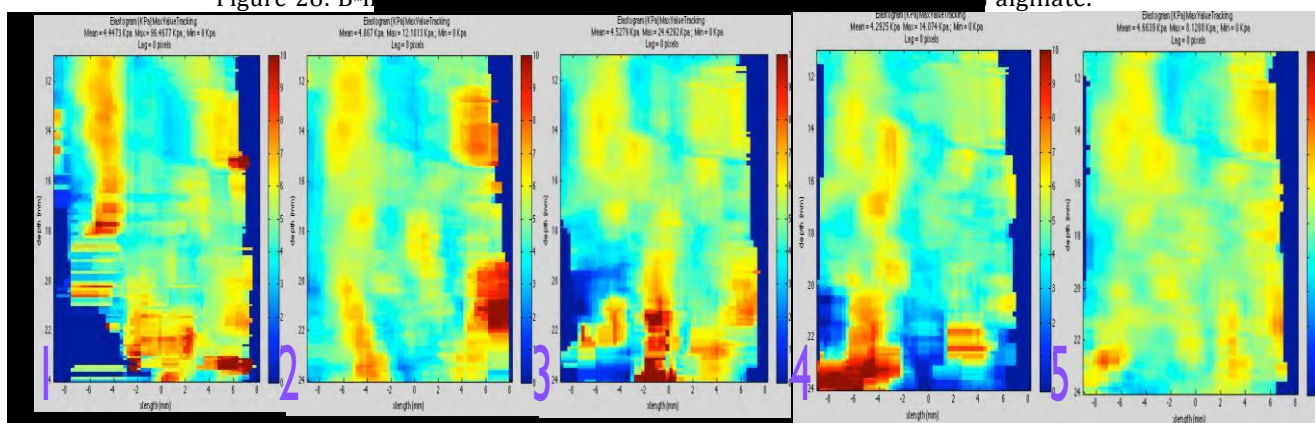


Figure 28: B-mode image of a tissue sample in 4.4% alginate.



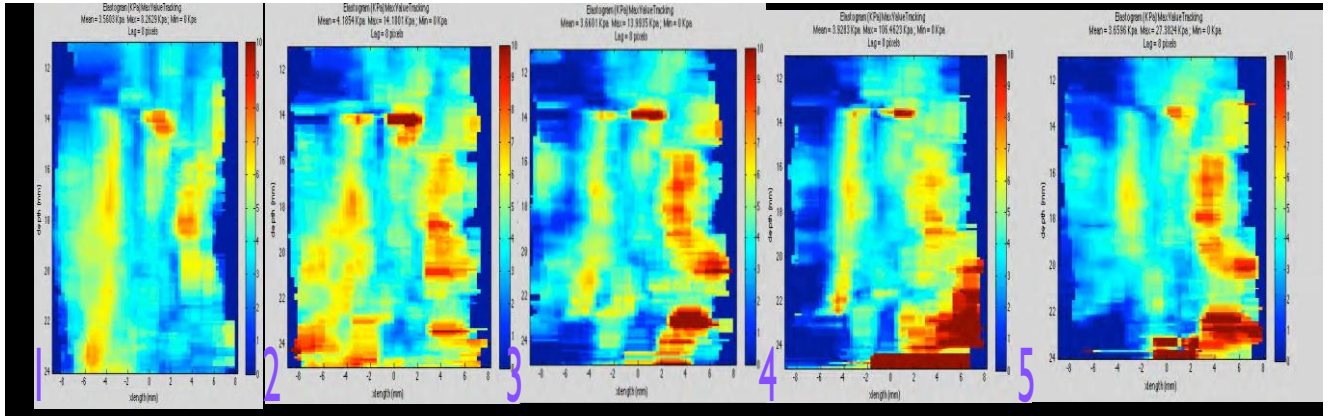


Figure 29: Shear modulus maps using 1-5 push parameters of [Top] 4.7% alginate alone and [Bottom] **Control mouse brain** in 4.7% alginate

Regarding to the result above, 4.7% alginate was chosen to be the most optimized percentage for mouse brains. Push parameter number 5 was considered best for 4.7% alginate SW imaging. Therefore, one additional experiment with the chosen setup was carried out in alginate to test parameter 5, and SW propagation movies in brain were studied to reconfirm the results.

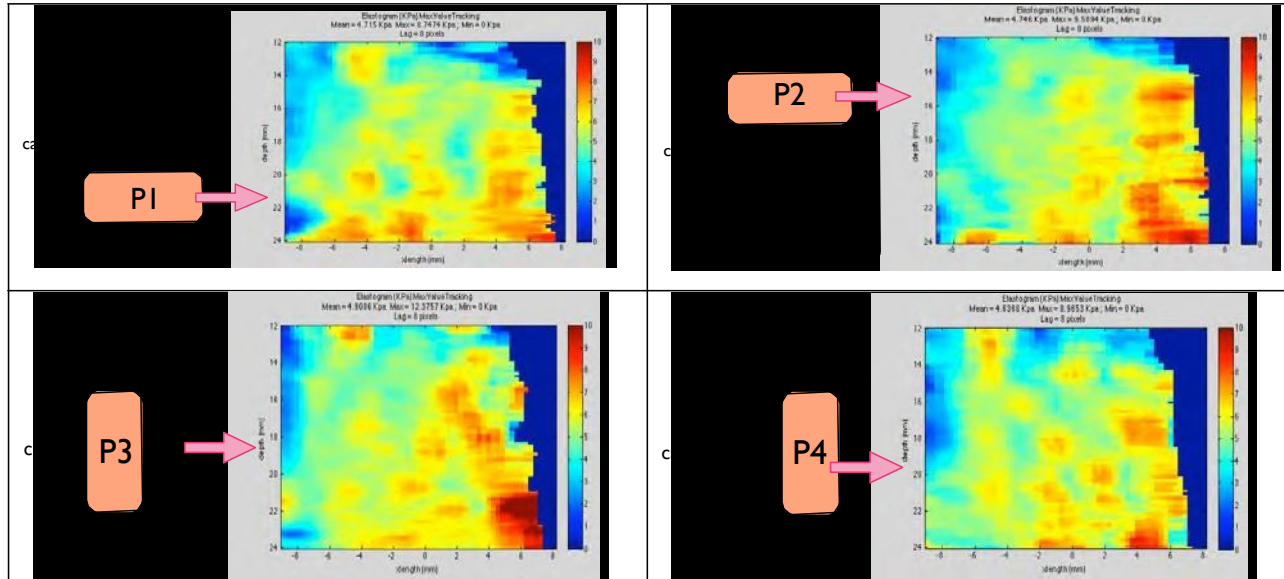


Figure 30: Shear modulus maps of 4.7% alginate using #5 push parameter at four different positions.

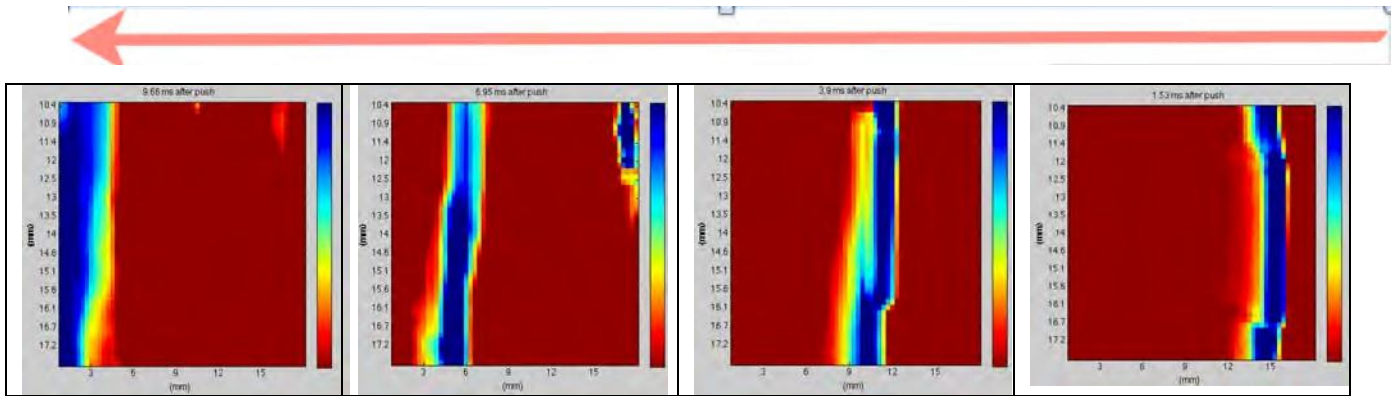


Figure 31: SW propagation movie of control mice in 4.7% alginate

Starting spring 2013, a total of 5 control mice and 5 24---hour TBI mice were imaged in vitro using the chosen alginate. The imaging protocol was modified in that each brain will be imaged between 20---30min after exposure and at four positions, using various push parameters. The positions were indicated below in a chronic order. Expectations were that SW imaging would be able to highlight TBI site with lower shear modulus. An example of each is shown below.

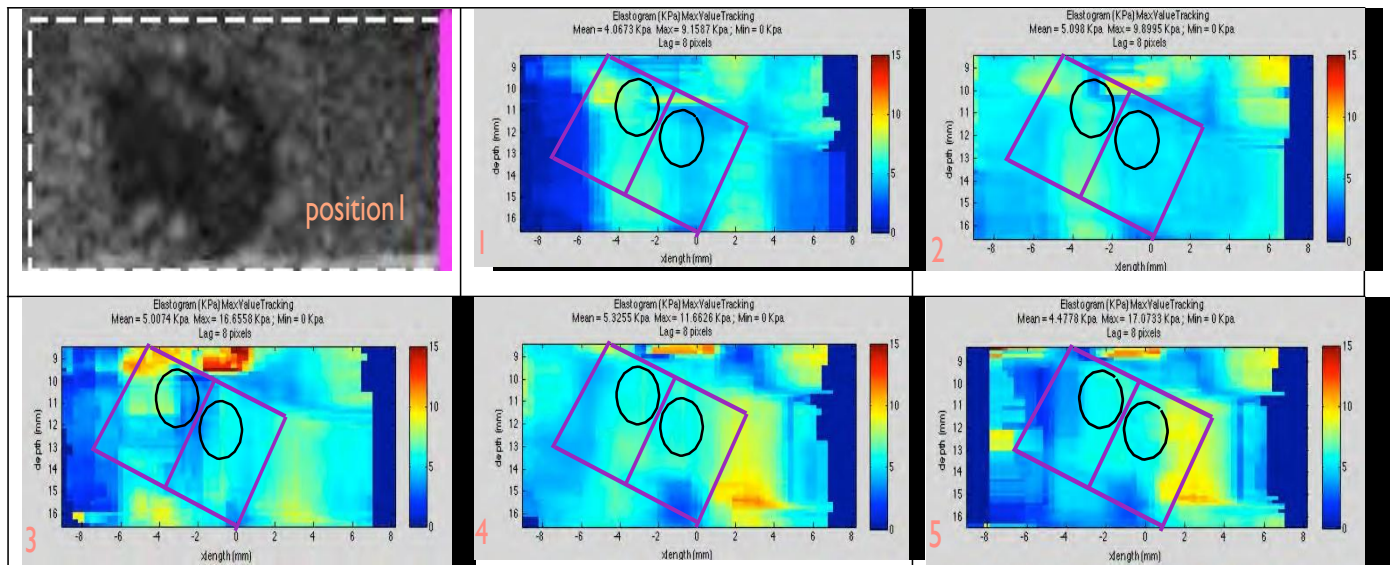
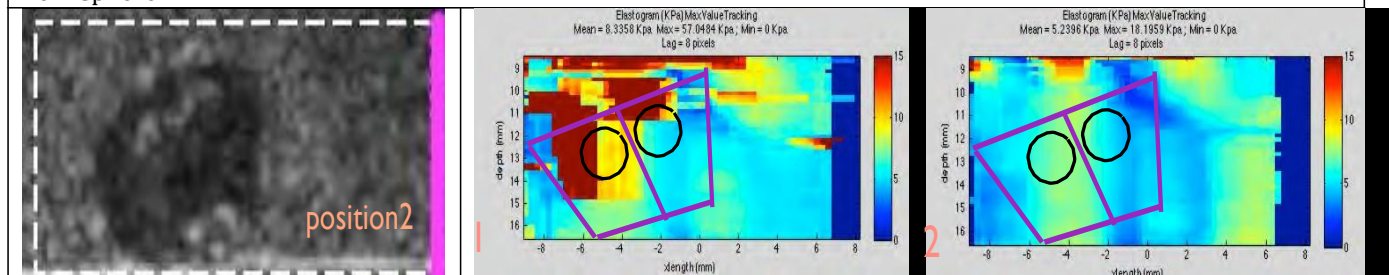


Figure 32: [Top Right] B-mode Image of **Control mouse brain** in position1. [Others] Shear modulus map of control mouse brain in 4.7% alginate in position 1 with 5 parameters. Boxes contours the brain, circles indicates the two hemisphere.



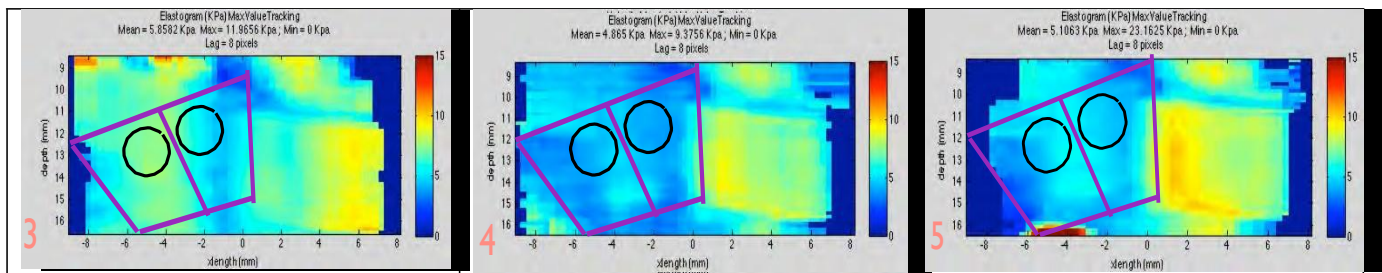


Figure 33: [Top Right] B-mode Image of **Control mouse brain** in position2. [Others] Shear modulus map of control mouse brain in 4.7% alginate in position 2 with 5 parameters

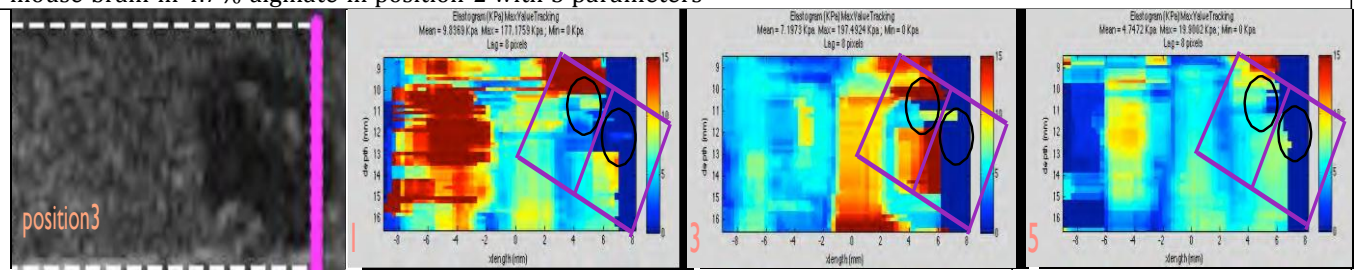


Figure 34: [Top Right] B-mode Image of **Control mouse brain** in position3. [Others] Shear modulus map of control mouse brain in 4.7% alginate with parameter 1, 3, 5 in Position 3

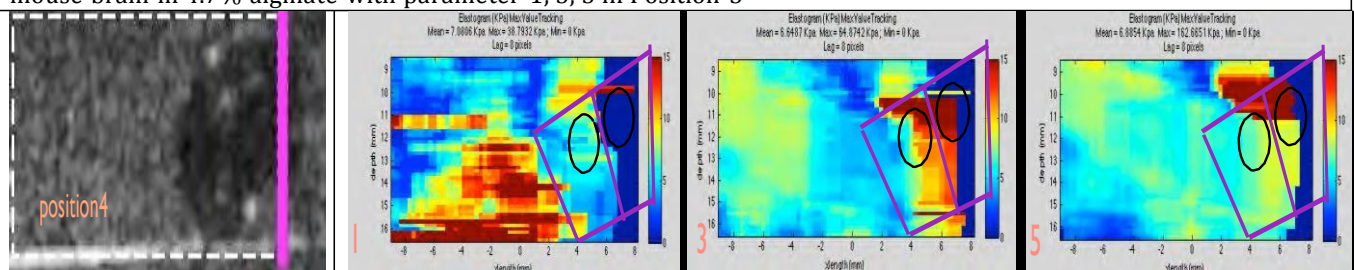


Figure 35: [Top Right] B-mode Image of **Control mouse brain** in position4. [Others] Shear modulus map of control mouse brain in 4.7% alginate with parameter 1, 3, 5 in Position 4

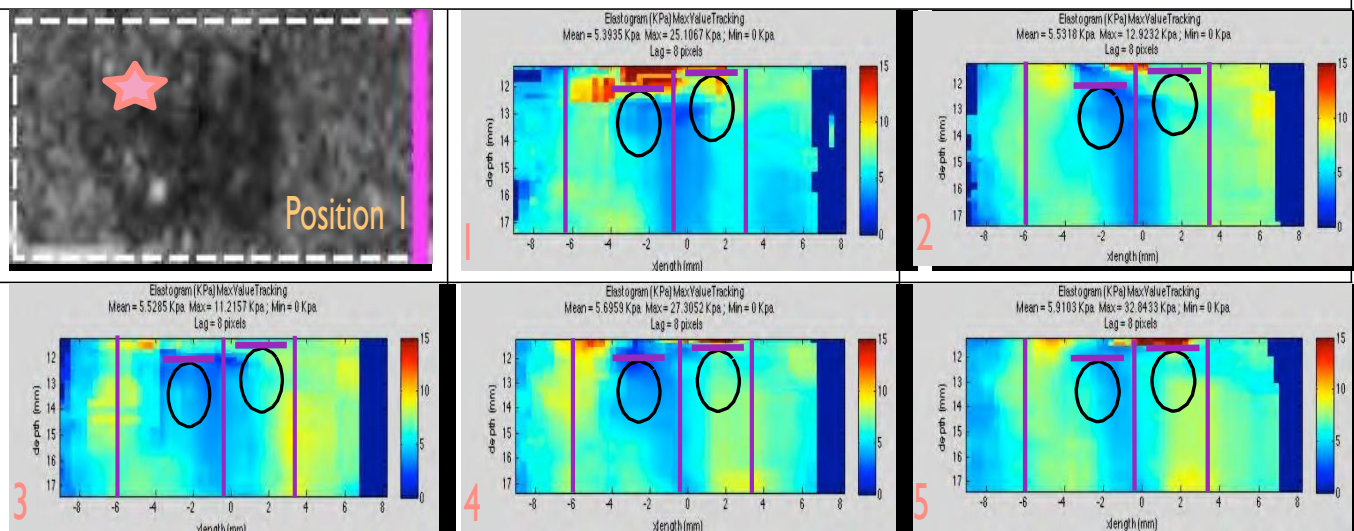


Figure 36: [Top Right] B-mode Image of **TBI mouse brain** in position1. [Others] Shear modulus map of 24hr TBI mouse brain in 4.7% alginate in position 1 with 5 parameters. Boxes contours the brain, circles indicates the two hemisphere.

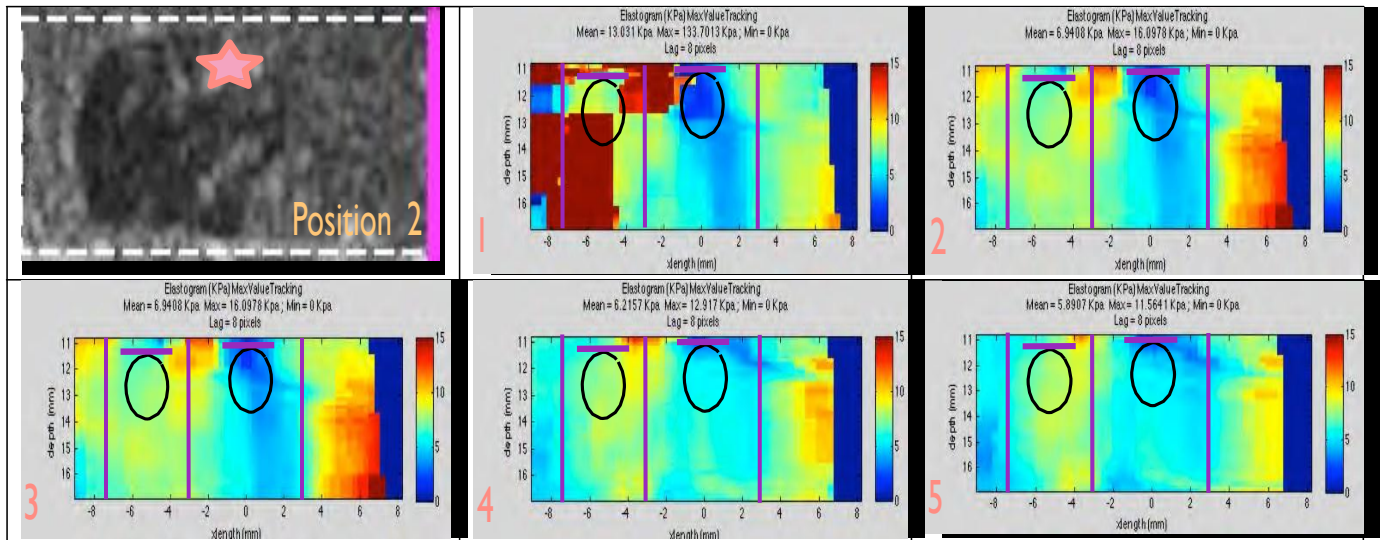


Figure 37: [Top Right] B-mode Image of **TBI mouse brain** in position2. [Others] Shear modulus map of 24hr TBI mouse brain in 4.7% alginate in position 2 with 5 parameters

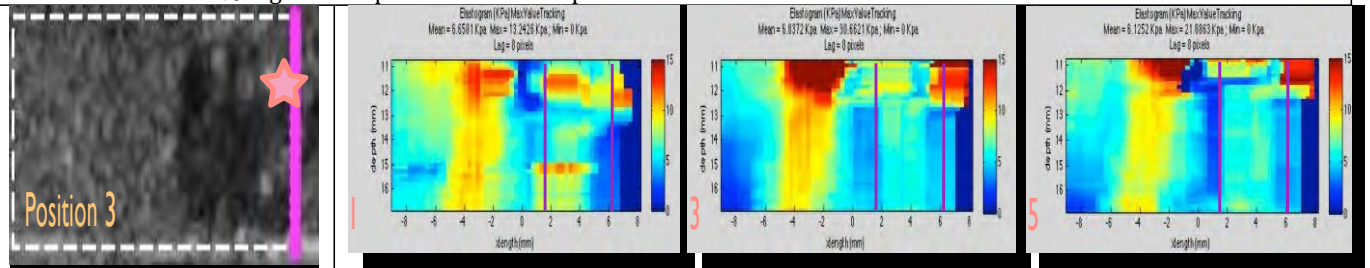


Figure 38: [Top Right] B-mode Image of **TBI mouse brain** in position3. [Others] Shear modulus map of 24hr TBI mouse brain in 4.7% alginate with parameter 1, 3, 5 in position 3, purple lines indicate edge of normal hemisphere.

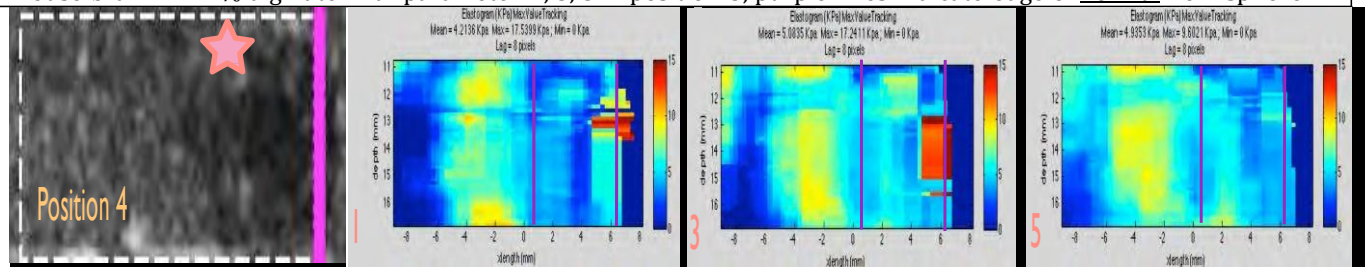


Figure 39: [Top Right] B-mode Image of **TBI mouse brain** in position4. [Others] Shear modulus map of 24hr TBI mouse brain in 4.7% alginate with parameter 1, 3, 5 in position 4, purple lines indicate edge of **TBI** hemisphere

According to the qualitative analysis in 5 control and TBI mice, position 1 and 2, and parameter 4 and 5 turned out to have equal brain image quality. Consequently, quantitative analyses of these images were carried out to determine the sensitivity of the parameters to TBI. The circled regions, indicating the two hemispheres, were evaluated for mean shear modulus and compared to each other. Position 1 and position 2 were analyzed separately at first to study the effects of time variance (due to imaging order: 10---15 minutes difference) and position of hemisphere (near or far from the ‘push’).

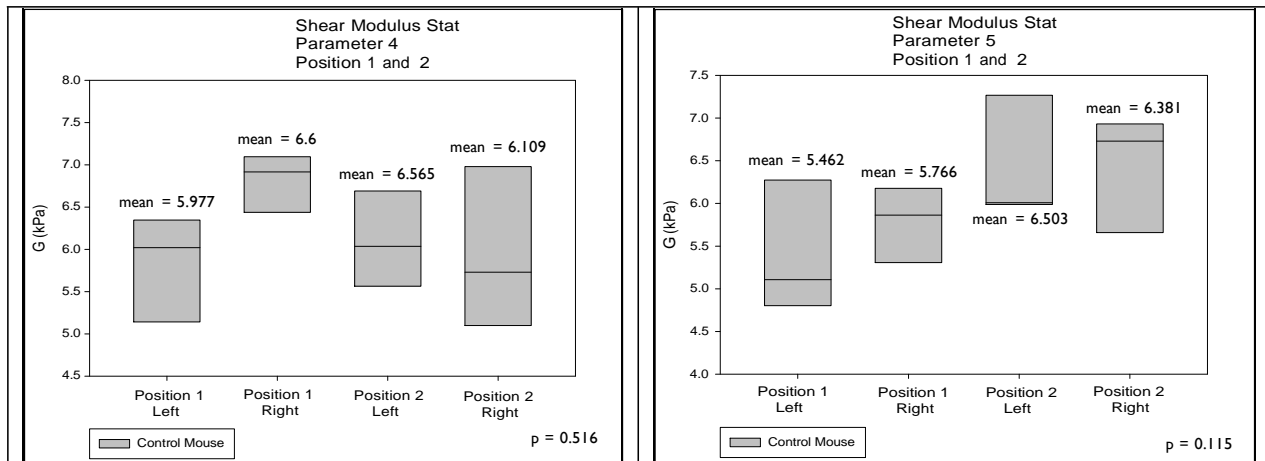


Figure 40: Statistical analysis (parameter 4 and 5) of shear-modulus in the two hemispheres of control mouse brains at position 1 and position 2. Box plots show mean, distribution and p values of shear modulus values in left and right hemispheres.

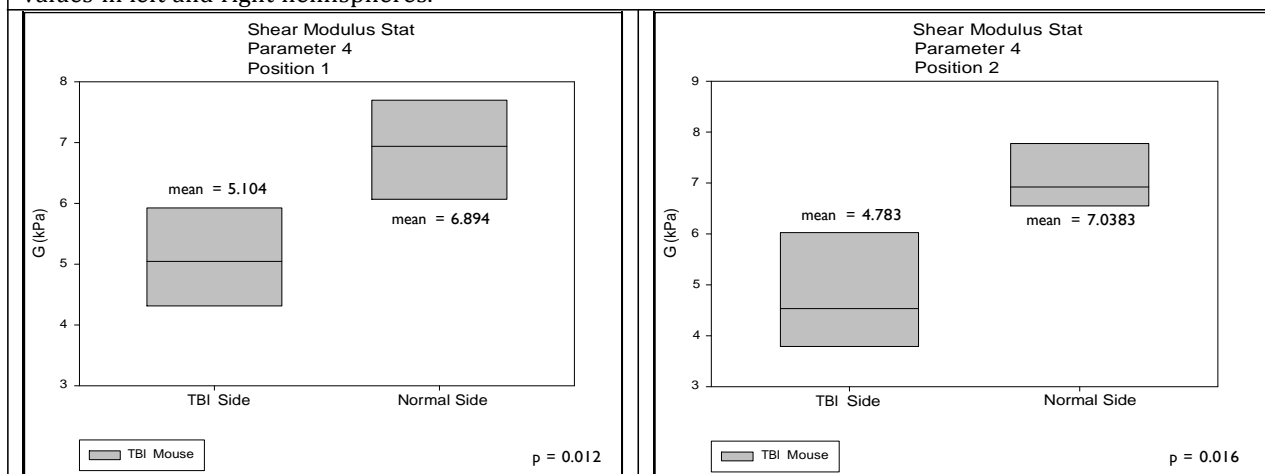


Figure 41: Statistical analysis (parameter 4) of shear-modulus in the two hemispheres of TBI mouse brains [Left] position 1 and [Right] position 2.

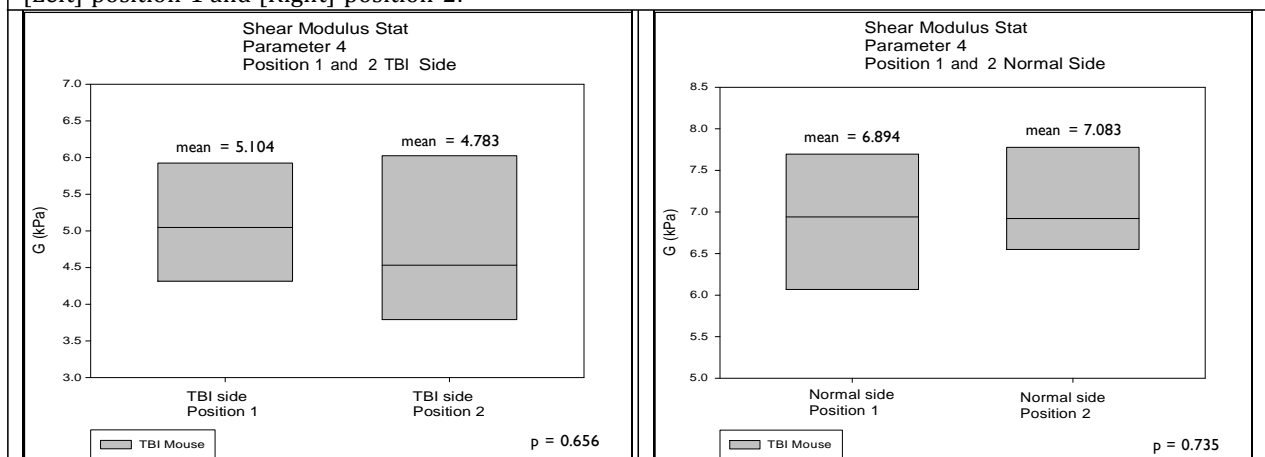


Figure 42: Statistical analysis (parameter 4) of shear-modulus in the two hemispheres of TBI mouse brains [Left] Position 1 and position 2 TBI side [Right] Position 1 and position 2 normal side

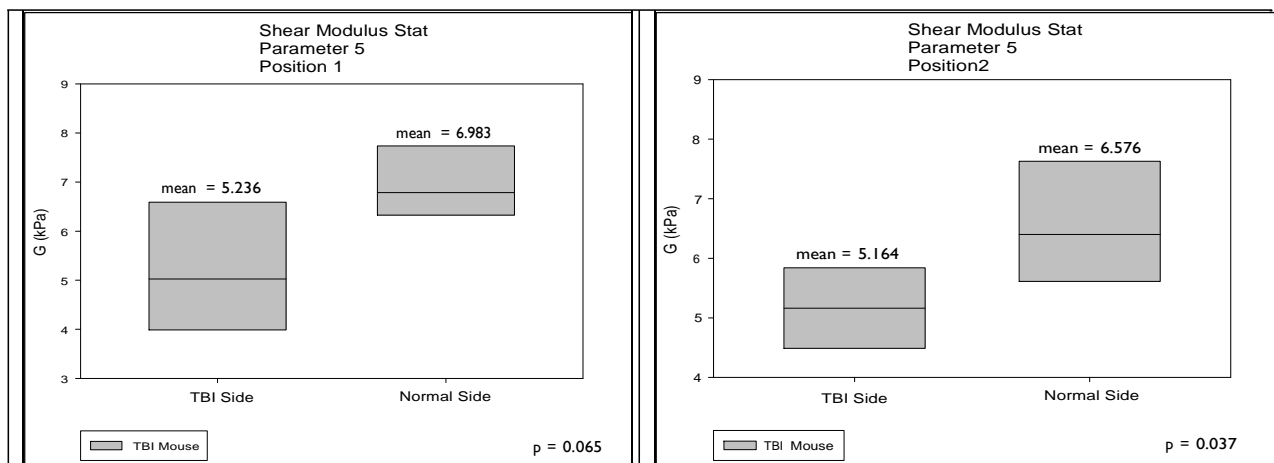


Figure 43: Statistical analysis (parameter 5) of shear-modulus in the two hemispheres of TBI mouse brains [Left] position 1 and [Right] position 2

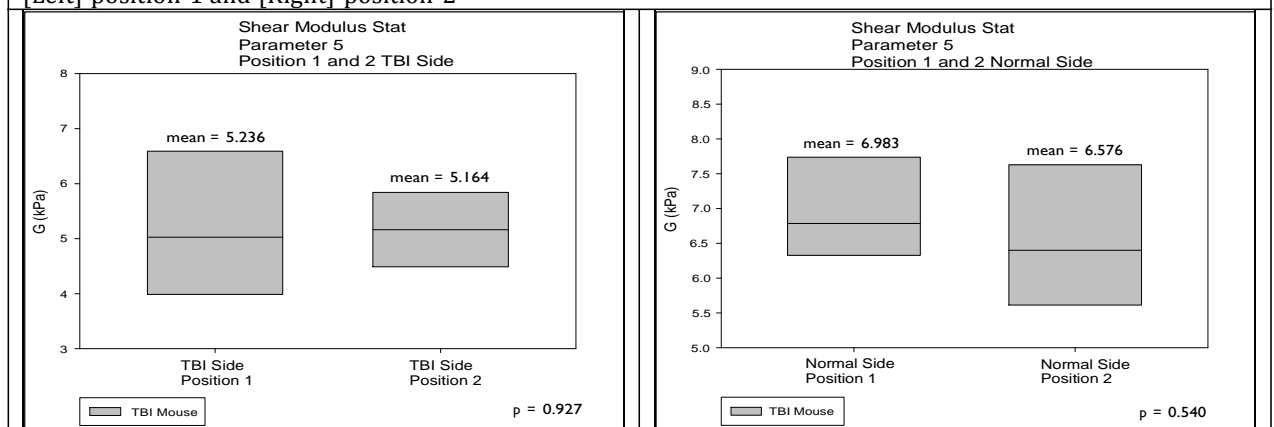


Figure 44: Statistical analysis (parameter 5) of shear-modulus in the two hemispheres of TBI mouse brains [Left] Position 1 and position 2 TBI side [Right] Position 1 and position 2 normal side

After confirming that time variance of imaging and the position of hemisphere relative the 'push' have no significant effect on the stiffness of brain tissue, further analysis was conducted combing the data from position 1 and position 2.

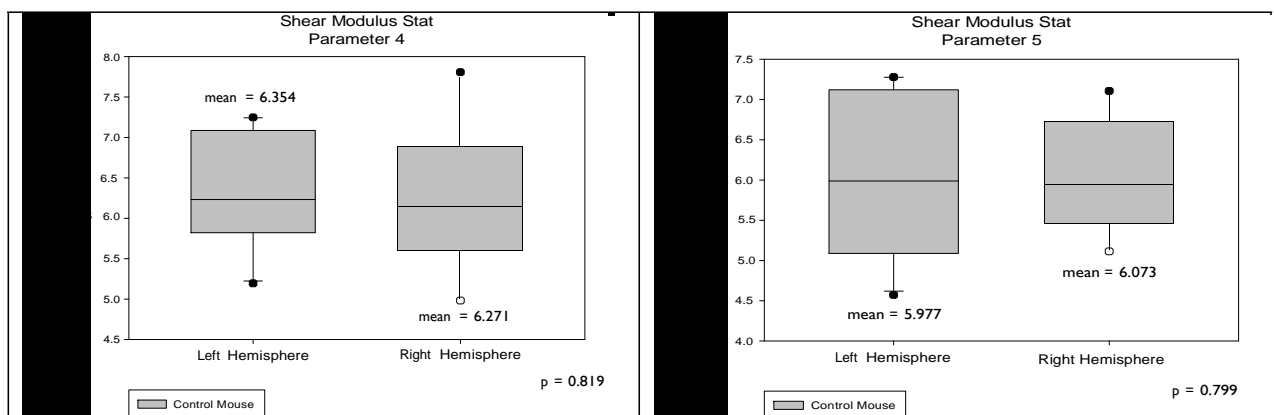


Figure 45: Statistics results (parameter 4 and 5) of shear modulus in the two hemispheres of control mouse brains.

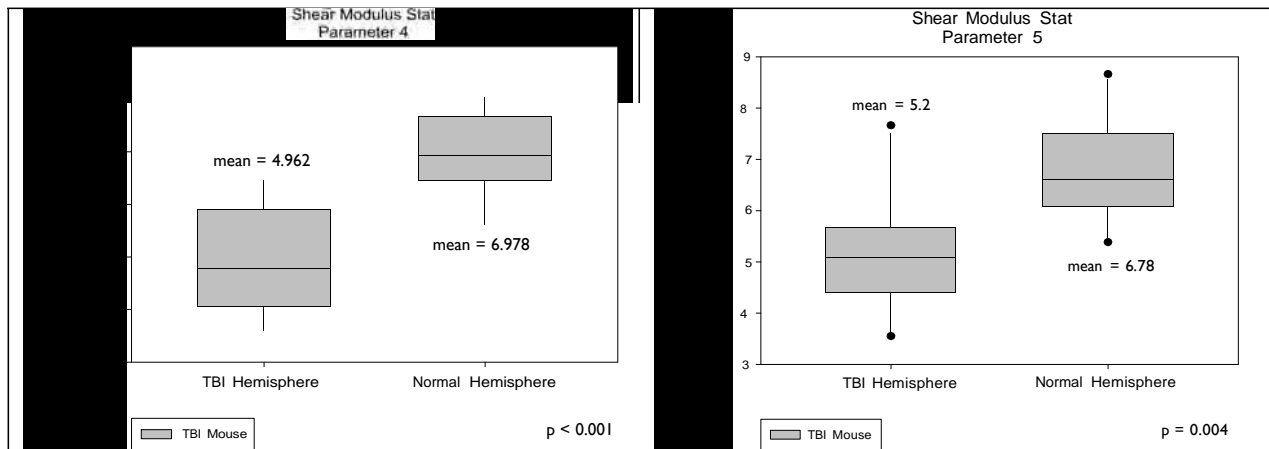


Figure 46: Statistics results (parameter 4 and 5) of shear modulus in the two hemispheres of TBI mouse brains.

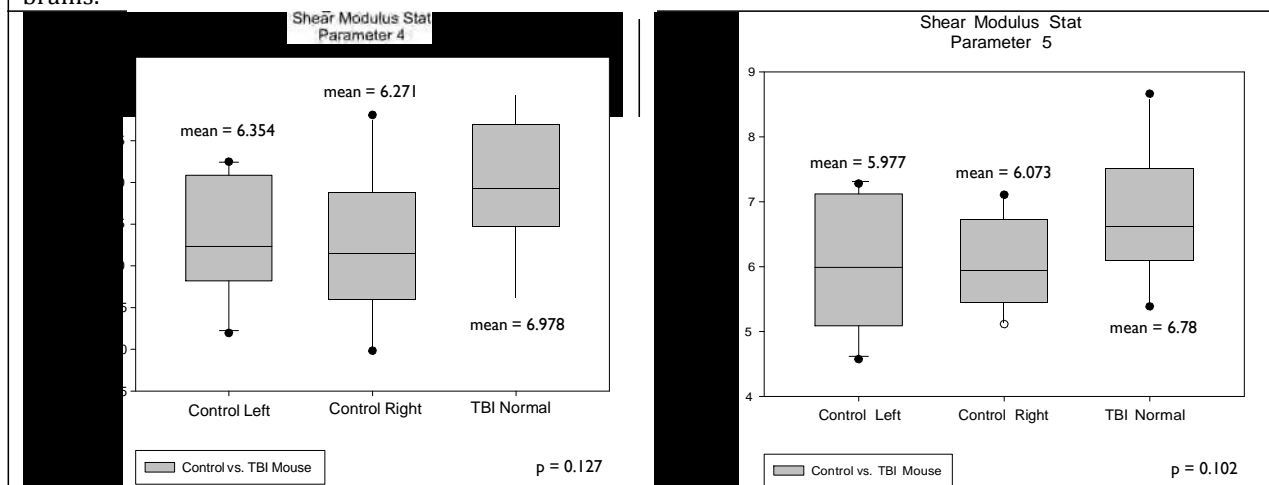


Figure 47: Statistics results (parameter 4 and 5) of shear modulus in the two hemispheres of Control mouse and the Normal hemisphere of the TBI mouse.

Design Decision:

In the computation part of the project, I was responsible to design, test, and optimize SW tracking algorithm. I designed the tracking pattern, two separate tracking methods and the approach to manipulate SW data in space and time to give the best shear modulus image. I decided to do weighted average and designed the cross correlation interpolation.

In the experiment part of the project, I was responsible to perform surgeries to rodents, set up imaging protocols, and design an alginate setup for brain to sit in. I decided to work on different percentage of alginates as an approach to optimize SW imaging. I decided to test alginate percentage ranging from 4.4% to 5%. I designed a two-layer alginate setup that could cover up the brain with the correct orientation.

In the analysis part of the project, I was responsible to post-process SW data exported from both SSI and VUE, study the resulting shear modulus map, and give further modification or conclusion. I decided to compare mean, standard deviation, max and min values in alginate stiffness maps from VUE and SSI. I decided to contour the brain and its hemispheres in stiffness maps for easy visualization. Additionally, I decided to do quantitative analysis along with qualitative analysis in TBI and non-TBI hemispheres so as to determine the most sensitive parameter for diagnosis of TBI.

Analysis and Conclusions:

Breast phantom and Alginate Studies:

According to fig.17, the shear moduli in the two images in the same color scale are close in the bottom half. However, the generated image has very low spatial and temporal resolution, and inconsistent values on the top. This result proves the correctness of the preliminary SW tracking algorithm, and also indicates future work in the direction to increase resolution. In fig.18 and fig.19, temporal resolution of the generated shear modulus maps in alginate is significantly increased by the modified SW tracking pattern (recall in section Correlation Methodology). Images with frame lag equals to 10 are more homogenous and have mean G value much closer to that of SSI (fig.18 top) than images with frame lag equals to 5. There are still artifacts existing in the images using SSI data, indicated by the bright red pattern, but the MaxValue Tracking method results in fewer artifacts than Linear Tracking method (fig.18 bottom). Images generated from VUE have a lower average G value (fig.19), but there is no artifact present. This is mostly because VUE only generates one push into the medium, while SSI generates 4 pushes at different positions into the medium. Therefore, artifacts from SSI are very likely due to SW interference between different pushes. In fig.20 and fig.21, images generated using frame lag 8 have comparable homogeneity as frame lag 10, but higher temporal resolution, and therefore was chosen to be the standard lag used in further studies. Note in fig.20 bottom that images generated using SSI data have same bright patterns as appeared in SSI images on the top. VUE images have average G values much closer to that from SSI (fig.21), and the MaxValue Tracking continues to have better image quality and mean shear modulus. According to the statistical analysis in table 1, MaxValue method appears to work 3%

better comparing to Linear Tracking method, and the standard deviation of the two tracking algorithm do not differ significantly. Consequently, MaxValue tracking method is applied in later experiments. In fig.22, both images have very close mean shear modulus value. However the right image has less stripy patterns and higher resolution comparing to the left image. This implies that the cross correlation interpolation and weighted spatial averaging are working very well in optimizing the elastograph.

Rat Brain Elastograph:

According to fig.23, a control rat brain is sitting vertically in 2% alginate in B-mode image. From the static SW propagation image (middle), it is very obvious that when SW reaches the brain-alginate interface, it breaks up and disappears in the brain. This gives rise to the messy shear modulus map (right), which has large non-traceable area on the left side and unreasonable max G value equals to 78.6kPa in brain. Nonetheless, the shear modulus looks nice and homogenous in alginate on the right. Same phenomenon is observed in fig.24 on a 24-hour TBI brain. The shear modulus map on the right contours the brain edge, but fails to give reasonable stiffness values inside the brain. Therefore, one possible conclusion is that when SW is propagating from alginate to brain, the media difference causes SW to break apart, dissipate and finally disappear. This discrepancy can be reduced if the SW impedance of alginate equals to that of brain. Another possible reason can be due to the white matter in rat brains. By looking at SW propagation movie in rats, SW tends to break apart or disappear at the white matter because the structure is much stiffer than grey matter. Though this phenomena is not observed in mice study (shown below), it is very likely that the larger white matter structures in rats disturb SW more significantly so that the filtering and averaging algorithm, which works on mice, are not sufficient to solve the discrepancy in rats.

Mouse Brain Elastograph:

According to table 2, human brain SW impedance, referring to Weaver et.al¹⁸, is closest to that of 5.3% alginate. For alginates larger than 5.3% (i.e. 5.5% and 6%), the mechanical property of them is too hard for the ultrasound pushes to induce detectable displacements. Consequently, 5.3% alginate becomes the top limit.

In fig.27, 4.4% alginate images are homogenous throughout the five parameters, however the mean shear moduli of which are relatively high (~ 7 kPa) compared to greater

percentage of alginates (i.e. 4.7% in fig.29). This is because alginate becomes harder through time, and for this particular set of imaging, the alginate was settled longer than the other ones. According to this finding, later alginate imaging were all controlled to occur in the same time frame (30---40 min). Reasonable shear modulus values in brain indicate that SW successfully propagates through the brain from alginate. Nonetheless, brain images still appear to have unexpected artifacts, elastograph from parameter 1 is especially messy. This result implies that the SW impedance of alginate and brain gets closer, but there is still space to improve. In fig.29, 4.7% alginate images are very homogeneous, especially parameter 5. Brain elastograph appear to have tiny spots of artifacts near the top of the brain. One possible reason for the artifacts is SW being disturbed when propagating through white matter, which is a lot stiffer than grey matter. Other than that, the elastograph shows reasonable brain shear modulus, the brain seems invisible in alginate and there is no obvious inter---hemisphere difference, which is expected. Consequently, conclusions were drawn from observation that parameter 5 is the best for 4.7% alginate and 4.7% alginate is the best for SW imaging in brain.

In fig.30, 4.7% alginate is reproduced using push parameter 5 at four different positions. According to the elastograph, the images are consistently homogeneous with a steady mean G value of ~ 4.7 kPa. Same analysis and results were observed in another 4.7% alginate. In fig.31, static SW propagation movie in 4.7% alginate---brain medium are shown. Recall that fig.3 shows the static SW propagation movie in alginate. Comparing the two propagations, and the ones in rats (fig.23 and fig.24 middle), SW in mouse brains is totally traceable and propagates more like in alginate as SW does not break up or get messy. Note that the bottom part of wave front does tilt a little bit as SW propagates because of the brain in the medium.

Fig.32 shows shear modulus images of a control mouse brain in position 1 using 5 parameters. According to observation, the two hemispheres have slight difference in parameter 1, 2, and 3. In parameter 4 and 5, no difference can be noticed between two hemispheres. In position 2 (fig.33), parameter 1 results in huge artifacts within the brain but parameter 4 and 5 show close shear modulus in both hemispheres. In position 3 and 4 (fig.34 and fig.35), there are artifacts existing in all of the images in the brain, and there is discontinuity of shear modulus. This results primarily from the messiness of SW

propagation, which is caused by the ultrasound pushes generated into the brain instead of alginate. Notice in images of parameter 3 and 5, the elastograph becomes smooth and homogeneous again out of the brain. Same imaging protocol and qualitative analysis were conducted in 4 more control mouse.

Fig.36 shows shear modulus images of a TBI mouse brain in position 1 using 5 parameters. According to observation, the TBI sides in all parameters are shown to have lower elasticity than the normal side. However, in parameter 1 and 2, the center of brain is also shown to be low in stiffness. Parameter 3, 4 and 5 turn out to have more localized low stiffness region corresponding to the TBI side. In position 2 (fig.37), parameter 1 again results in huge artifacts within the brain, while parameter 2 to 5 all show localized reduced elasticity at the TBI side. In position 3 and 4 (fig.38 and fig.39), artifacts again come up in the elastograph. However, if comparing the brain region in the fig.38 and fig.39, there is still an observable difference in the two hemispheres regardless of artifacts. Same imaging protocol and observational analysis were conducted in 4 more TBI mouse.

According to observation on 5 control and 5 TBI mice, position 1 and 2 are chosen for further analysis because position 3 and 4 are way too noisy. Parameter 1 and 2 tends to result in artifacts in the brain. Parameter 3 has much fewer artifacts but often displays inter---hemisphere difference in control brains and unfocused injury in TBI brains. Parameter 4 and 5 become most prominent in diagnosis of TBI because they work well on both control and TBI brains. One hypothesis for this is that parameter 4 and 5 have more active pushing elements and longer push duration, which induce larger and stronger tissue displacement, and enable SW to propagate smoothly without being dissipated or disturbed. Because it is hard to tell from eyes which parameter (4 or 5) is the most sensitive to TBI, quantitative analysis is needed.

Fig.40 [left] indicates that in control mouse brain, using parameter 4, no statistically significant difference is observed between position 1 and 2 in both contralateral and ipsilateral hemispheres ($p = 0.516$). This means that the time and position variance do not alter the brain property great enough for the elastograph to detect using parameter 4. Same result is reached using parameter 5 ($p = 0.115$) in fig.40 [right].

Fig. 41 compares the TBI and normal side of TBI brain at position 1 [left: $p = 0.012$] and position 2 [right: $p = 0.016$] separately using parameter 4. Both statistics show

significant decrease of shear modulus on the TBI side. Then, in fig.42, the TBI and normal side in both positions are not significantly different ($p = 0.656$ TBI; $p = 0.735$ normal). The result further affirms that the time and position variance do not affect the elastograph in parameter 4. Same statistical analysis on parameter 5 reaches the same conclusion except that there is no significant difference found in position 1 of the TBI brain ($p = 0.065$), though there is a great trend that they will be different according to fig.43. This may be an indication of insensitivity of parameter 5 to TBI, but may also be due to the small sample size ($n = 5$) involved in the study.

According to the result above, data from position 1 and position 2 of the same brain are combined and analyzed again. In fig.45, both parameter 4 and 5 indicate no inter-hemispherical difference in control brains. Parameter 4 has $p=0.819$, which is more slightly greater than $p=0.799$ in parameter 5. In fig.46, both parameter 4 and 5 indicate significantly lower stiffness in TBI side. Parameter 4 is the more sensitive ($p<0.001$), then parameter 5 ($p=0.004$). In fig.47, control hemispheres using parameter 4 and 5 are compared to the normal side of TBI brains. TBI normal sides in both parameters have a higher mean shear modulus than the controls, indicating a trend of increasing stiffness, however, the statistical analyses indicate no significant difference.

As a conclusion according to the results above, the designed SW tracking algorithm successfully track and produce elastograph of alginate and brain. Among the different methods developed, MaxValue tracking using a frame lag of 8 plus correlation interpolation and weighted spatial average give rise to the elastograph with high resolution and accurate shear modulus in alginate. Low percentage of alginates (2%) did not work with rat brains due to mismatch of SW impedance. After trails of experiments and reproducing in mouse brains, 4.7% alginate matches best to its SW impedance and allow smooth SW propagation into the brain. Push parameters 5 works best in 4.7% alginates. In diagnosis of TBI, push parameter 4 appears to be the most sensitive. In control brains, parameter 4 reports an average shear modulus of 6.354kPa and 6.271kPa for left and right hemispheres with $p = 0.819$. In TBI brains, parameter 4 reports an average shear modulus of 4.962kPa and 6.978kPa for TBI and normal hemispheres with $p < 0.01$. The shear modulus on the normal side of the TBI brain, though increases, is not significantly different from that of control hemispheres. This result is consistent with the preliminary study done with SSI in that

brain stiffness all appear to decrease on the TBI side. Nonetheless, this result differs from the preliminary study in that brain stiffness on the normal side of TBI brain does not appear to be higher. This difference may be due to the ex vivo imaging protocol, (for preliminary study, rats are imaged in vivo) which is likely to alter mechanical properties of brain due to exposure. Moreover, the analysis of this project is accurate to 0.5mm regarding to the location of TBI. This gives another hypothesis of the discrepancy in shear modulus in that preliminary studies chose regions without artifacts, which could be anywhere in the hemisphere. The study also gives reasonable shear modulus values for both control and TBI brains, which has not been done yet in the existing literature.

Future Work:

The first step of future work should focus on collecting more data on mice. Due to limited time, only 5 TBI and 5 control mice were studied in the project. More data from animal studies can create a better normal distribution for ANOVA tests, and thus give more accurate average brain shear modulus. Secondly, elastograph should be further optimized for more focused diagnosis of TBI. As due to heavy filtering and averaging of the displacement data, the elastograph tends to spread low G value to non-TBI regions as in fig.36 parameter 2 and 3. Making the elastograph more focusing will certainly increase the contrast between TBI and normal hemispheres. Thirdly, this technology should be applied onto rat brains, as they are larger animal models. Since all the rodent studies will be ex vivo because of their limited skull size, the next step of future work should move on to larger animal models to better represent human brains. The optimized SW tracking algorithm should also be implemented into VUE, so that VUE can display elastograph simultaneously with imaging. Additionally, more sophisticated TBI inducing surgeries or procedures also need to be designed, i.e. procedures that will cause massive and irregular destruction of brain tissue. Finally, the technology needs to be optimized so that it is no longer invasive. The technology can proceed on to human clinical trials if all the above works are finished successfully.

Acknowledgements:

I would like to acknowledge the principle investigator and mentor of the project, Dr.

Pierre Mourad in Department of Neurosurgery. Dr Mourad gave me very valuable suggestions and guidance during my capstone project. As a mentor, Dr Mourad showed me his persistency and passion about his field of research, which motivated me greatly whenever I encountered difficulties. I would also like to acknowledge Ray Illian, Douglas D Kolstoe, John Kucewicz and Chelsea Bossard in my lab for their valuable suggestions and help. Finally, I would like to acknowledge the US Department of Defense for their funding for the project.

Reference:

1. "National Center for Injury Prevention & Control." What is Traumatic Brain Injury?. 07 September 2006. Centers for Disease Control and Prevention. 18 Oct 2006. <http://www.cdc.gov/ncipc/tbi/TBI.htm>.
2. Kennard, Jerry. "Traumatic Brain Injury in Combat Troops--War Zones and Brain Damage" About.com Guide. Web. October 21, 2006. April 17, 2012.

- http://menshealth.about.com/od/conditions/a/TBI_Comat_Troop.htm
3. "All About Traumatic Brain Injury" Your Legal Guide. Web. July 2009. April 17, 2012. <http://www.allabouttbi.com/symptoms.htm>
 4. Mourad, Pierre. "project narrative" 14 Dec. 2009
 5. Xu, ZS, RJ Lee, SS Chu, A Yao, MK Paun, SP Murphy, and PD Mourad. "Evidence of Changes in Brain Tissue Stiffness After Ischemic Stroke Derived from Ultrasound-Based Elastography." *Journal of Ultrasound in Medicine : Official Journal of the American Institute of Ultrasound in Medicine*. 32.3 (2013): 485-94. Print.
 6. MacE, E, G Montaldo, M Fink, M Tanter, I Cohen, and R Miles. "In Vivo Mapping of Brain Elasticity in Small Animals Using Shear Wave Imaging." *Ieee Transactions on Medical Imaging*. 30.3 (2011): 550-558. Print.
 7. "IACUC.org" Web. American Association for Laboratory Animal Science. April 2012. May 29th 2012. <http://www.iacuc.org/aboutus.htm>
 8. Lewin-ICF (1992) *The Cost of Disorders of the Brain*, Washington DC: The National Foundation for Brain Research. [Updated figures based on \$44 billion in 1988 dollars as estimated by: W. Max, E.J. MacKenzie & D. P. Rice (1991), *Head Injuries: Cost and Consequences*. *Journal of Head Trauma Rehabilitation*, 6: 76-91]
 9. Dewall, RJ. "Ultrasound Elastography: Principles, Techniques, and Clinical Applications." *Critical Reviews in Biomedical Engineering*. 41.1 (2013): 1-19. Print.
 10. Bercoff, J, M Tanter, and M Fink. "Supersonic Shear Imaging: a New Technique for Soft Tissue Elasticity Mapping." *Ieee Transactions on Ultrasonics, Ferroelectrics and Frequency Control*. 51.4 (2004): 396-409. Print.
 11. "The Verasonics Ultrasound Engine: A New Paradigm For Ultrasound System Architecture" Copyright 2007, Verasonics, Inc. <http://www.verasonics.com/>
 12. "Understanding Brain Injury Diagnostic Tests CT/MRI/DTI/SPECT/EEG)" *Brain Injury.com*. Web. 04/19/2012. <http://www.braininjury.com/diagnostics.shtml>
 13. Cammoun, D, WR Hendee, and KA Davis. "Clinical Applications of Magnetic Resonance Imaging-Current Status." *The Western Journal of Medicine*. 143.6 (1985): 793-803. Print.
 14. Sahraian, Mohammad A, and Arman Eshaghi. "Role of Mri in Diagnosis and Treatment of Multiple Sclerosis." *Clinical Neurology and Neurosurgery*. 112.7 (2010): 609-615. Print.
 15. "Breakthrough: The most modern MRI techniques are now showing significant pathologies in Subtle Brain Injury cases." Attorney Gordon S. Johnson, Jr. Web. 2001. 4/19/2012. <http://neuro-imaging.net/>
 16. McCracken, P, A Manduca, J P. Felmlee, and R L. Ehman. "Transient Mr Elastography: Modeling Traumatic Brain Injury." *Lecture Notes in Computer Science*. (2004): 1081-1082. Print.
 17. Sack, KJ Streithberger, D Kretting, F Paul, J Braun, and I. "The Influence of Physiological Aging and Atrophy on Brain Viscoelastic Properties in Humans." *Plos One*. 6.9 (2011). Print.
 18. Weaver, JB, AJ Pattison, MD McGarry, IM Perreard, JG Swienckowski, CJ Eskey, SS Lollis, and KD Paulsen. "Brain Mechanical Property Measurement Using Mre with Intrinsic Activation." *Physics in Medicine and Biology*. 57.22 (2012): 7275-87. Print.

- 19.Green, M A, L E. Bilston, and R Sinkus. "In Vivo Brain Viscoelastic Properties Measured by Magnetic Resonance Elastography." *Nmr in Biomedicine*. 21.7 (2008): 755-764. Print.
- 20.Murphy, MC, J. Huston, CR J. Jack, KJ Glaser, A Manduca, JP Felmlee, and RL Ehman. "Decreased Brain Stiffness in Alzheimer's Disease Determined by Magnetic Resonance Elastography." *Journal of Magnetic Resonance Imaging: Jmri*. 34.3 (2011): 494-8. Print.
- 21.Hamhaber, U, I Sack, S Papazoglou, J Rump, D Klatt, and J Braun. "Three-dimensional Analysis of Shear Wave Propagation Observed by in Vivo Magnetic Resonance Elastography of the Brain." *Acta Biomaterialia*. 3.1 (2007): 127-137. Print.
- 22.Johnson, Curtis L, Matthew D. J. McGarry, Armen A. Gharibans, John B. Weaver, Keith D. Paulsen, Huan Wang, William C. Olivero, Bradley P. Sutton, and John G. Georgiadis. "Local Mechanical Properties of White Matter Structures in the Human Brain." *Neuroimage*. 79 (2013): 145-152. Print.
- 23.Deffieux, T, JL Gennisson, B Larrat, M Fink, and M Tanter. "The Variance of Quantitative Estimates in Shear Wave Imaging: Theory and Experiments." *Ieee Transactions on Ultrasonics, Ferroelectrics, and Frequency Control*. 59.11 (2012): 2390-410. Print.
- 24.Zhang, John, Michael A. Green, Ralph Sinkus, and Lynne E. Bilston. "Viscoelastic Properties of Human Cerebellum Using Magnetic Resonance Elastography." *Journal of Biomechanics*. 44.10 (2011): 1909-1913. Print.
- 25.Mak, T.M, Y.P Huang, and Y.P Zheng. "Liver Fibrosis Assessment Using Transient Elastography Guided with Real-Time B-Mode Ultrasound Imaging: a Feasibility Study." *Ultrasound in Medicine & Biology*. 39.6 (2013): 956-966. Print.
- 26.Bamber, J, D Cosgrove, CF Dietrich, J Fromageau, J Bojunga, F Calliada, V Cantisani, JM Correas, M D'Onofrio, EE Drakonaki, M Fink, M Friedrich-Rust, OH Gilja, RF Havre, C Jenssen, AS Klauser, R Ohlinger, A Saftoiu, F Schaefer, I Sporea, and F Piscaglia. "EfsUMB Guidelines and Recommendations on the Clinical Use of Ultrasound Elastography. Part 1: Basic Principles and Technology." *Ultraschall in Der Medizin (stuttgart, Germany)*. 34.2 (2013): 169-84. Print.
- 27.Arndt, R, S Schmidt, C Loddenkemper, M Grünbaum, W Zidek, der G. M. van, and TH Westhoff. "Noninvasive Evaluation of Renal Allograft Fibrosis by Transient Elastography-a Pilot Study." *Transplant International: Official Journal of the European Society for Organ Transplantation*. 23.9 (2010): 871-7. Print.
- 28.Kim, BK, J Fung, MF Yuen, and SU Kim. "Clinical Application of Liver Stiffness Measurement Using Transient Elastography in Chronic Liver Disease from Longitudinal Perspectives." *World Journal of Gastroenterology: Wjg*. 19.12 (2013): 1890-900. Print.
- 29.M. Tanter, J. Bercoff, A. Athanasiou, T. Deffieux, J.L. Gennisson, G. Montaldo et al. "Quantitative assessment of breast lesions viscoelasticity using supersonic shear imaging technique: initial clinical investigation" *Ultrasound Med Biol*, 34 (9) (2008), pp. 1373-1386.
- 30.W.A. Berg, D.O. Cosgrove, C.J. Doré et al. "Shear-wave elastography improves the specificity of breast US: the BE1 Multinational Study of 939 Masses." *Radiology*, 262 (2) (2012), pp. 435-449
- 31.Deffieux, T, JL Gennisson, J Bercoff, and M Tanter. "On the Effects of Reflected Waves in Transient Shear Wave Elastography." *Ieee Transactions on Ultrasonics, Ferroelectrics, and Frequency Control*. 58.10 (2011): 2032-5. Print.
- 32.Alavi, M, F Destrempes, E Montagnon, and G Cloutier. "Dynamic Quantitative Ultrasound Imaging of Mimicked Breast Lesions During Shear Wave Propagation to Emphasize Differences in Tissue Statistical Backscatter Properties." *The Journal of the Acoustical Society of America*. 133.5 (2013). Print.

33. Pneumatic (Cortical) Impact Device. www.muromachi.com/PDF_Pro/.../AMS201_Amscien.pdf
34. Mac, Donald C, A Johnson, D Cooper, T Malone, J Sorrell, J Shimony, M Parsons, A Snyder, M Raichle, R Fang, S Flaherty, M Russell, and DL Brody. "Cerebellar White Matter Abnormalities Following Primary Blast Injury in Us Military Personnel." *Plos One*. 8.2 (2013). Print.
35. Liu, C, NE Murphy, and W Li. "Probing White-Matter Microstructure with Higher-Order Diffusion Tensors and Susceptibility Tensor Mri." *Frontiers in Integrative Neuroscience*. 7 (2013). Print.